CHEMISTRY OF MATERIALS

pubs.acs.org/cm

Article

# Synthesis of Highly Oriented Graphite Films with a Low Wrinkle Density and Near-Millimeter-Scale Lateral Grains

Shahana Chatterjee,* Na Yeon Kim, Nicola Maria Pugno, Mandakini Biswal, Benjamin V. Cunning, Min Goo, Sunghwan Jin, Sun Hwa Lee, Zonghoon Lee, and Rodney S. Ruoff*

Cite This: *Chem. Mater.* 2020, 32, 3134−3143

Read Online

ACCESS | Metrics & More | Article Recommendations | Supporting Information

**ABSTRACT:** Principal defects found in graphite films include grain boundaries and wrinkles. These defects are well known to have detrimental effects on properties such as thermal and electrical conductivities as well as mechanical properties. With a two-fold objective of synthesizing graphite films with large single crystal grains and no wrinkles, we have developed a relatively low-temperature (<1150 °C) process that involves the precipitation of graphite films from nickel−carbon solid solutions followed by in-situ etching of the nickel foil substrates with anhydrous chlorine gas to obtain *near wrinkle-free* continuous graphite films. The size ($L_a$) distribution of lateral grains (or single crystal regions) in these highly oriented graphite films has been found to be asymmetric with the largest grains about 0.9 mm in diameter, as determined by electron backscatter diffraction (EBSD). Thus, the growth of large-area graphite films with grains much larger than those reported for highly oriented pyrolytic graphite (HOPG, ∼20 to 30 $\mu$m), and with a low density of wrinkles, as in the case of HOPG, but prepared at much lower temperatures, is reported here.

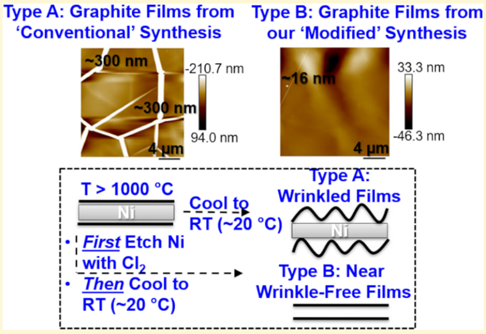

## ■ INTRODUCTION

Methods such as the molten flux route (>1500 °C)[1−5] or the metal−carbon solid solution route[6−17] have been explored to synthesize graphite crystals in the bulk form or as thin films. However, the graphite films generated are often heavily wrinkled, a defect that, along with grain boundaries, dislocations, and vacancies, is largely detrimental to their properties, including thermal and electrical conductivities and mechanical properties. Moreover, although some published studies provide selected area diffraction patterns from transmission electron microscope (TEM) analyses, the analyses are limited to regions $\lesssim 1\ \mu m^2$, and none of these studies report the grain sizes of these graphite materials. Another route to synthesizing graphite involves the thermal cracking of hydrocarbons at very high temperatures (>2000 °C) with applied pressure. This process tends to yield nonwrinkled "highly oriented pyrolytic graphite" (HOPG) as products, but the grain sizes are typically limited to ∼20 to 30 $\mu$m (for grade A HOPG).[18] Another variant of the molten flux method to prepare graphite is the kish-method, where graphite flakes are obtained by the precipitation of C from molten steel. Although these flakes may contain single crystals up to ∼1 mm in size, they contain iron impurities that must be removed by additional purification.[4]

In this work, we have explored the synthesis of graphite films with minimal wrinkles and large grains by precipitation from Ni−C solid solutions in the temperature range of 1000−1150 °C. The Ni−C solid solution may be considered as a model system to study and control the precipitation of graphite films for the following reasons: (1) the Ni{111} surface is lattice matched to the graphene layers, (2) Ni does not undergo additional reactions (such as phase changes or carbide formation) at our temperatures of interest that could otherwise complicate the process, and (3) C dissolution and segregation and precipitation from Ni have been previously studied in detail by in situ techniques such as LEED and Auger electron spectroscopy by several surface science groups.[19−23] Methane was selected as the C precursor of choice as it is a thermally stable hydrocarbon that can only be catalytically decomposed in $H_2$-rich environments at temperatures <1200 °C: this approach minimizes "soot" or amorphous carbon formation from thermally mediated reactions.

Our typical graphite growth process involved (1) exposure of the Ni foils to $CH_4$ gas at $T_{dissolution}$ to form Ni−C solutions followed by (2) precipitation of the graphite films at a lower $T_{precipitation}$ under vacuum and (3) a final cooling step to room temperature (RT) (Process A, Figure 1). Films generated using this process were heavily wrinkled (or buckled), where wrinkles are defined as vertical deviations from a flat surface

Received: January 14, 2020
Revised: March 12, 2020
Published: April 2, 2020

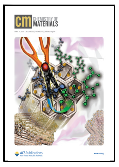

https://dx.doi.org/10.1021/acs.chemmater.0c00154
*Chem. Mater.* 2020, 32, 3134−3143

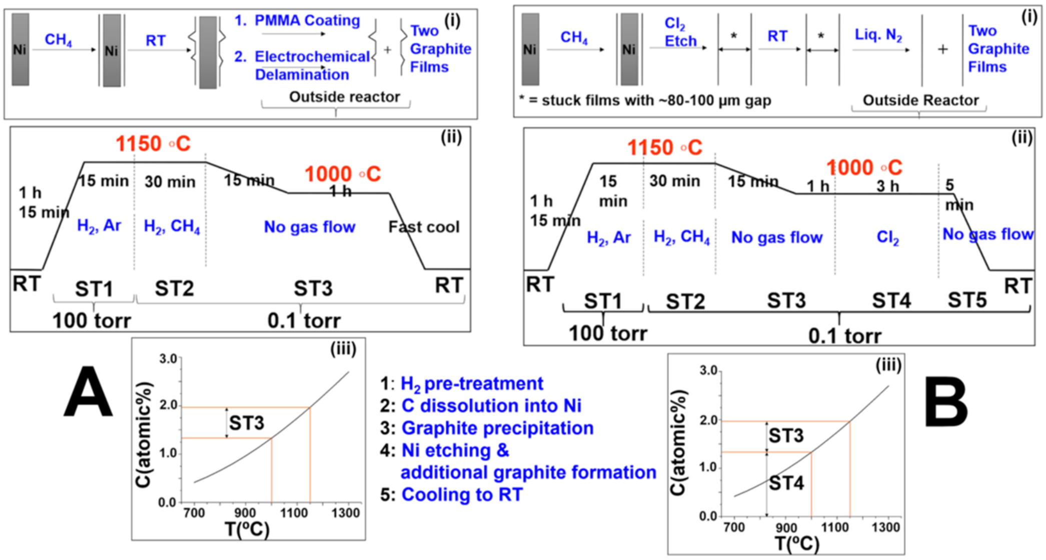

**Figure 1.** Details of the production of **Type A** and **B** films: (i) overall process, (ii) schematic of the process inside the reactor, and, (iii) plots of variation in C solubility with temperature in polycrystalline Ni showing the amounts of C precipitated as graphite during steps **3** (due to a reduction in temperature), and, **4** (due to Ni etching) of the process (ST = step).

(Figure S2). Such films are referred to as Type A films in this manuscript (Figure 2 and Figures S3 and S4). The major cause of the formation of wrinkles in thin films synthesized at high temperatures (>800 °C) is the thermal stress generated due to the mismatch in the coefficients of thermal expansion (CTEs) between the thin film and the growth substrate (other factors such as intrinsic stresses generated during growth and extrinsic stresses due to external factors may also cause wrinkling). For example, when cooled from a growth temperature of 1000 °C to RT, the lattice parameter "a" of face-centered cubic (FCC) Ni changes from 3.58 to 3.52 Å (i.e., ∼1.7% contraction),[24] while for graphite, the change in the in-plane lattice constant is negligible (Figure S5).[25,26] This unequal contraction introduces biaxial compressive stresses in the film that are released by forming a network of delamination buckles in the film.

Wrinkling may distort the local crystal symmetry and thus introduce bond strain and crystallographic defects in the graphite film. At a more severe level, wrinkling may even lead to bond breakage in graphite films. Wrinkling has been observed to degrade several material properties in graphene[27−29] or to enhance its chemical reactivity.[30,31] Strategies to prevent wrinkling in single-layer graphene include growth on copper substrates with a specific crystallographic orientation (Cu(111)),[32,33] switching to lower CTE substrates like metallic platinum[34] or nonmetallic germanium,[35] or growth at lower temperatures (Cu/Ni(111) at 750 °C).[36] However, to the best of our knowledge, no attempts on eliminating wrinkling in graphite or multilayer graphene films have been reported in the literature.

## ■ RESULTS AND DISCUSSION

Our approach for preventing wrinkle formation in graphite films has been to remove *physical contact* between the Ni foil and the graphite films immediately after growth at 1000 °C and then cool the resulting free-standing graphite films to RT. This essentially involved chemical etching of the Ni foil(s) at $T_{\text{precipitation}}$ or 1000 °C. An ideal reagent for this purpose should have the following characteristics: it should (1) be stable at 1000 °C, (2) have sufficient vapor pressure for easy introduction into a reactor under dynamic gas flow conditions, (3) selectively react with the Ni foil(s), (4) form reaction products with sufficient vapor pressures that can be removed without contaminating the graphite films, (5) not introduce defects into the graphite films, and finally, (6) not interfere with the graphitization process of the dissolved C in the Ni foil(s).

Commercial etchants and aqueous solutions of nonoxidizing and oxidizing acids, such as HCl, $HNO_3$, $H_2SO_4$, or $H_3PO_4$, that are commonly used for etching Ni at temperatures <200 °C cannot be used for high-temperature etching inside a reactor. Oxidizing reagents such as supercritical water or oxygen gas will also completely or partially oxidize the graphite film (and possibly also generate $CH_4$, CO, or $CO_2$) while converting the Ni foil to nickel oxide powder. Similarly, sulfur-containing etchants such as $H_2S$ acid vapor are known to produce stable S-doped graphene at temperatures above ∼600 °C.[37] Again, anhydrous HCl or other nonoxidizing acid vapors cannot be used because HCl will produce $H_2$ gas, both by thermal dissociation (∼0.73% at 1000 °C)[38] and upon reaction with Ni, which may etch the graphene layers. Moreover, as the remaining dissolved C in the Ni foil graphitizes as the foil is etched (discussed in detail later), the presence of $H_2$ may complicate this process by creating vacancies or sp$^3$ carbon. Indeed, $H_2$−$Cl_2$ mixtures have been used to form nanodiamond particles or sp$^3$ carbons that are not wanted in our process.[39,40]

It has been shown that the carbon−halogen bonds in halographenes[41] and graphite fluoride[42] are unstable at temperatures above 400−700 °C. For example, the C−Cl bond is not stable at high temperatures and pristine graphene can be recovered from chlorinated graphene by heating to temperatures >500 °C.[43,44] Indeed, one method of purifying natural and kish graphites industrially is by exposing them to anhydrous $Cl_2$ gas at high temperatures.[4] Moreover, the synthesis of carbide-derived carbons (CDCs) has been explored with the reaction of carbides $MC_x$ (M = Si, Al, Ti, Zr, V, Nb, Ta, etc.) with $Cl_2$−Ar under dynamic flow and ambient pressure at ∼900 to 1000 °C to form graphitic C and

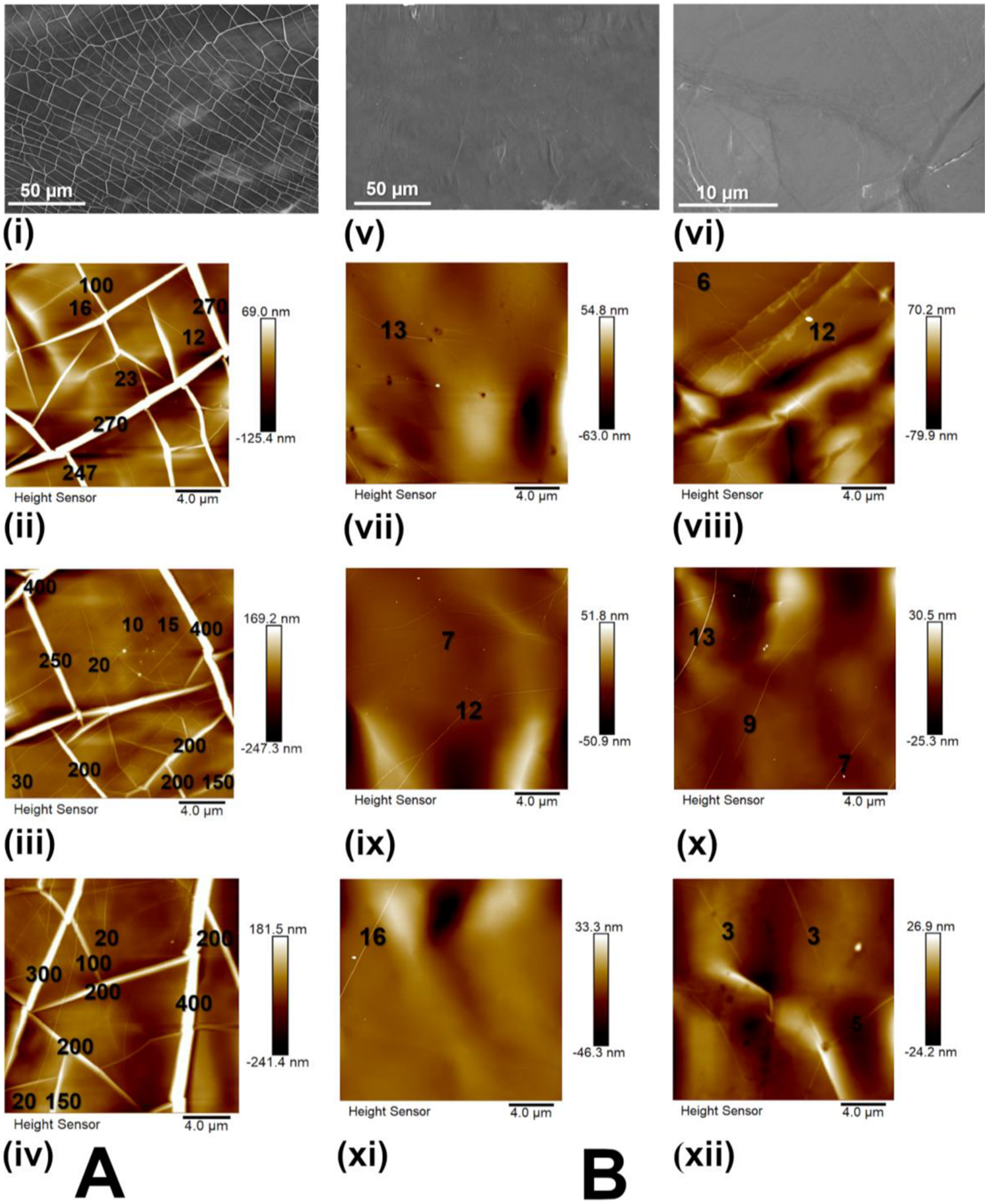

**Figure 2.** SEM and AFM images of graphite films. **Type A** films: (i) SEM image, and, (ii)-(iv) AFM images; **Type B** films: (v)−(vi) SEM images, and, (vii)−(xii) AFM images. All AFM images show 20 × 20 $\mu m^2$ scan areas. Numbers across the wrinkles denote their heights in nanometers.

$MCl_x$.[45,46] The other halogens react similarly with $MC_x$ and are all potentially suitable agents for etching Ni at high temperatures without damaging the graphite film.[46,47] Because anhydrous $Cl_2$ gas has a higher reactivity than $Br_2$ and $I_2$, and because they are respectively a liquid and a solid that would require additional optimization of appropriate bubbler-type set-ups, we selected $Cl_2$ for the etching process. Fluorine was not selected because of its severe safety hazards.

In order to remove wrinkles, after the graphite films had formed at 1000 °C ($T_{precipitation}$), anhydrous $Cl_2$ gas was introduced for ∼3 h to etch away the Ni foil sandwiched between the two graphite films that had grown on its two sides (Process B, Figure 1). The temperature for graphite growth and subsequent Ni etching was selected to be 1000 °C to ensure that the $NiCl_2$ produced did not contaminate the graphite films because $NiCl_2$ has a high enough vapor pressure to be removed from the reaction zone under dynamic vacuum.

It is important to note that for the graphite growth runs in which the Ni was etched (process B), the Ni foils were placed in boats with covers to prevent the resulting free-standing graphite films from flying away under this dynamic vacuum (Figure S6). As the Ni etching progressed, an orange anhydrous $NiCl_2$ powder was deposited on the cooler surfaces of the reactor (Figure S7). When the graphite growth and Ni etching were completed, the $Cl_2$ gas was turned off, and the films were cooled to RT after a 5 min wait period at 1000 °C. This wait time was necessary to pump out all the $Cl_2$ gas before cooling in order to eliminate any possible chance of C−Cl bond formation at lower temperatures (<500 °C). At this point, these graphite films no longer had a Ni substrate in physical contact and hence did not experience the ∼1.7% biaxial compressive stress they otherwise would have had. At RT, the films were recovered from the furnace and floated in ethanol or acetone. However, the two graphite films that had grown on the two sides of the Ni foil had collapsed onto each other (with gaps of ∼80 to 100 $\mu$m) after the Ni etching process. The films were then separated by gentle mechanical agitation with liquid $N_2$ (see the Supporting Information for details) and tested for the presence of any metallic Ni(0) residue by bringing a magnet close to them. If the films were not attracted to the magnet, they were tentatively considered free of Ni(0) (Figure S8). The residual Ni concentration was later measured on select films by inductively coupled plasma-optical emission spectroscopy (ICP-OES). The results given in Table S2 show that the Ni content was quite small, ∼0 to 1%. The films were then transferred onto silicon wafers and air dried for further characterization. These films are referred to as Type B films in this manuscript.

The surfaces of the Type B graphite films were examined by optical microscopy (Figure S9) and SEM (Figure 2 and Figure S10) and showed a huge reduction in the total number of wrinkles. The films had lost their corrugated appearance, and the larger wrinkles were completely absent. The few remaining wrinkles were possibly caused by mechanical stresses during handling of these free-standing submicrometer-thick films. AFM imaging of the graphite surfaces showed that such wrinkles were ∼5 to 20 nm high and ∼0.1 to 0.2 $\mu$m wide. AFM imaging also showed that the films were "wavy", as might be expected from such free-standing films. Unsurprisingly, the film had occasional tears or holes, which were most likely a result of mechanical damage during the separation of the two films (Figure 2 and Figure S11).

The etching rate of Ni with $Cl_2$ was observed to be important for two main reasons. First, etching conditions that were "too harsh" mechanically damaged the films, forming, for example, torn and crumpled films when the $Cl_2$ flow rate or the reactor pressure were too high (Figure S12). Second, at 1000 °C, the Ni foil not only has graphite films on both surfaces but also about 1.3 at. % C in the bulk (Figure 1). This dissolved C graphitizes during the Ni etching step (neither the dissolved C nor the precipitated graphite are etched by $Cl_2$ at this temperature, as explained earlier). This suggests that the Ni etching rate may be an important parameter to consider to better control the C precipitation during Ni removal and the final structure of the graphite films. Hence, in order to form large graphite grains, the etching must be carried out at an optimized rate so that these C atoms are added to existing grains instead of randomly nucleating smaller new ones. Although we were able to optimize the etching rates so that minimally damaged films with large grains were produced, we were not able to independently evaluate the effects of rapid etching on the grain size, because this forms crumpled graphite films that could not be characterized by the diffraction techniques to be discussed later.

Graphite growth in process B thus occurs in two stages: (1) by nonisothermal precipitation as a result of a reduction in temperature from $T_{\mathrm{dissolution}}$ to $T_{\mathrm{precipitation}}$ (step 3, Figure 1), and (2) by isothermal precipitation at $T_{\mathrm{precipitation}}$ as the amount of Ni is reduced by chemical etching (thus continuously saturating the Ni with C; step 4, Figure 1). No obvious difference in quality was observed between the graphite precipitated in steps 3 and 4 (see Supporting Information for details). As a consequence of this Ni etching step, Type B films were found to be much thicker than the films grown without Ni etching, as performed for Type A films. Thus, Type B films have an average thickness in the range of ∼750 to 800 nm, while Type A films have an average thickness of ∼250 nm (Figure S13), values that approximately match the predicted thickness from C solubilities (Predicted: Type B, 805 nm; Type A, 265 nm; Table S1).

The initial characterization of the chemical nature of the as-synthesized films included electron energy loss spectroscopy (EELS), X-ray photoelectron spectroscopy (XPS) analysis, and Raman spectroscopy. EELS and XPS analyses showed that the film contained only $sp^2$ carbon and that no additional functionalization was present (Figures S14 and S32). Raman mapping was performed on several samples to obtain information on the film quality from the $I_D/I_G$ ratio, and it ranged from ∼0.04 to 0.09 (Figure S15, Table S3-i), indicating that they were high quality with mostly $sp^2$-bonded C atoms.

In order to determine the stacking order of the graphene layers, Raman mapping of the 2D peak was performed, and the stacking order was evaluated based on the method of Cancado et al. (see the Supporting Information for details).[48] For a Grade A HOPG sample with almost complete AB stacking, the metric obtained by this method was ∼1.0, whereas for both Type A and Type B films, it varied from ∼0.84 to 1.0 (Table S3-ii). However, our films did show regions, where the AB stacking order is obviously broken (Figure S17), but at this time, we are not certain what causes such disorder and hypothesize that such regions may be due to defects such as stacking faults or grain boundaries. These Raman results are consistent with the XRD data (discussed later) from which an "average" $d_{0002}$ spacing of 3.35 Å was obtained for all samples, which also implies that the layers are mostly AB stacked.

The crystal dimensions in both the "$a$" ($L_a$ or lateral dimensions) and "$c$" directions ($L_c$) must be determined to define the size of a single crystal or grain in our films, and electron backscatter diffraction (EBSD) has been used to determine the orientation and lateral grain size of the films. EBSD is a common technique for the determination of orientation and grain size in metallic and ceramic samples that utilizes Kikuchi patterns produced by backscattering of diffusely scattered electrons inside the sample for phase identification and determination of the crystal orientation. EBSD analysis has been used for characterizing graphitic regions in iron[49,50] and has been reported for graphite samples in two conference proceedings.[51,52] To the best of our knowledge, there has been no earlier work on the use of EBSD to obtain a detailed and rigorous evaluation of the grain orientation and size in graphite.

In order to verify that EBSD can be used to determine the graphite grain orientation and size, EBSD was first performed on flakes of natural graphite transferred to silicon wafers. In EBSD, the software utilizes a user-defined sample co-ordinate system and phase to match the Kikuchi bands of the sample with reference patterns and determines crystal orientation.[53] Thus, one relatively stringent requirement is that the sample surface must be completely flat and perpendicular to the normal direction (ND) of the sample co-ordinate system at all points. Hence, all samples were pressed with a roller a few times before measurement, which may have introduced additional wrinkles. Because graphite is a soft and layered material, no other chemo-mechanical polishing that is common for the preparation for metallic and ceramic samples for such studies was performed as it could have severely damaged the surface.

Orientation mapping involves the determination of the crystal orientation (or index) of all pixels in a scan and then delineating grain boundaries based on the mis-orientation between these pixels. Hence, the first step after collecting the scan from a natural graphite flake was to evaluate the quality of the Kikuchi patterns obtained using an image quality (IQ) map (Figure S18-i) followed by the evaluation of the confidence index (CI) map that shows the CI values associated with each pixel. The CI values represent the acceptability of the indexing results and range from 0 to 1 (Figure S18-ii). Only orientations with CI values >0.1 were considered for subsequent analysis after processing (Figure S18-iii). Finally, the indexing success rate (ISR) was determined, where ISR is simply the ratio of the points with CI values >0.1 to the total number of scanned points. As shown in Figure S18, there is good correlation between the IQ and CI maps, and the ISR is ∼99.6%, indicating that this is a good scan. The details of this process have been provided in the Supporting Information.

The EBSD data may be represented by pole figures (PFs), inverse pole figures (IPFs), IPF maps, and kernel average mis-orientation (KAM) maps. The PFs show plots of specified crystal directions or poles of the different unit cells of the grains in the sample with respect to the sample coordinate system. On the other hand, IPFs show plots of a sample direction (such as the ND) with respect to specific crystal directions of the differently oriented unit cells in the sample. Thus, two key pieces of information are obtained simultaneously: the number or set of points reflects the number of grains in the sample, whereas their locations indicate the location of specific crystal directions of the different grains (i.e., single crystal regions) with respect to the sample co-ordinate system. In both the PFs and IPFs, the points have been weighted by the associated grain sizes for easy identification of a particularly large grain and multiple smaller grains, as is often the case. Figure S19-I-i shows the plots of the PFs for the $\langle 0001 \rangle$ and $\langle 10\bar{1}1 \rangle$ crystal directions of the different grains in the scan for natural graphite. It contains two large points (for the (0001) PF) or sets of points (for the $(10\bar{1}1)$ PF) and several tiny (or sets of tiny) points, which implies that the scanned region contains two large grains. The IPF for the natural graphite scan (Figure S19-I-ii) shows the plots of the sample ND with respect to the crystal directions of the different grains. It contains points close to the $\langle 0001 \rangle$ direction, implying that the $\langle 0001 \rangle$ directions of the different grains are essentially parallel to the sample ND. In other words, the $\{0001\}$ planes of all grains in the film are parallel to the sample surface. The IPF also shows two coincident large points, implying that two large grains are present. Finally, the IPF map is color coded to represent the orientation of the ND of each pixel in the scan, which for this scan is parallel to the $\langle 0001 \rangle$ directions of all associated grains (Figure S19-III). The last step of the EBSD scan analysis involves delineating the grain boundaries and calculating the grain size (see Supporting Information). The grain diameters for regions 1 and 2 have been calculated from their areas to be ∼500 and ∼450 μm, respectively. Figure S19-IV shows the KAM map from the natural graphite scan comparing the mis-orientation between neighboring pixels: the mis-orientation between the first nearest neighbors is generally <2°.

Several Type B films have been analyzed by EBSD. However, perhaps because of an uneven surface topography, the ISR values were somewhat lower. Smaller scan areas ($\leq$125 × 200 μm) tended to have larger ISR values (∼99%), but the grain sizes were artificially limited by the areas scanned (Figure 3 and Figures S20 and S21 and Table S4). To determine the "true" grain sizes, EBSD scans over an area of about 1.5 × 1.5 mm$^2$ were performed. Figure 4 shows the IPF and PF plots for two Type B films with the $\{0001\}$ orientation and the largest grains about 0.9 mm in diameter. The (0001) PFs for both films show a single large point, and the $(10\bar{1}1)$ PFs show one set of large points, confirming that these regions are single crystals. The yellow regions in the IPF map and the circled points in the PFs and the IPFs are from the exposed silicon wafer where the films have holes or tears (Figure S27). A large area scan from a Type A-wrinkled film is shown in Figure S23 and shows that the largest grain diameter is about 0.8 mm. The KAM maps and details of all large area scans are provided in Figure S22 and Table S5.

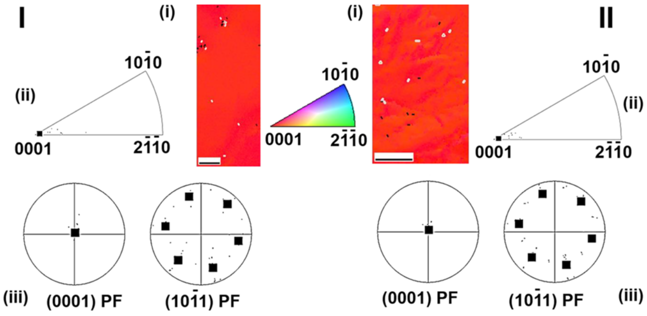

**Figure 3.** EBSD scans of **Type B** graphite films. (I) A high resolution scan with a step size of 250 nm, and, (II) A scan where the grain size is limited by the scan size: (i) IPF map of the sample ND (Scale bars: 5 μm (**I**), 50 μm (**II**)); (ii) IPF of the sample ND; (iii) left: (0001) PF, and, right: $(10\bar{1}1)$ PF. Grain boundaries are represented in white and black areas represent pixels with CI < 0.1 that have not been included in the IPF maps. The points in the PFs and IPFs have been weighted by grain size. ND refers to the normal or (001) direction of the sample co-ordinate system.

A probable reason for the lower ISRs can be obtained by comparing the maps in Figure S24, where the SEM image (i), the "raw" IQ map (ii) and the IQ (iii) and the CI (iv) maps from postprocessing are shown. From these figures, it is obvious that nonflat regions have lower IQ values that result in low CI values and poor indexing. In this example, the nonflat regions are the ones where the film has torn materials deposited on top of it, which perhaps obscure the Kikuchi patterns from the film lying beneath it. However, even without material deposition on the top and a sharp Kikuchi pattern, the local surface curvature (i.e., any deviation from the user defined sample co-ordinate system) may result in a failure by the software to index the pixel with an acceptable CI value and lead to an overall lower ISR for the scan.

Figure 5 shows a comparison between similar area scans from a Type B film, a natural graphite flake, and commercial grade A HOPG. It is concluded from the unique grain color maps that grain sizes in grade A HOPG are much smaller (6–26 μm) than in the natural or Type B graphite samples. Again,

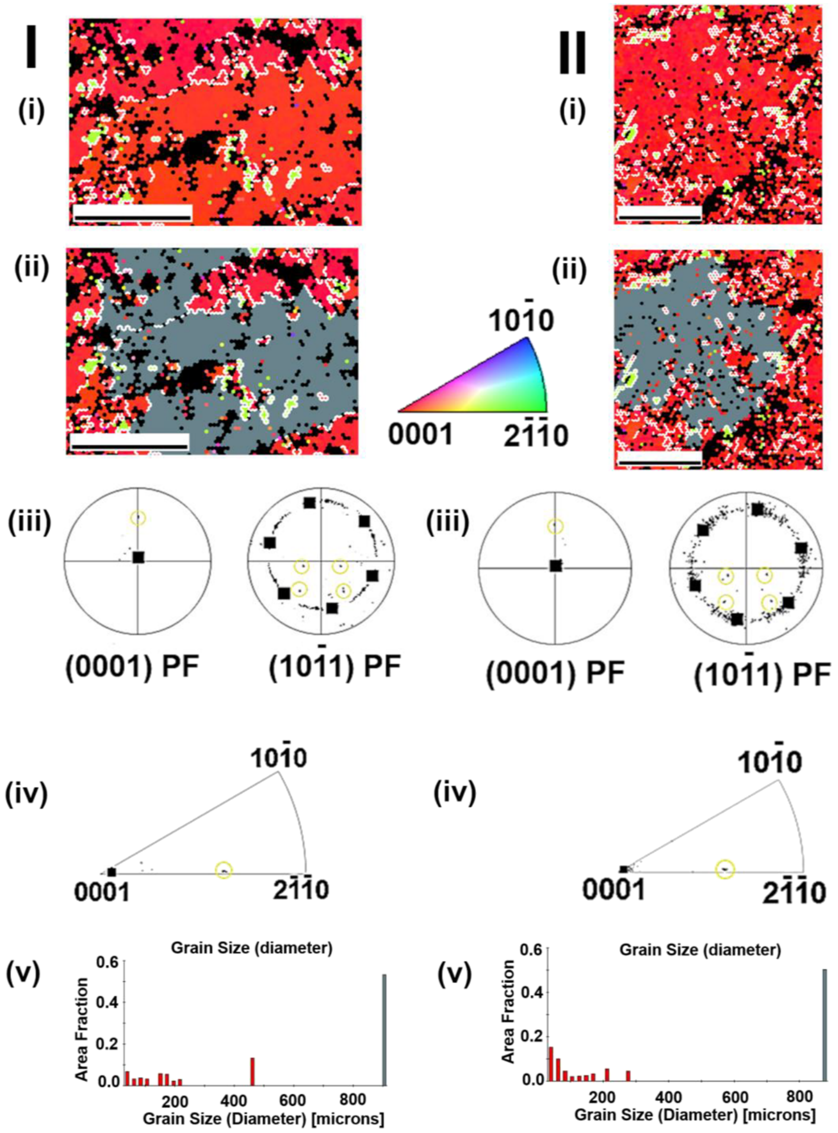

**Figure 4.** Large area EBSD scans of two **Type B** graphite films (I) and (II): (i) IPF map for the sample ND; (ii) IPF map for the sample ND with the largest grain highlighted in gray (Scale bars: (I) 600 $\mu$m; (II) 500 $\mu$m); (iii) left: (0001) PF, and, right: $(10\overline{1}1)$ PF; (iv) IPF of the sample ND; (v) grain size chart with the largest grain highlighted in gray. Grain boundaries are represented in white and black areas represent pixels with CI < 0.1 that have not been included in the IPF maps. Yellow regions in the IPF maps or the points circled in yellow on the IPFs and PFs are from the bare silicon wafer. The points in the PFs and IPFs have been weighted by grain size. ND refers to the normal or (001) direction of the sample co-ordinate system.

the quasi ring-like appearance of the $(10\overline{1}1)$ PF of grade A HOPG versus the single set of large points for natural graphite or the Type B graphite film clearly demonstrates that the grains in HOPG are much smaller.

XRD experiments that involved coupled $\omega$-2$\theta$ scans with a 0-D detector were performed to probe the crystal structure in the "c" direction and showed that the films have a preferred orientation because only the {0002} family of peaks was detected. The $d_{0002}$ values calculated from these scans were all clustered around 3.354 Å (Table S7-i), which implies that the films are, on average, AB stacked (a higher $d_{0002}$ value would imply turbostratic stacking).[54] This result does not contradict the Raman spectroscopic analysis discussed earlier showing occasional deviations from AB stacking. This is because Raman spectroscopy has a much higher resolution (spot size of beam ~700 to 800 nm at 100× magnification; information depth ~30 nm), whereas XRD provides an average value for the entire film (spot size of beam ~1 mm; information depth ~entire film).

Mosaic spread is a parameter that is commonly used for HOPG samples to determine crystallite (or single crystal) alignment in the "c" direction and a lower value of this metric signifies greater crystallite alignment (see the Supporting Information for details). The mosaic spread values obtained were in the range of ~0.1 to 0.2° for Type B films and ~0.5° for Type A films. This indicates that the crystallite alignment in Type B films is at least as good as in Grade A HOPG, keeping in mind that these films are not perfectly flat which may artificially increase the mosaic spread value.

High-resolution TEM (HR-TEM) was also used to study and compare Type A and Type B graphite films (Figure 6). Electron transparent Type A films imaged in the top-down mode (plan view TEM) showed a heavily wrinkled appearance with 3−4 wrinkles often emerging from common junction

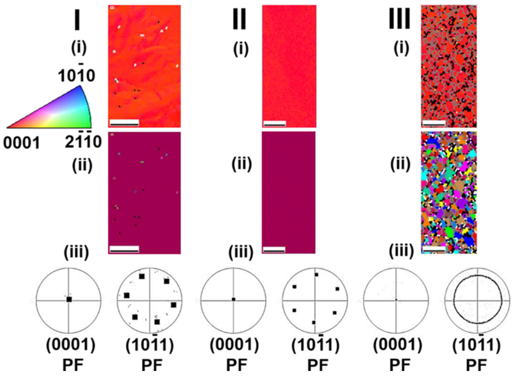

**Figure 5.** Comparison of similar sized EBSD scans (~125 × 220 $\mu m^2$): (I) Type B graphite film, (II) Natural graphite flake, (III) Grade A HOPG (Optigraph); (i) the IPF map for the normal direction of the sample co-ordinate system; (ii) the unique grain color map; (iii) left: (0001) PF, and, right: (10$\bar{1}$1) PF for the respective scans. Scale bars for (i) and (ii): 50 $\mu$m. Grain boundaries are represented in white (IPF map) or gray (unique grain color map) and black areas represent pixels with CI < 0.1 that have not been included. The points in the PFs have been weighted by grain size.

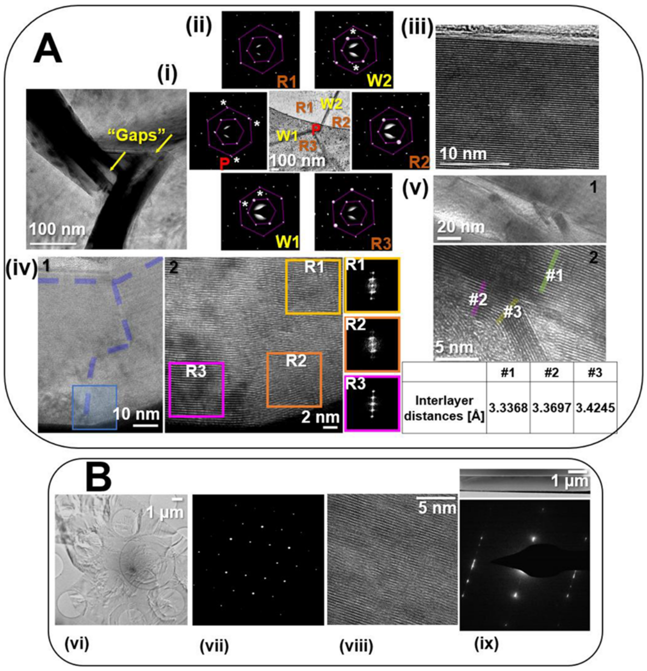

**Figure 6.** HR-TEM images and selected area diffraction (SAED) patterns of graphite films. **Type A** films: (i) a wrinkle junction; (ii) SAED patterns from a region containing a wrinkle junction (P: junction point) where spots adjacent to the stars are examples of select "additional" spots in the patterns from wrinkles W1, W2 and P; R: region; (iii) defect-free crystal lattice; (iv) (1) lower and (2) higher magnification images of a region containing a conformal bend, and, digital diffractograms (right) from selected regions showing variation in crystallinity; (v) (1) lower and (2) higher magnification images of a region containing a nano-buckle with the spacing of the $d_{0002}$ lattice fringes in regions 1−3 tabulated below. **Type B** films: (vi) image, and, (vii) SAED pattern from a film thinned to electron transparency; (viii) cross-section image, and (ix) SAED pattern of a typical ~800 nm film.

points. High-magnification images of these junction regions revealed "gaps" where the graphene layers had physically separated, possibly due to shear stress. Selected area electron diffraction (SAED) of such junctions was then done to explore whether wrinkling had locally modified the orientation. SAED showed no change in orientation although additional diffraction spots were present, possibly from the folded over part in the wrinkle. On the other hand, cross-sectional TEM imaging performed on thicker and thinner Type A films revealed two types of large angular bends (>100°) in the {0002} lattice fringes of the graphene layers. These include ~130 to 160° conformal bends adjacent to the Ni substrate and ~130 to 150° nanobuckles within the graphene layers of the film. Nanobuckles may show variations in the $d_{0002}$ lattice fringe spacing and may have adjacent physical gaps. Both nanobuckles and conformal bends may have neighboring regions of lower crystallinity. The details of the TEM characterization of Type A-wrinkled films and the possible implication of buckling of the graphene layers on the growth process and film properties will be reported elsewhere.

For Type B films, the plan-view HR-TEM image on a film thinned to electron transparency by mechanical exfoliation showed the region to be a single crystal with AB stacking. Figure 6-viii,ix show the cross-section of a Type B film and respectively a high-resolution image and a diffraction pattern, proving that it is a highly crystalline material. Again, the sharpness of the diffraction spots indicates that this is a single-crystal region.

In order to further understand the role of the Ni substrate on graphite grain size, attempts were made to correlate the grain structure of the Ni substrate with that of the graphite film. It was found that considerable grain growth had occurred in the Ni foil after the $H_2$ pretreatment step (step 1, Figure 1) and that the foil contained grains of different orientations that could be as large as ~850 $\mu$m (Figure S29). The fact that the largest graphite grains were also ~800 to 900 $\mu$m in size suggests that a relationship may exist between the grain sizes of the graphite film and the Ni substrate. Again, the graphite grains were always found to have the {0001} orientation. Thus, the graphene layers of the films grow parallel to the Ni substrate irrespective of the orientation of the Ni grains. This has been previously observed by Johansson et al. while exploring the orientations of their graphite films and the underlying polycrystalline Ni substrate by electron diffraction in the TEM.[55] Additional details on the role of the substrate on graphite film growth will be reported elsewhere.

One of the major improvements expected from the removal of wrinkles in graphite films is a significant increase in their Young's modulus/ stiffness. Hence, removing wrinkles from an area fraction = 0.1, from films that have wrinkle amplitude/film thickness ratios ranging from 1 to 10, would increase their respective Young's modulus by a factor of 0.6−60.[56] However, the removal of wrinkles is not expected to significantly influence the film strength and the potential applications for wrinkle-free graphite films are where "high-modulus carbon films" are required (similar to high-modulus carbon fibers that are obtained by the removal of the misalignment between the constituent crystalline carbon ribbons).

On the other hand, removal of grain boundaries is expected to increase the film strength and stiffness.[57,58] An increase in grain size has been observed in silico as capable of increasing the fracture strength of polycrystalline graphene, following an inverse Hall−Petch-like relation and demonstrating that the grain boundary junctions are the weakest links. From this result, a ~2 times increase in strength may be expected with an increase in grain size $d$ in a graphite film of a size $L$, when the

$L/d$ ratio changes from 10,000 to 10. Accordingly, the potential applications for both wrinkle and grain boundary-free graphite films are where "high-modulus and high-strength carbon films" are required. A detailed discussion can be found in the Supporting Information.

## ■ CONCLUSIONS

We have shown that we can grow graphite films with few wrinkles by growing them on Ni foils at high temperatures and then removing the Ni substrates by chemical etching to eliminate issues caused by the CTE differences between the films and the foils. Moreover, by optimizing the process parameters, we have grown continuous graphite films with near-millimeter-scale lateral grains. We believe that this is the first report of an attempt to reduce wrinkling in thin films of a layered material, with single-layer graphene being a notable exception. This is also the first rigorous attempt to unambiguously determine grain sizes in graphite by EBSD, which has been used extensively for this purpose. Initial calculations on mechanical properties predict a significant improvement in axial stiffness and strength in these films attributed to a reduction in the number of wrinkles and an increase in grain size.

However, intrinsic stresses from the growth process and external stresses generated after the growth process that may cause other defects including fine wrinkles have not been eliminated or studied. The current technical limitations of the overall process include the formation of holes or tears in the films and the inability to obtain pristine thin films of graphite or multilayer graphene, both due to the difficulty of handling such free-standing films in the reactor without mechanical damage. Such limitations may be removed with appropriate equipment and experimental design modifications, such as by using more suitable sample holders. In the future, we hope to see such films generated so that the expected property improvements discussed above can be studied and evaluated.

## ■ EXPERIMENTAL SECTION

In a typical process, the reactor was loaded with ∼1 cm$^2$ pieces of Ni foil (thickness: 100 $\mu$m; purity: 99.994%, metals basis) in quartz boats covered with alumina lids. The furnace temperature was slowly increased to 1150 °C in 1 h 15 min (∼15 °C/min) under an Ar/$H_2$ flow at 100 Torr followed by a 15 min hold at 1150 °C (step 1). This was followed by a $CH_4$ exposure step at a pressure of <0.1 Torr (step 2). Then, all gases were turned off and the temperature was quickly reduced to 1000 °C (at 10 °C/min) and held at 1000 °C for 1 h under dynamic vacuum to precipitate the graphite films (step 3). This quick temperature reduction was to minimize graphite precipitation during this ramp down process and ensure that most of the film is generated at 1000 °C. In one set of experiments (Process A, Figure 1), the samples were then fast cooled to RT by switching off and sliding the furnace ∼20 cm away from the samples and turning on a table fan. Finally, the Ni foils with graphite films on both sides were recovered. Selected films were delaminated using the electrochemical delamination method[59] with ∼1 M NaOH after (spin)coating them with polymeric PMMA (polymethyl methacrylate) support layers. These graphite-PMMA films were transferred to silicon wafers or other substrates of choice followed by PMMA removal using acetone and $H_2$/Ar treatments at 400 °C.

In a second set of experiments (Process B, Figure 1), after the formation of the graphite films at 1000 °C, ∼10 to 20 sccm of anhydrous $Cl_2$ gas was introduced into the reactor for ∼3 h (step 4). At the end of this process, the $Cl_2$ gas was turned off, and after a 5 min wait time, the furnace was turned off and cooled to RT (step 5). At the end of this process, *only* unsupported graphite films were recovered. The graphite films were then collected and floated in ethanol or acetone. At this point, each recovered film was composed of two graphite films ("collapsed" films) that had originally grown on the two sides of each Ni foil and collapsed onto each other during the Ni etching. Liquid $N_2$ was added slowly to the ethanol where the films were floating, and these two graphite films were separated by gentle mechanical agitation. The films were then transferred to substrates of choice for further characterization.

Additional experimental details including characterization methods can be found in the Supporting Information.

## ■ ASSOCIATED CONTENT

### Supporting Information

The Supporting Information is available free of charge at https://pubs.acs.org/doi/10.1021/acs.chemmater.0c00154.

> Details of synthetic and characterization methods and mechanical property calculations; and profilometry data, XPS spectra, EELS spectra, Raman spectra, XRD data, and additional optical microscopy, SEM and AFM images, and EBSD scans (PDF)

## ■ AUTHOR INFORMATION

### Corresponding Authors

**Shahana Chatterjee** − *Center for Multidimensional Carbon Materials (CMCM), Institute for Basic Science (IBS), Ulsan 44919, Republic of Korea;* orcid.org/0000-0001-7406-1154; Email: chatterjee.shahana@gmail.com

**Rodney S. Ruoff** − *Center for Multidimensional Carbon Materials (CMCM), Institute for Basic Science (IBS), Ulsan 44919, Republic of Korea; Department of Chemistry, School of Materials Science and Engineering, and School of Energy and Chemical Engineering, Ulsan National Institute of Science and Technology (UNIST), Ulsan 44919, Republic of Korea;* orcid.org/0000-0002-6599-6764; Email: ruofflab@gmail.com, rsruoff@ibs.re.kr

### Authors

**Na Yeon Kim** − *Center for Multidimensional Carbon Materials (CMCM), Institute for Basic Science (IBS), Ulsan 44919, Republic of Korea*

**Nicola Maria Pugno** − *Laboratory of Bio-Inspired, Bionic, Nano, Meta Materials & Mechanics, Università di Trento, I-38123 Trento, Italy; School of Engineering and Materials Science, Queen Mary University of London, London E1 4NS, U.K.; Fondazione E. Amaldi, Ket Lab, 00133 Rome, Italy;* orcid.org/0000-0003-2136-2396

**Mandakini Biswal** − *Center for Multidimensional Carbon Materials (CMCM), Institute for Basic Science (IBS), Ulsan 44919, Republic of Korea;* orcid.org/0000-0002-1295-1095

**Benjamin V. Cunning** − *Center for Multidimensional Carbon Materials (CMCM), Institute for Basic Science (IBS), Ulsan 44919, Republic of Korea*

**Min Goo** − *Center for Multidimensional Carbon Materials (CMCM), Institute for Basic Science (IBS), Ulsan 44919, Republic of Korea; Department of Chemistry, Ulsan National Institute of Science and Technology (UNIST), Ulsan 44919, Republic of Korea*

**Sunghwan Jin** − *Center for Multidimensional Carbon Materials (CMCM), Institute for Basic Science (IBS), Ulsan 44919, Republic of Korea*

**Sun Hwa Lee** − *Center for Multidimensional Carbon Materials (CMCM), Institute for Basic Science (IBS), Ulsan 44919, Republic of Korea*

**Zonghoon Lee** − *Center for Multidimensional Carbon Materials (CMCM), Institute for Basic Science (IBS), Ulsan 44919, Republic of Korea; School of Materials Science and Engineering, Ulsan National Institute of Science and Technology (UNIST), Ulsan 44919, Republic of Korea;* orcid.org/0000-0003-3246-4072

Complete contact information is available at: https://pubs.acs.org/10.1021/acs.chemmater.0c00154

## Notes

The authors declare no competing financial interest.

## ■ ACKNOWLEDGMENTS

This work was supported by IBS-R019-D1. N.M.P. ackowledges the support of the European Commission under the Graphene Flagship Core 2 grant No. 785219 (WP14, “Composites”), the FET Proactive (“Neurofibres”) grant No. 732344, the FET Open (Boheme) grant No. 863179 as well as by the Italian Ministry of Education, University and Research (MIUR) under the “Departments of Excellence” grant L. 232/2016, the ARS01- 01384-PROSCAN and the PRIN-20177TTP3S grants. The authors would like to thank Prof. Marc DeGraef (Carnegie Mellon University) and Prof. Luigi Colombo (University of Texas at Dallas) for helpful discussions and comments regarding this manuscript. S.C. would like to acknowledge Dr. Myungjae Lee and Matt Nowell for helping in setting up the EBSD experiments; S.C. and N.Y.K. would like to thank Mi-Sun Cho, Gyeong Ae Lee, and Ji Hyun Park for helping in the preparation of the TEM cross-section samples.

## ■ REFERENCES

(1) Li, P. C. Preparation of Single-Crystal Graphite from Melts. *Nature* **1961**, *192*, 864−865.

(2) Austerman, S. B.; Myron, S. M.; Wagner, J. W. Growth and Characterization of Graphite Single Crystals. *Carbon* **1967**, *5*, 549−557.

(3) Noda, T.; Sumiyoshi, Y.; Ito, N. Growth of Single Crystals of Graphite from a Carbon-Iron Melt. *Carbon* **1968**, *6*, 813−816.

(4) Inagaki, M. Highly Oriented Graphites. In *New Carbons - Control of Structure and Functions*;Elsevier Science: Oxford, U.K., 2000; pp 30−57 DOI: 10.1016/B978-008043713-2/50002-9.

(5) Amini, S.; Kalaantari, H.; Garay, J.; Balandin, A. A.; Abbaschian, R. Growth of Graphene and Graphite Nanocrystals from a Molten Phase. *J. Mater. Sci.* **2011**, *46*, 6255−6263.

(6) Karu, A. E.; Beer, M. Pyrolytic Formation of Highly Crystalline Graphite Films. *J. Appl. Phys.* **1966**, *37*, 2179−2181.

(7) Presland, A. E. B.; Walker, P. L., Jr. Growth of Single-Crystal Graphite by Pyrolysis of Acetylene over Metals. *Carbon* **1969**, *7*, 1−8.

(8) Yudasaka, M.; Klkuchi, R.; Matsui, T.; Ohki, Y.; Ota, E.; Yoshimura, S. Graphite Film Formation by Chemical Vapor Deposition on Ni Coated Sapphire. *Carbon* **1996**, *34*, 763−767.

(9) Cai, W. W.; Zhu, Y.; Li, X.; Piner, R. D.; Ruoff, R. S. Large Area Few-Layer Graphene/Graphite Films as Transparent Thin Conducting Electrodes. *Appl. Phys. Lett.* **2009**, *95*, 123115.

(10) Cao, H.; Yu, Q.; Colby, R.; Pandey, D.; Park, C. S.; Lian, J.; Zemlyanov, D.; Childres, I.; Drachev, V.; Stach, E. A.; Hussain, M.; Li, H.; Pei, S. S.; Chen, Y. P. Large-Scale Graphitic Thin Films Synthesized on Ni and Transferred to Insulators: Structural and Electronic Properties. *J. Appl. Phys.* **2010**, *107*, No. 044310.

(11) Chen, S.; Cai, W.; Piner, R. D.; Suk, J. W.; Wu, Y.; Ren, Y.; Kang, J.; Ruoff, R. S. Synthesis and Characterization of Large-Area Graphene and Graphite Films on Commercial Cu-Ni Alloy Foils. *Nano Lett.* **2011**, *11*, 3519−3525.

(12) Cheng, L.; Yun, K.; Lucero, A.; Huang, J.; Meng, X.; Lian, G.; Nam, H. S.; Wallace, R. M.; Kim, M.; Venugopal, A.; Colombo, L.; Kim, J. Low Temperature Synthesis of Graphite on Ni Films using Inductively Coupled Plasma Enhanced CVD. *J. Mater. Chem. C* **2015**, *3*, 5192−5198.

(13) Zheng, Q. Y.; Braun, P. V.; Cahill, D. G. Thermal Conductivity of Graphite Thin Films Grown by Low Temperature Chemical Vapor Deposition on Ni (111). *Adv. Mater. Interfaces* **2016**, *3*, 1600234.

(14) Hu, Q.; Kim, S. G.; Shin, D. W.; Kim, T. S.; Nam, K. B.; Kim, M. J.; Chun, H. C.; Yoo, J. B. Large-Scale Nanometer-Thickness Graphite Films Synthesized on Polycrystalline Ni Foils by Two-Stage Chemical Vapor Deposition Process. *Carbon* **2017**, *113*, 309−317.

(15) Kim, T.-S.; Shin, D.-W.; Kim, S.-G.; Kim, M. J.; Yoo, J.-B. Large Area Nanometer Thickness Graphite Freestanding Film Without Transfer Process. *Chem. Phys. Lett.* **2017**, *690*, 101−104.

(16) Hu, Q.; Kim, G.; Nam, K.-B.; Yeo, J.-H.; Kim, T.-S.; Kim, M.-J.; Yoo, J.-B. A Way to Improve the Uniformity of Nanometer-Thickness Graphite Film Synthesized on Polycrystalline Ni Substrate: From Large Grain to Small Grain. *Carbon* **2019**, *144*, 410−416.

(17) Kato, R.; Hasegawa, M. Fast Synthesis of Thin Graphite Film with High-Performance Thermal and Electrical Properties Grown by Plasma CVD using Polycrystalline Nickel Foil at low temperature. *Carbon* **2019**, *141*, 768−773.

(18) Moore, A. W. Highly oriented pyrolytic graphite. In *Chemistry and Physics of Carbon*; Walker, P. L., Jr.; Thrower, P. A., Eds.; Dekker: New York, 1973; Vol. *11*, pp 69−187.

(19) Shelton, J. C.; Patil, H. R.; Blakely, J. M. Equilibrium Segregation of Carbon to a Nickel (111) Surface - Surface Phase-Transition. *Surf. Sci.* **1974**, *43*, 493−520.

(20) Mojica, J. F.; Levenson, L. L. Bulk-to-Surface Precipitation and Surface-Diffusion of Carbon on Polycrystalline Nickel. *Surf. Sci.* **1976**, *59*, 447−460.

(21) Eizenberg, M.; Blakely, J. M. Carbon Interaction with Nickel Surfaces - Monolayer Formation and Structural Stability. *J. Chem. Phys.* **1979**, *71*, 3467−3477.

(22) Fujita, D.; Homma, T. Surface Precipitation of Graphite Layers on Carbon-Doped Nickel and their Stabilization Effect against Chemisorption and Initial Oxidation. *Surf. Interface Anal.* **1992**, *19*, 430−434.

(23) Fujita, D.; Yoshihara, K. Surface Precipitation Process of Epitaxially Grown Graphite (0001) Layers on Carbon-Doped Nickel(111) Surface. *J. Vac. Sci. Technol. A* **1994**, *12*, 2134−2139.

(24) Hwang, J.-W. Thermal Expansion of Nickel and Iron, and the Influence of Nitrogen on the Lattice Parameter of Iron at the Curie temperature. M.S. Theses, University of Missouri Rolla, 1972.

(25) Kellett, E. A.; Richards, B. P. The Thermal Expansion of Graphite within the Layer Planes. *J. Nucl. Mater.* **1964**, *12*, 184−192.

(26) Morgan, W. C. Thermal-Expansion Coefficients of Graphite Crystals. *Carbon* **1972**, *10*, 73−79.

(27) Zhu, W.; Low, T.; Perebeinos, V.; Bol, A. A.; Zhu, Y.; Yan, H.; Tersoff, J.; Avouris, P. Structure and Electronic Transport in Graphene Wrinkles. *Nano Lett.* **2012**, *12*, 3431−3436.

(28) Vasić, B.; Zurutuza, A.; Gajić, R. Spatial Variation of Wear and Electrical Properties across Wrinkles in Chemical Vapour Deposition Graphene. *Carbon* **2016**, *102*, 304−310.

(29) Deng, S.; Berry, V. Wrinkled, Rippled and Crumpled Graphene: an Overview of Formation Mechanism, Electronic Properties, and Applications. *Mater. Today* **2016**, *19*, 197−212.

(30) Zhang, Y.; Fu, Q.; Cui, Y.; Mu, R.; Jin, L.; Bao, X. Enhanced Reactivity of Graphene Wrinkles and their Function as Nanosized Gas Inlets for Reactions under Graphene. *Phys. Chem. Chem. Phys.* **2013**, *15*, 19042−19048.

(31) Deng, S.; Rhee, D.; Lee, W. K.; Che, S.; Keisham, B.; Berry, V.; Odom, T. W. Graphene Wrinkles Enable Spatially Defined Chemistry. *Nano Lett.* **2019**, *19*, 5640−5646.

(32) Deng, B.; Pang, Z.; Chen, S.; Li, X.; Meng, C.; Li, J.; Liu, M.; Wu, J.; Qi, Y.; Dang, W.; Yang, H.; Zhang, Y.; Zhang, J.; Kang, N.; Xu,

H.; Fu, Q.; Qiu, X.; Gao, P.; Wei, Y.; Liu, Z.; Peng, H. Wrinkle-Free Single-Crystal Graphene Wafer Grown on Strain-Engineered Substrates. *ACS Nano* **2017**, *11*, 12337−12345.

(33) Li, B. W.; Luo, D.; Zhu, L.; Zhang, X.; Jin, S.; Huang, M.; Ding, F.; Ruoff, R. S. Orientation-Dependent Strain Relaxation and Chemical Functionalization of Graphene on a Cu(111) Foil. *Adv. Mater.* **2018**, *30*, 1706504.

(34) Choi, J. K.; Kwak, J.; Park, S. D.; Yun, H. D.; Kim, S. Y.; Jung, M.; Kim, S. Y.; Park, K.; Kang, S.; Kim, S. D.; Park, D. Y.; Lee, D. S.; Hong, S. K.; Shin, H. J.; Kwon, S. Y. Growth of Wrinkle-Free Graphene on Texture-Controlled Platinum Films and Thermal-Assisted Transfer of Large-Scale Patterned Graphene. *ACS Nano* **2015**, *9*, 679−686.

(35) Lee, J. H.; Lee, E. K.; Joo, W. J.; Jang, Y.; Kim, B. S.; Lim, J. Y.; Choi, S. H.; Ahn, S. J.; Ahn, J. R.; Park, M. H.; Yang, C. W.; Choi, B. L.; Hwang, S. W.; Whang, D. Wafer-Scale Growth of Single-Crystal Monolayer Graphene on Reusable Hydrogen-Terminated Germanium. *Science* **2014**, *344*, 286−289.

(36) Zhang, X.; Wu, T.; Jiang, Q.; Wang, H.; Zhu, H.; Chen, Z.; Jiang, R.; Niu, T.; Li, Z.; Zhang, Y.; Qiu, Z.; Yu, G.; Li, A.; Qiao, S.; Wang, H.; Yu, Q.; Xie, X. Epitaxial Growth of 6 in. Single-Crystalline Graphene on a Cu/Ni (111) Film at 750 degrees C via Chemical Vapor Deposition. *Small* **2019**, *15*, No. e1805395.

(37) Poh, H. L.; Šimek, P.; Sofer, Z.; Pumera, M. Sulfur-Doped Graphene via Thermal Exfoliation of Graphite Oxide in H2S, SO2, or CS2 Gas. *ACS Nano* **2013**, *7*, 5262−5272.

(38) Hisham, M. W. M.; Bommaraju, T. V. Hydrogen Chloride. In*Kirk-Othmer Encyclopedia of Chemical Technology*; Kroschwitz, J. I.; Howe-Grant, M., Eds.; Wiley-Interscience: New York, 1995; Vol. *13*, pp 808−837.

(39) Gogotsi, Y.; Welz, S.; Ersoy, D. A.; McNallan, M. J. Conversion of Silicon Carbide to Crystalline Diamond-Structured Carbon at Ambient Pressure. *Nature* **2001**, *411*, 283−287.

(40) Welz, S.; Gogotsi, Y.; McNallan, M. J. Nucleation, Growth, and Graphitization of Diamond Nanocrystals during Chlorination of Carbides. *J. Appl. Phys.* **2003**, *93*, 4207−4214.

(41) Karlický, F.; Kumara Ramanatha Datta, K.; Otyepka, M.; Zbořil, R. Halogenated Graphenes: Rapidly Growing Family of Graphene Derivatives. *ACS Nano* **2013**, *7*, 6434−6464.

(42) Herraiz, M.; Dubois, M.; Batisse, N.; Hajjar-Garreau, S.; Simon, L. Large-Scale Synthesis of Fluorinated Graphene by Rapid Thermal Exfoliation of Highly Fluorinated Graphite. *Dalton Trans.* **2018**, *47*, 4596−4606.

(43) Gopalakrishnan, K.; Subrahmanyam, K. S.; Kumar, P.; Govindaraj, A.; Rao, C. N. R. Reversible chemical storage of halogens in few-layer graphene. *RSC Adv.* **2012**, *2*, 1605−1608.

(44) Bouša, D.; Luxa, J.; Mazánek, V.; Jankovský, O.; Sedmidubský, D.; Klímová, K.; Pumera, M.; Sofer, Z. Toward Graphene Chloride: Chlorination of Graphene and Graphene Oxide. *RSC Adv.* **2016**, *6*, 66884−66892.

(45) Yushin, G. N. A.; Gogotsi, Y. Carbide-derived Carbon. In *Nanomaterials Handbook*; 1st ed.; Gogotsi, Y., Ed.; Taylor and Francis: Boca Raton, 2006; pp 240−282.

(46) Presser, V.; Heon, M.; Gogotsi, Y. Carbide-Derived Carbons - From Porous Networks to Nanotubes and Graphene. *Adv. Funct. Mater.* **2011**, *21*, 810−833.

(47) Hirooka, A.; Habuka, H.; Takahashi, Y.; Kato, T. Formation and Removal of Carbon Film on Silicon Carbide Surface Using Chlorine Trifluoride Gas. *ECS J. Solid State Sci. Technol.* **2016**, *5*, P441−P445.

(48) Cançado, L. G.; Takai, K.; Enoki, T.; Endo, M.; Kim, Y. A.; Mizusaki, H.; Speziali, N. L.; Jorio, A.; Pimenta, M. A. Measuring the Degree of Stacking Order in Graphite by Raman Spectroscopy. *Carbon* **2008**, *46*, 272−275.

(49) Zarza, F. M. *Graphite EBSD Characterization in Compact Graphite Iron*. M.S. Thesis, Ghent University, Ghent, 2015−16.

(50) Theuwissen, K.; Lacaze, J.; Véron, M.; Laffont, L. Nano-Scale Orientation Mapping of Graphite in Cast Irons. *Mater. Charact.* **2014**, *95*, 187−191.

(51) Woo, Y.; Kim, D.-C.; Jeon, D.-Y.; Chung, H.-J.; Shin, S.-M.; Li, X.-S.; Kwon, Y.-N.; Seo, D.-H.; Shin, J.; Chung, U.-I.; Seo, S. In *Large-Grained and Highly-Ordered Graphene Synthesized by Radio-Frequency Plasma Enhanced Chemical Vapor Deposition*, Graphene and Emerging-Materials for post CMOS applications, San Francisco; Obeng, Y.; De Gent, S.; Srinivasan, P.; Misra, D.; Iwai, H.; Karim, Z.; Hess, D. W.; Grebel, H., Eds.; The Electrochemical Society, 2009; pp 111−114.

(52) Yoshida, A.; Hishiyama, Y.; Kaburagi, Y., *Characterization of Crystal Grain Shape and Crystal Axis Orientation Mapping on Surface of HOPG using Electron Backscatter Diffraction*, 2004.

(53) *Electron Backscatter Diffraction in Materials Science*. Schwartz, A. J.; Kumar, M.; Brent, A. L. Eds.; Springer US: New York, 2009; Vol. *1*.

(54) Franklin, R. E. The Structure of Graphitic Carbons. *Acta Cryst.* **1951**, *4*, 253−261.

(55) Johansson, A. S.; Lu, J.; Carlsson, J. O. TEM Investigation of CVD Graphite on Nickel. *Thin Solid Films* **1994**, *252*, 19−25.

(56) Garcia, A. P.; Pugno, N.; Buehler, M. J. Superductile, Wavy Silica Nanostructures Inspired by Diatom Algae. *Adv. Eng. Mater.* **2011**, *13*, B405−B414.

(57) Sha, Z. D.; Quek, S. S.; Pei, Q. X.; Liu, Z. S.; Wang, T. J.; Shenoy, V. B.; Zhang, Y. W. Inverse pseudo Hall-Petch relation in polycrystalline graphene. *Sci. Rep.* **2014**, *4*, 5991.

(58) Song, Z.; Artyukhov, V. I.; Yakobson, B. I.; Xu, Z. Pseudo Hall-Petch Strength Reduction in Polycrystalline Graphene. *Nano Lett.* **2013**, *13*, 1829−1833.

(59) Wang, Y.; Zheng, Y.; Xu, X.; Dubuisson, E.; Bao, Q.; Lu, J.; Loh, K. P. Electrochemical Delamination of CVD-Grown Graphene Film: Toward the Recyclable Use of Copper Catalyst. *ACS Nano* **2011**, *5*, 9927−9933.

# Supporting Information

# Synthesis of Highly Oriented Graphite Films with a Low Wrinkle Density and Near-Millimeter Scale Lateral Grains

Shahana Chatterjee,[1*] Na Yeon Kim,[1] Nicola Maria Pugno,[2,3,4] Mandakini Biswal,[1] Benjamin V. Cunning,[1] Min Goo,[1,5] Sunghwan Jin,[1] Sun Hwa Lee,[1] Zonghoon Lee,[1,6] Rodney S. Ruoff[1,5,6,7*]

chatterjee.shahana@gmail.com, ruofflab@gmail.com, rsruoff@ibs.re.kr

[1] Center for Multidimensional Carbon Materials (CMCM), Institute for Basic Science (IBS), Ulsan 44919, Republic of Korea

[2] Laboratory of Bio-inspired, Bionic, Nano, Meta Materials & Mechanics, Department of Civil, Environmental and Mechanical Engineering, Università di Trento, via Mesiano, 77, I-38123 Trento, Italy

[3] School of Engineering and Materials Science, Queen Mary University of London, Mile End Road, London E1 4NS, UK

[4] Fondazione E. Amaldi, Ket Lab, Via del Politecnico snc, 00133 Rome, Italy.

[5] Department of Chemistry, Ulsan National Institute of Science and Technology (UNIST), Ulsan 44919, Republic of Korea

[6] School of Materials Science and Engineering, Ulsan National Institute of Science and Technology (UNIST), Ulsan 44919, Republic of Korea

[7] School of Energy and Chemical Engineering, Ulsan National Institute of Science and Technology (UNIST), Ulsan 44919, Republic of Korea

## Experimental Details

### ***Materials***

Nickel foils of different thicknesses and purities were purchased from Alfa-Aesar (100 µm thickness and 99.994% purity; 25 µm thickness and 99.99% purity). Natural graphite crystals were obtained from Prof. John Jaszczak (Michigan Technological University & Naturally Graphite). Grade-A and Grade-B HOPG were purchased from SPI (USA), XFNano (China) and Optigraph (Germany). Ultra-high purity grade (99.999%) $CH_4$, $H_2$, and Ar gases were used for all graphite growth processes. The gases were additionally purified using respective purifiers before use. Anhydrous $Cl_2$ gas (99.999%) was used as received.

### ***Characterization***

AFM was performed on a Bruker Dimension Icon system. SEM imaging was performed on a Verios 460 scanning electron microscope and EBSD scans were obtained using a Hikari camera from Ametek attached to this SEM. TEM images and EELS spectra were recorded on a probe corrected FEI Titan G2 60-300 instrument with an electron monochromator at 80 kV. XRD data was obtained on a Rigaku SmartLab powder X-ray diffractometer. Confocal Raman spectroscopy was performed on a WiTEC instrument using a 532 nm laser and 600 g/mm or 1800 g/mm gratings. XPS measurements were acquired on a Thermo Scientific ESCALAB 250 Xi instrument. ICP-OES data was acquired on a Varian 700-ES instrument.

### ***Sample Preparation for EBSD***

Flakes were extracted from natural graphite crystals or HOPG pieces by pressing them to sticky notes followed by removal of the adhesive sticky notes with HPLC grade acetone. The free-floating pieces were then transferred to silicon wafers and dried in an oven at 80–100 °C. All the natural graphite or HOPG flakes thus obtained and Type A and Type B graphite films on silicon wafers were pressed a few times using a Kolami 330 S roller prior to performing EBSD scans.

## ***Sample Preparation for Cross-section TEM***

Regions of interest (ROI) from selected graphite films on Si wafers or Ni substrates were first coated with a Ti film and then with a black marker pen outside the SEM chamber. Once inside the SEM chamber (Helios 450HP) the ROI was coated with amorphous carbon and then sectioned with a focused ion beam (FIB) of gallium ions at 30 kV, and at an angle of ±2° to the surface normal. After transferring this wedge to a half grid, the final milling was also done with a gallium FIB sequentially at 30 kV, 5 kV and 2 kV and *without tilting*. This procedure has been adopted from a previous study by Colby et. al. to minimize ion beam damage to the graphite film.[1]

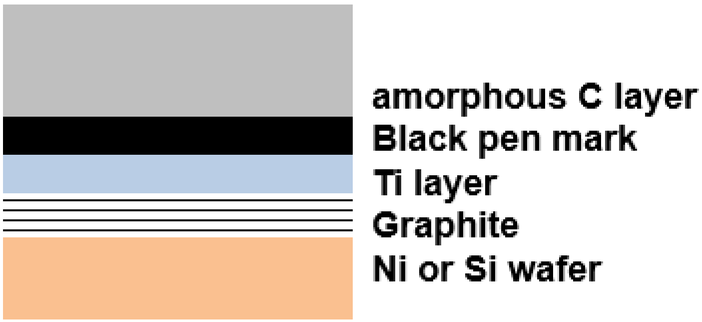

**Figure S1**. Figure representing a cross-section sample prepared from a graphite film for TEM imaging.

**Table S1**. Predicted number of graphene layers precipitated on each side of a 100 µm Ni foil, based on thermodynamic solubility data for C in polycrystalline Ni,[2] from a $T_{dissolution}$ temperature of 1150 °C. The calculation is based on the C solubility difference between $T_{dissolution}$ and $T_{precipitation}$.

Number of graphene layers

= (C solubility difference $T_{dissolution}$ and $T_{precipitation}$)*(Ni thickness)* unit cell area/ # of atoms per unit cell

where, unit cell area = $3\sqrt{3}/2*a^{\wedge 2}$, and, atoms per unit cell = 2, for each graphene layer.

For a 100 µm Ni foil, it has been assumed that half the excess carbon precipitates on each side, hence, thickness = 50 µm.

Film thickness = Number of graphene layers*(0.335 nm)

| $T_{precipitation}$ (°C) | Number of graphene layers | Film Thickness (nm) |
|---|---|---|
| **20 (RT)** | **2405.359456** | **805.7954177** |
| 600 | 2118.984173 | 709.8596978 |
| 650 | 2019.596995 | 676.5649932 |
| 700 | 1901.359476 | 636.9554246 |
| 750 | 1763.831489 | 590.8835488 |
| 800 | 1606.886348 | 538.3069267 |
| 850 | 1430.667738 | 479.2736922 |
| 900 | 1235.545145 | 413.9076235 |
| 950 | 1022.070829 | 342.3937277 |
| **1000** | **790.9401518** | **264.9649508** |
| 1050 | 542.9562114 | 181.8903308 |
| 1100 | 278.9991366 | 93.46471075 |

Thus, the maximum predicted film thickness is ~806 nm; this should be compared to Type B films. Type A films precipitated at 1000 °C are expected to have thicknesses around ~265 nm.

***AFM analysis of wrinkles***

**Figure S2** depicts what has been defined as the height of a wrinkle and how it has been measured using AFM. Generally, AFM analysis is performed on the side that was away from the Ni substrate during growth (outer side, **Figure S3**). However, select films have been flipped over and AFM has been performed on the side that was adjacent to the Ni surface (inner side). They show similar wrinkling patterns (**Figure S4**).

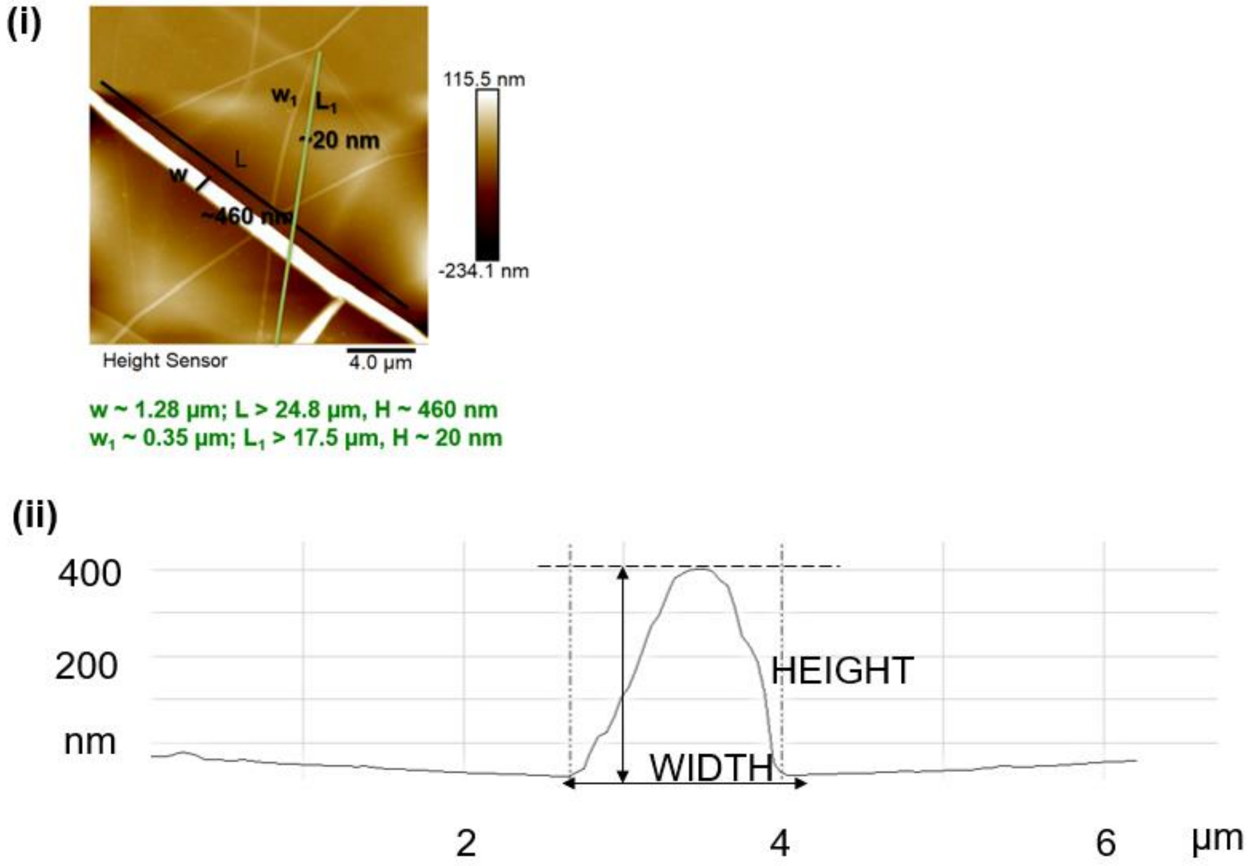

**Figure S2**. AFM analysis showing wrinkles on a graphite thin film characterized by their height H, length L and width w: (i) image, (ii) a typical line scan.

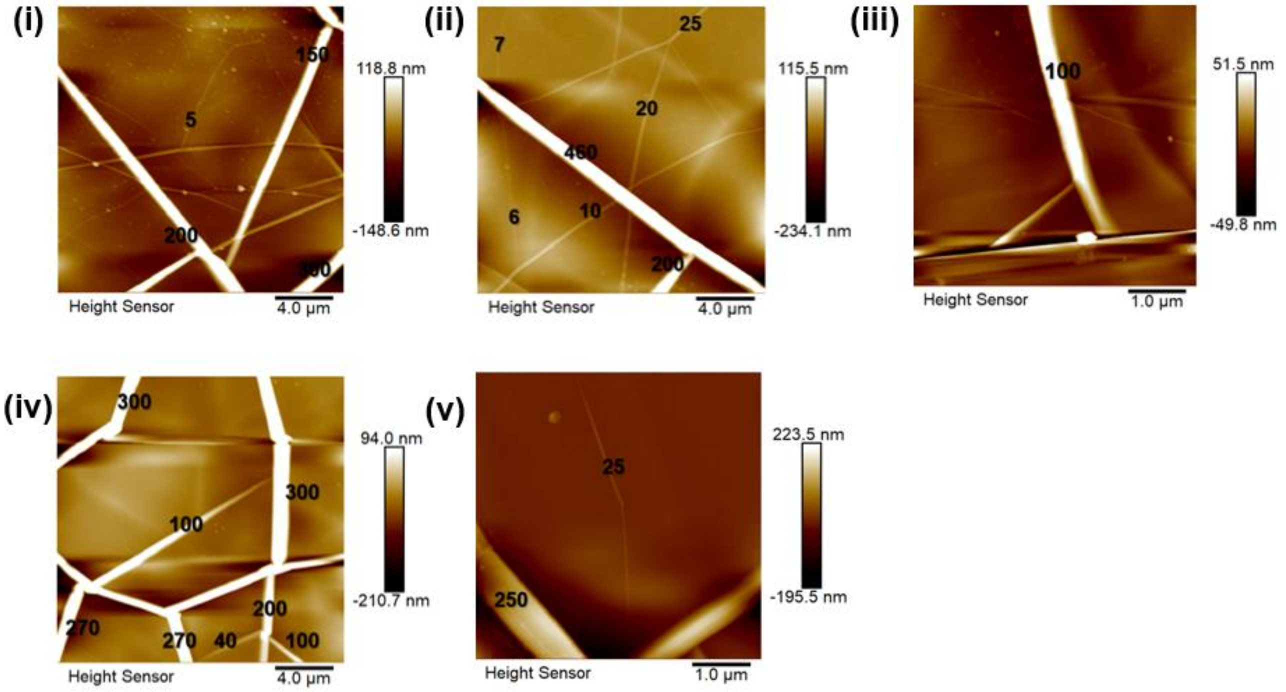

**Figure S3**. AFM analysis of Type A film on their 'outer' side. Numbers across the wrinkles represent their heights in nm. Scan areas: (i)-(ii), (iv): 20x20 µm$^2$; (iii), (v): 5x5 µm$^2$.

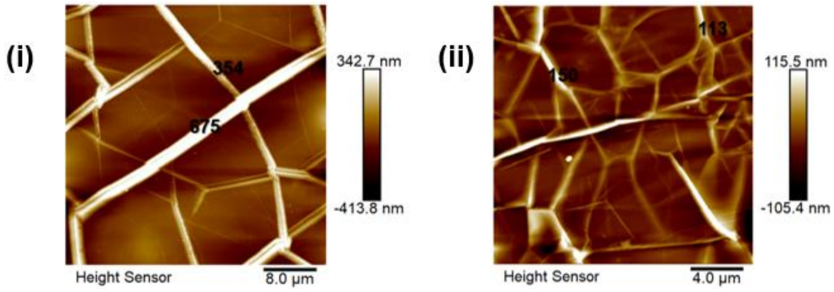

**Figure S4**. AFM analysis of Type A film on their 'inner' side. Numbers across the wrinkles represent their heights in nm. Scan areas: (i): 40x40 µm$^2$; (ii): 20x20 µm$^2$

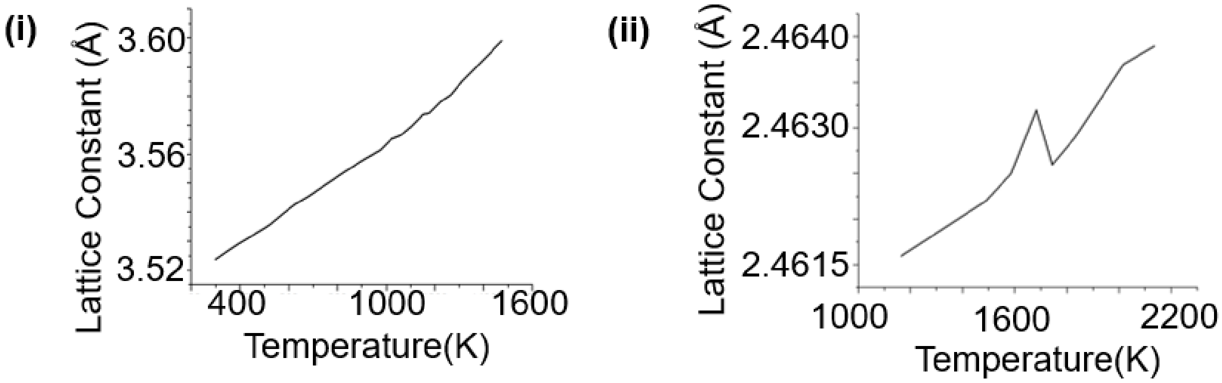

**Figure S5**. Variation in lattice parameters of (i) Ni, and, (ii) Graphite, with temperature. For face centered cubic (FCC) Ni this is the lattice parameter 'a' of its cubic unit cell, whereas, for graphite, this is the in-plane lattice parameter.[3-5]

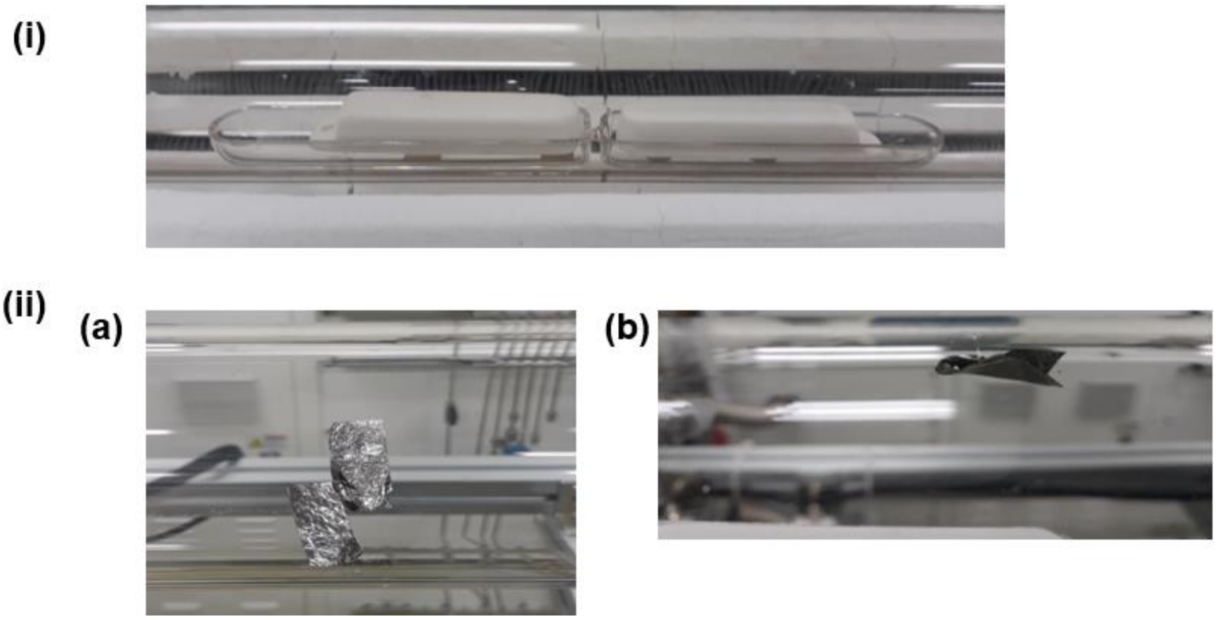

**Figure S6**. (i) Picture of Ni foils on quartz boats and alumina covers loaded in the reactor for synthesizing graphite films. (ii) (a)-(b) Graphite films that have flown away from the center to other parts of the reactor, from an experiment without protective lids.

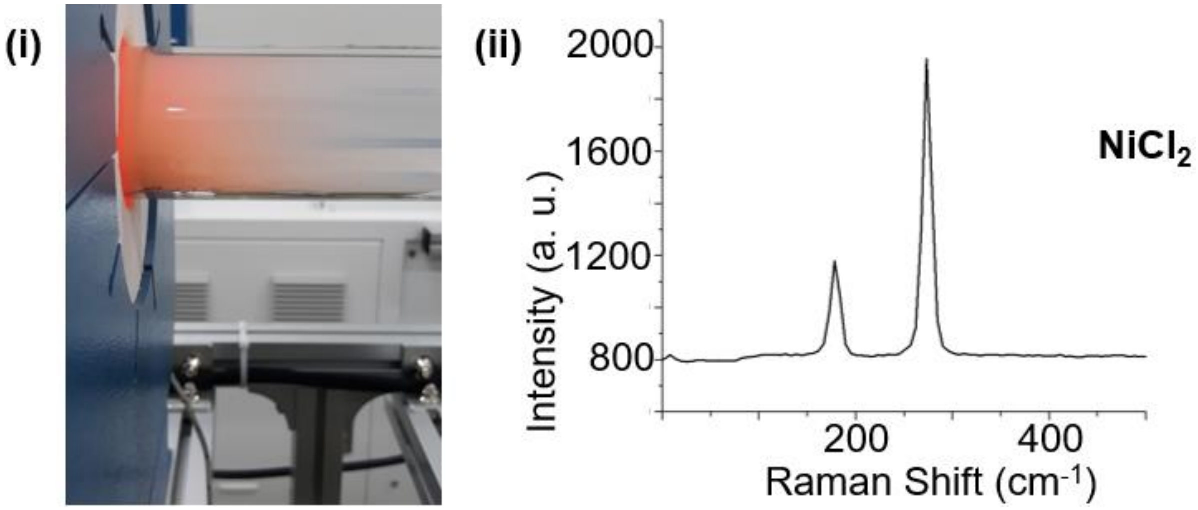

**Figure S7**. (i) Orange anhydrous $NiCl_2$ deposited on the cooler surfaces of the reactor (~500–600 ºC). (ii) Raman spectrum of anhydrous $NiCl_2$.[6]

**Evaluating the amount of Ni(0) or $NiCl_2$ in Type B films**

Magnet Test: At the end of an experiment, a magnet was brought close to a floating Type B film. If the film was not attracted by the magnet, it was tentatively considered to contain an insignificant amount of Ni(0) (**Figure S8**) residue.

**Table S2**. ICP-OES Data

| Sample# | Magnet Test | ICP-OES: Ni (% by weight) |
|---|---|---|
| 2-9-18 | No Ni(0) | -0.12 |
| 2-8-18 | No Ni(0) | -0.0013 |
| 2-25-19 | No Ni(0) | 1.01 |
| 2-6-18 | Ni(0) present | 98 |
| 2-5-19 | Ni(0) present | 38 |
| 3-16-19 | Ni(0) present | 89 |

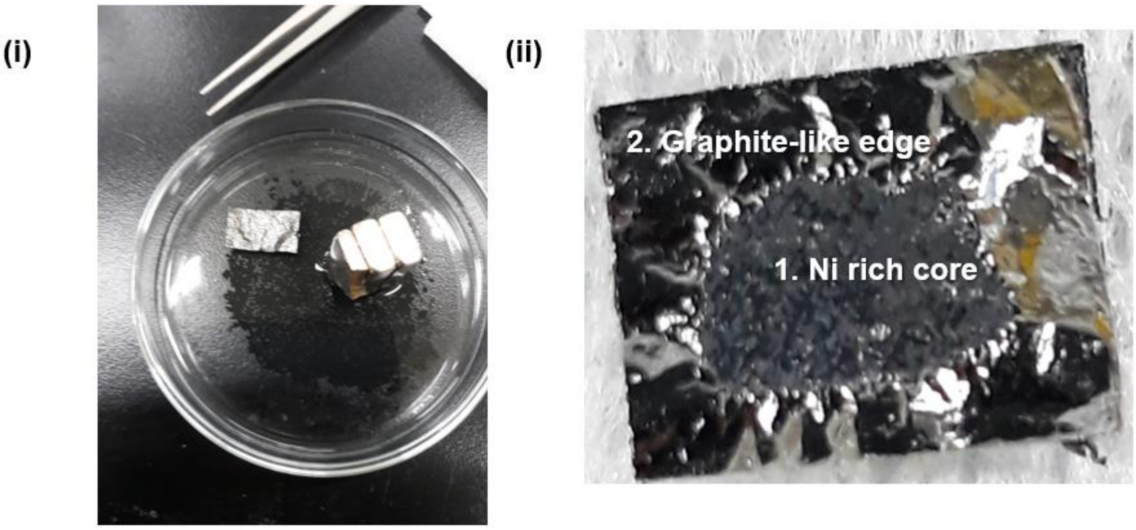

**Figure S8**. (i) A Type B graphite film floating in ethanol that is not attracted to the magnets indicating that it has an insignificant amount of metallic Ni(0) residue. (ii) A partially etched Ni-graphite sandwich: the core looks Ni rich while the edges look graphite like.

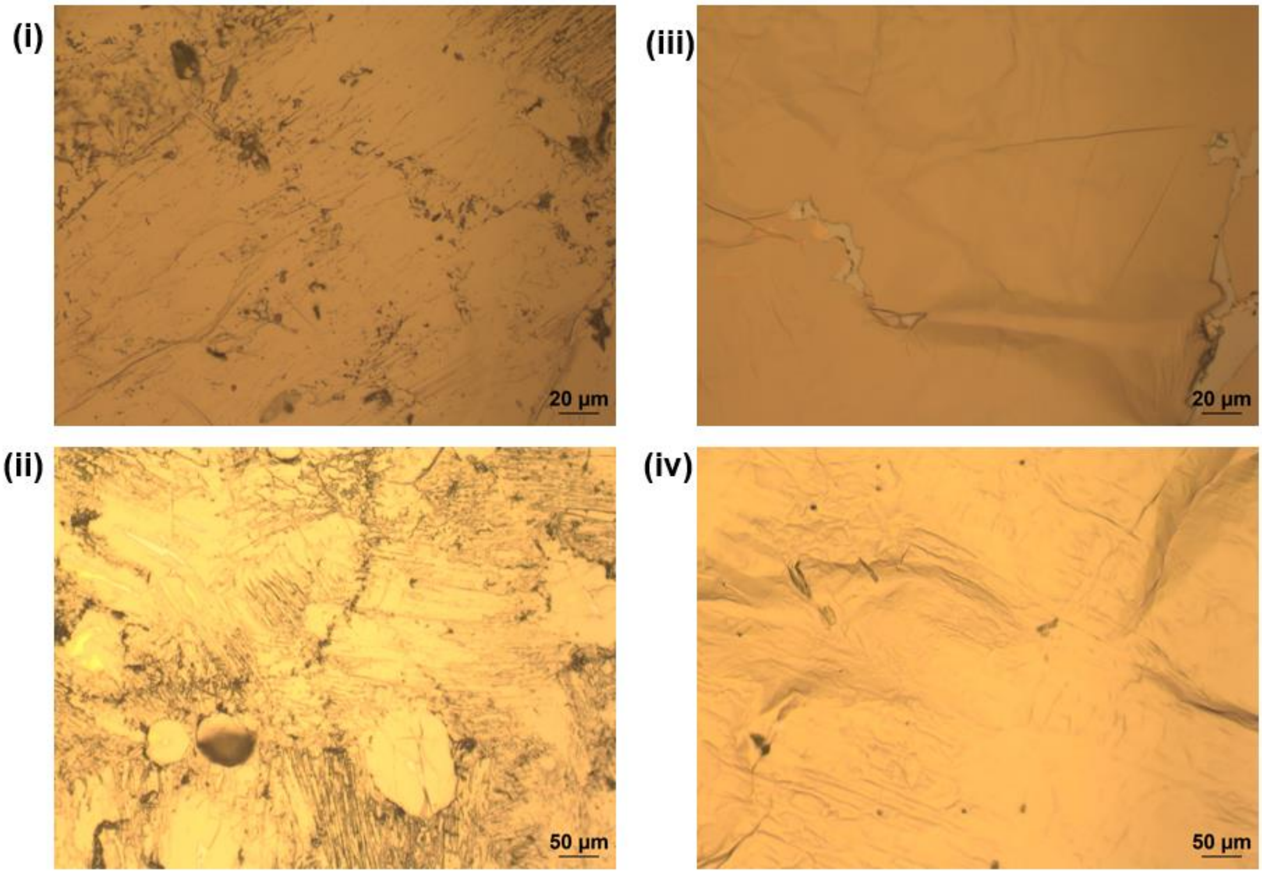

**Figure S9**. Optical images of Type B graphite films. Scale bars: 20 µm (i, iii); 50 µm (ii, iv).

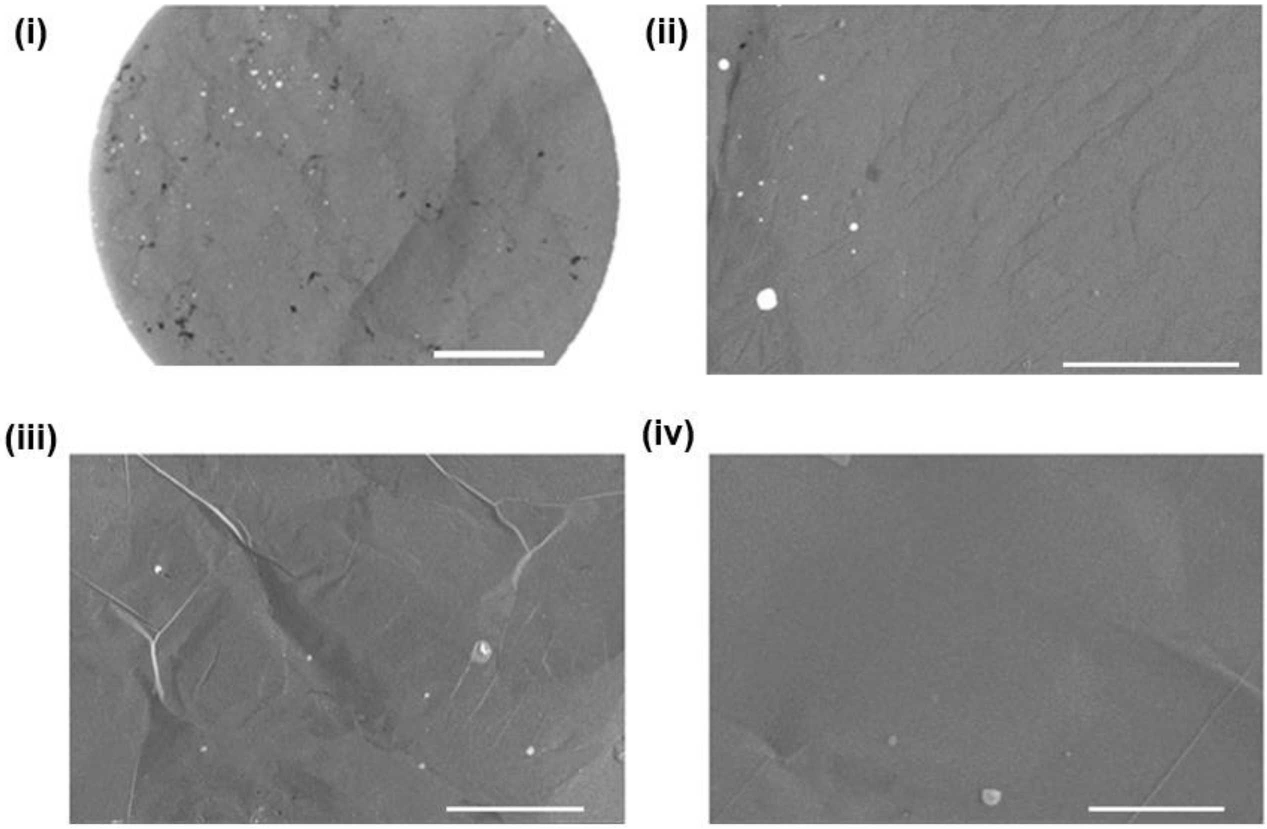

**Figure S10**. Additional SEM images of Type B graphite films. Scale bars: (i) 500 µm, (ii) 100 µm, (iii) 20 µm, (iv) 5 µm.

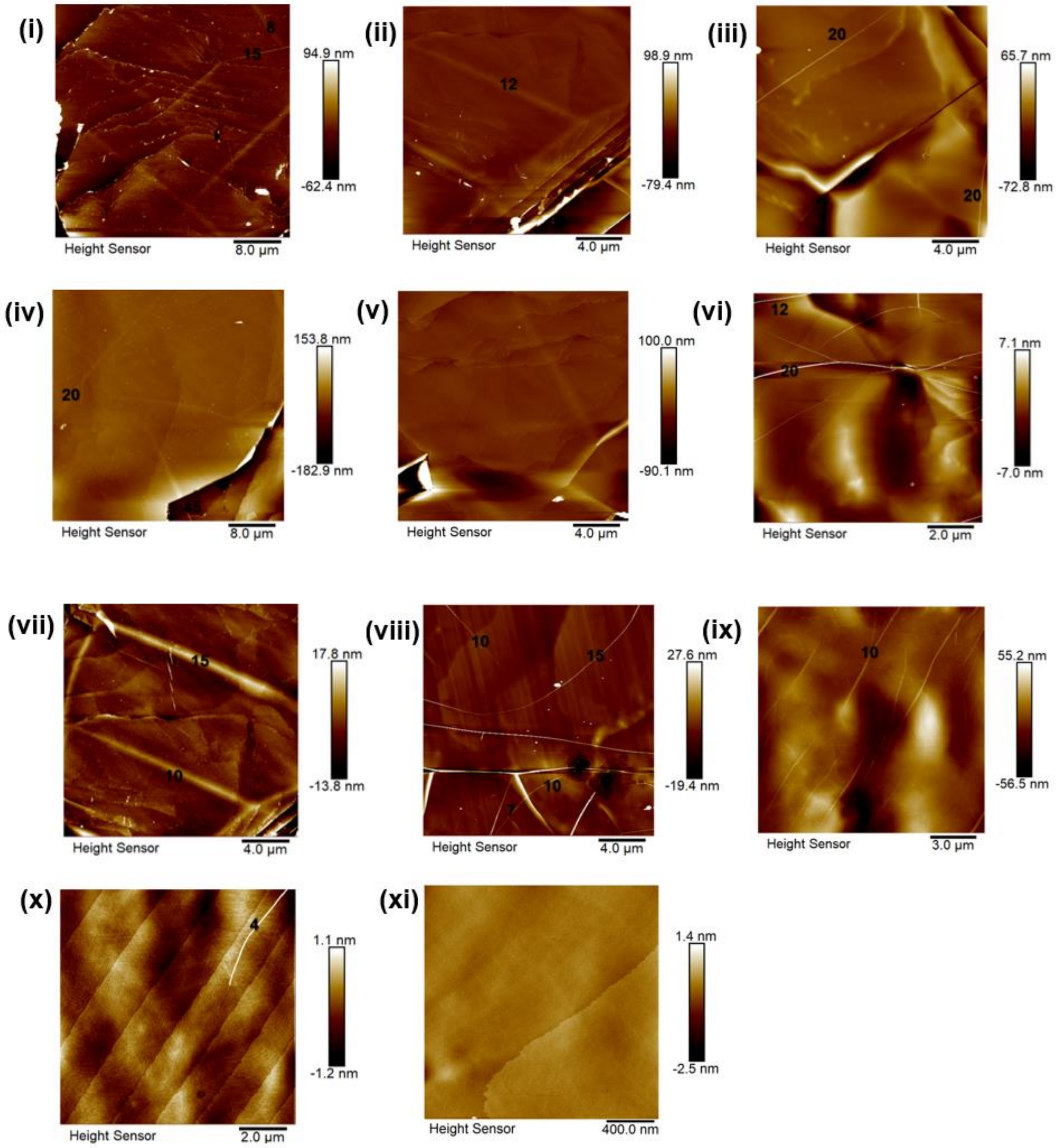

**Figure S11**. Additional AFM scans of Type B graphite films: (i), (iv): 40x40 µm$^2$, (ii)-(iii), (v), (vii) - (viii): 20x20 µm$^2$, (ix): 15x15 µm$^2$, (vi), (x): 10x10 µm$^2$, (xi): 2x2 µm$^2$. Numbers across the wrinkles denote their heights in nm.

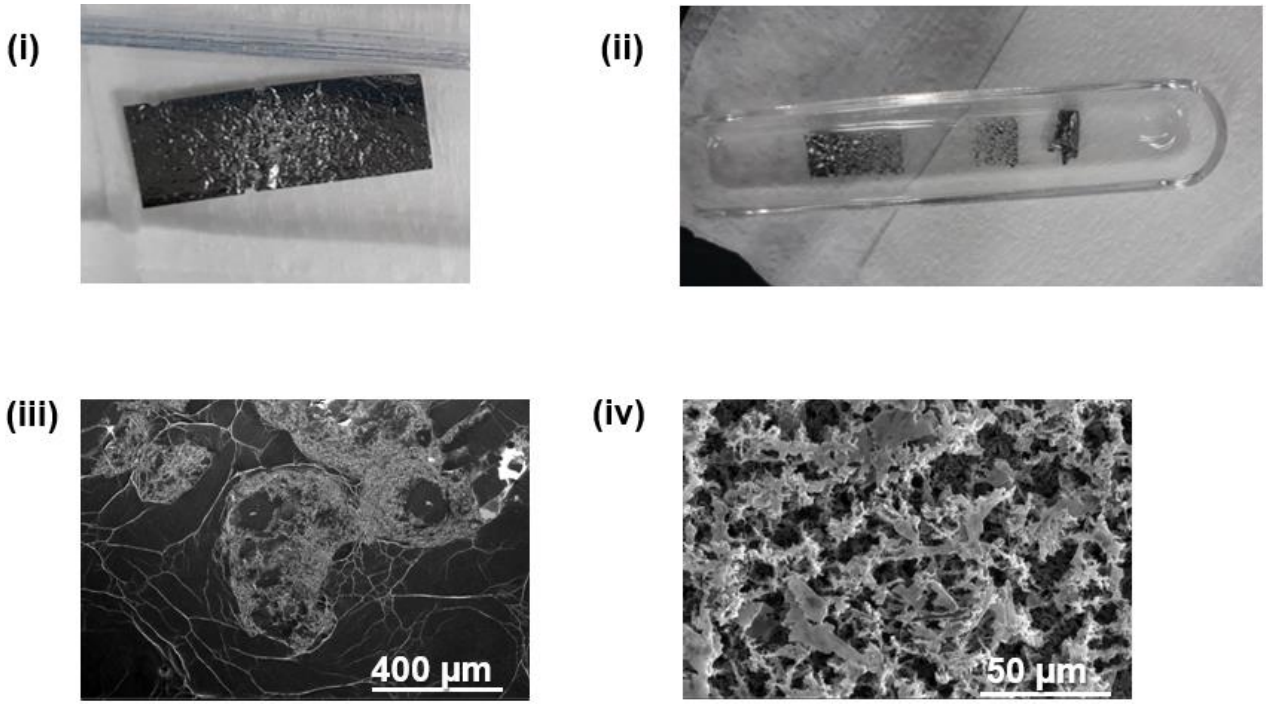

**Figure S12**. Damaged and crumpled graphite films formed by un-optimized $Cl_2$ etching: (i) – (ii) are optical images; (iii) – (iv) show SEM images of films with significant crumpling. Scale bars: (iii) 400 µm, (iv) 50 µm.

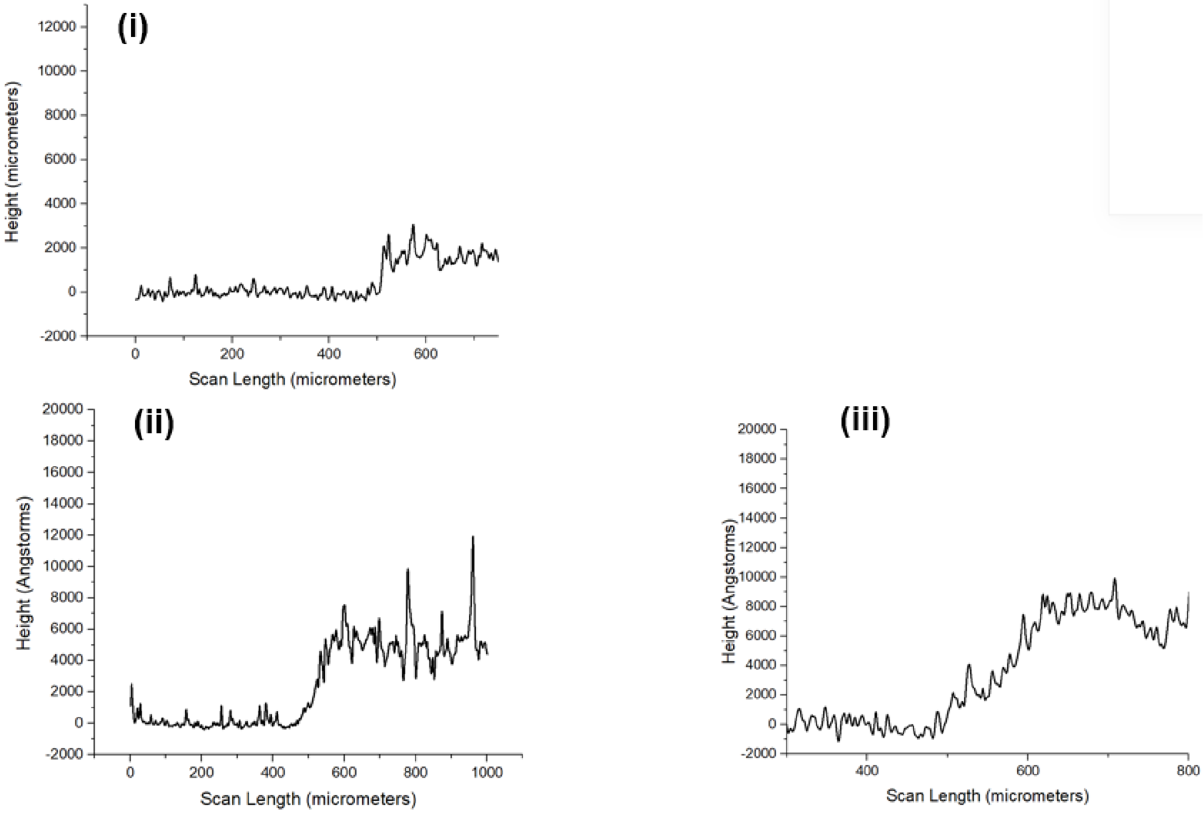

**Figure S13-I**. (i) Typical surface profilometry scans of a (i) Type A, and a (ii)-(iii) Type B graphite films. Heights are in Å. The thicknesses are similar to the calculated thicknesses in **Table S1**.

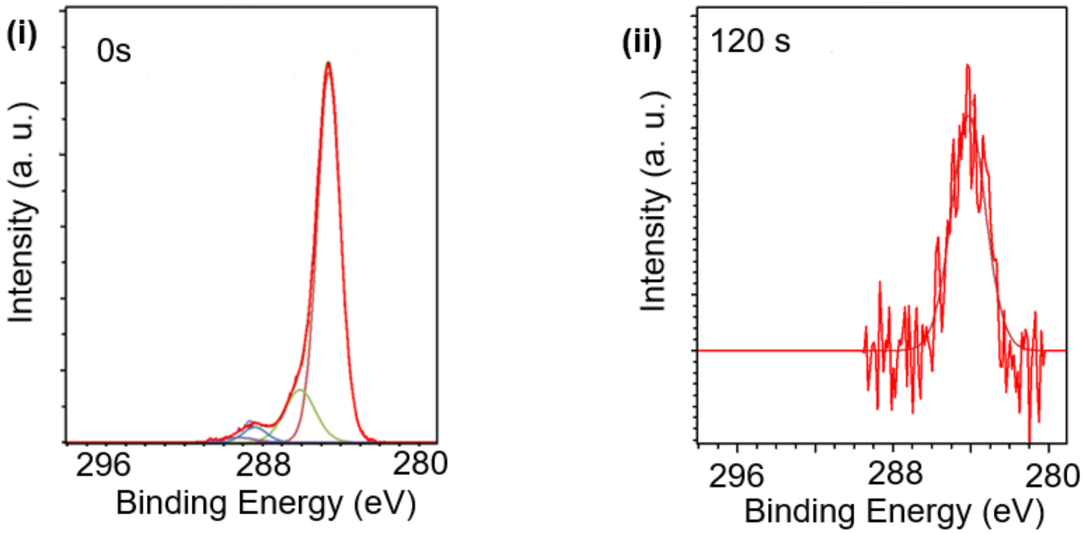

| Name | Position | FWHM | L. Sh. | Area | % Area |
|---|---|---|---|---|---|
| C-C, C-H | 284.61 | 1.39 | GL(30) | 155173.99 | 80.07 |
| C-O, C-OH | 286.08 | 1.84 | GL(30) | 29229.24 | 15.08 |
| C=O | 288.39 | 1.41 | GL(30) | 6451.63 | 3.33 |
| C(O)O | 289.29 | 2.05 | GL(30) | 2947.48 | 1.52 |

| Name | Position | FWHM | L. Sh. | Area | % Area |
|---|---|---|---|---|---|
| C-C, C-H | 284.11 | 2.04 | GL(30) | 4672.26 | 100.00 |

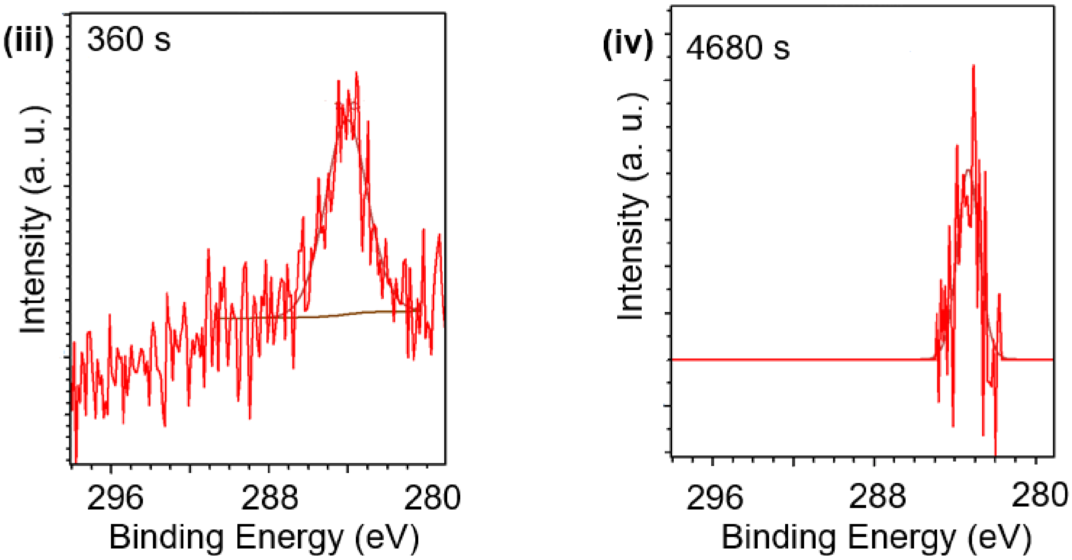

| Name | Position | FWHM | L. Sh. | Area | % Area |
|---|---|---|---|---|---|
| C-C, C-H | 284.08 | 2.51 | GL(30) | 4644.60 | 100.00 |

| Name | Position | FWHM | L. Sh. | Area | % Area |
|---|---|---|---|---|---|
| C-C, C-H | 283.33 | 1.25 | GL(30) | 1113.10 | 100.00 |

**Figure S13-II**. XPS depth profile for C in a Ni foil from **process A** (after graphite films have been removed), showing the presence of atomic C in the bulk. The Ni foil was etched with an argon ion beam and XPS signals were collected after each etching step. The above figure shows XPS spectra from the surface (0 s etching), and after etching for 120 s, 360 s and 4680 s.

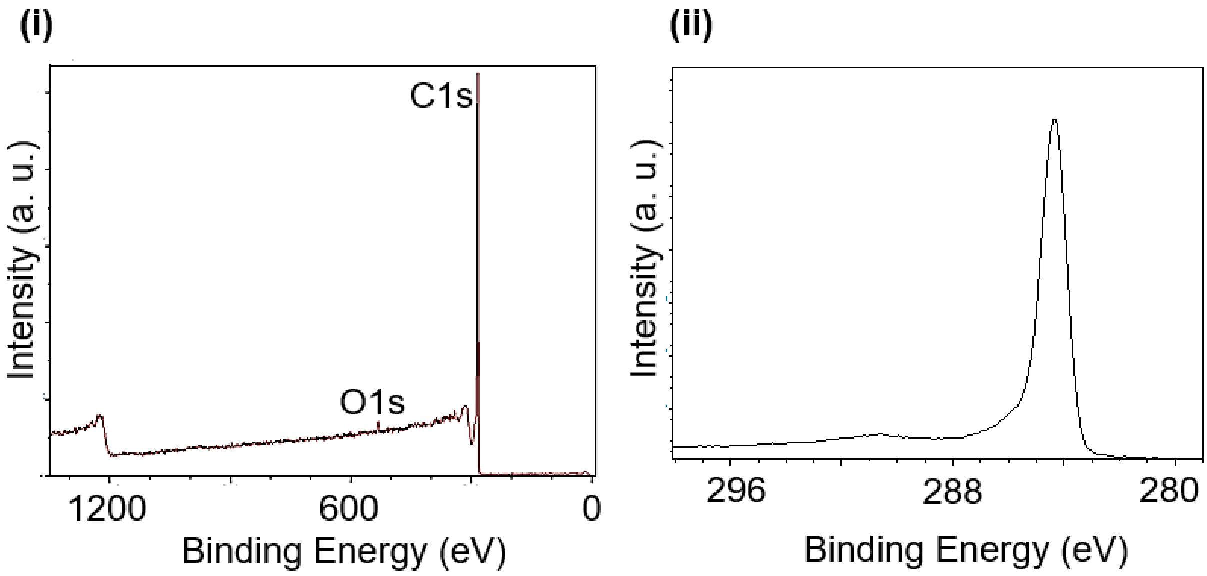

**Figure S14**. Typical XPS spectrum of a Type B graphite film confirming the presence of only $sp^2$ C in the film. (i) Survey spectrum, (ii) C1s peak.

## *Raman Spectroscopy of Graphite Films and HOPG*

**Table S3-(i)**: G peak fitting and calculation of $I_D/I_G$ ratios over the areas scanned (~100–2x10^4 μm$^2$).

Raman maps were recorded using a 532 nm laser at ~2–25 mW power and a 600 g/mm grating.

| Sample Details | $I_D/I_G$: Average (Median) | G: Average (Median)/cm$^{-1}$ | FWHM: Average (Median)/cm$^{-1}$ |
|---|---|---|---|
| HOPG-A (XFNANO) | 0.02 (0.017) | 1583 (1583) | 15.48(15.28) |
| Sample 1 (Type A, wrinkled) | 0.12(0.082) | 1580(1580) | 15(15) |
| Sample 1 (Type B) | 0.04 (0.035) | 1587(1587) | 15(15) |
| Sample 2 (Type B) | 0.06 (0.057) | 1581(1581) | 15.7(15.4) |
| Sample 3 (Type B) | 0.09(0.07) | 1583(1583) | 15.19(14.97) |
| Sample 4 (Type B) | 0.06(0.04) | 1579(1579) | 14.29(14.13) |

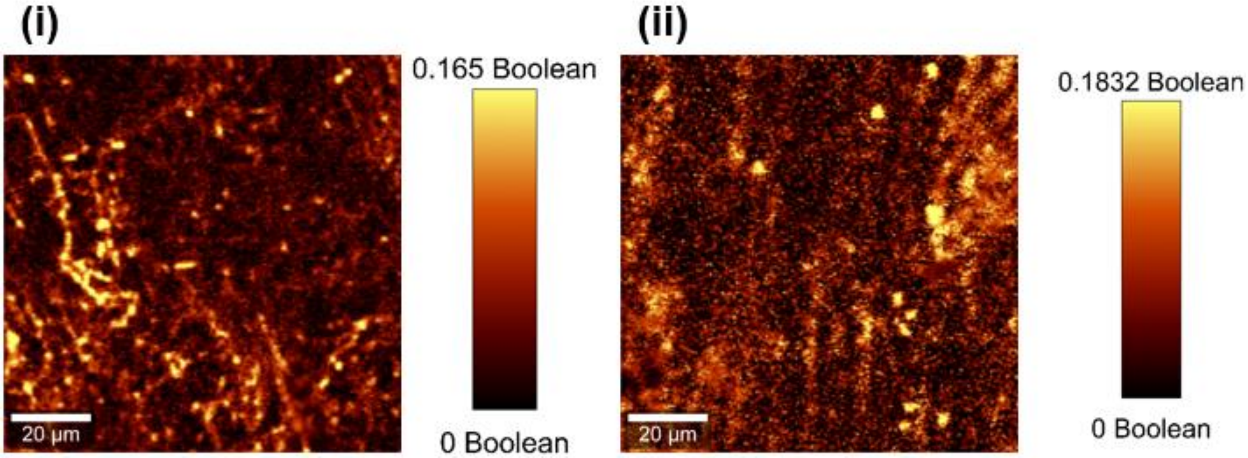

**Figure S15.** $I_D/I_G$ maps for (i, ii) two different Type B films (100x100 μm$^2$).

A method by Cancado et al. has been used to determine the AB stacking order from the 2D peak.[7] Briefly, this involved fitting the 2D peaks with a $2D_1$ peak at ~2714 cm$^{-1}$, a $2D_2$ peak at ~2670 cm$^{-1}$ and a $2D_T$ peak (T: turbostratic peak) at ~2698 cm$^{-1}$ (**Figure S16**). The AB stacking order over the scanned area was then calculated as the ratio of the area of the $2D_2$ peak to the sum of the areas of the $2D_2$ and $2D_T$ peaks and compared to HOPG. For a Grade A HOPG sample with near complete AB stacking of the graphene layers, this 2D area ratio was ~1.0. Hence, scanned areas from the graphite films that had an area ratio equal or close to 1 were considered to be AB stacked.

**Table S3-(ii)**: 2D peak fitting and calculation of percentage of AB stacking over the areas scanned (~100 μm$^2$). Raman maps were recorded using a 532 nm laser at ~25–30 mW power, a 100x objective lens and a 1800 g/mm grating.

| | **$D_1$: Average (median)/cm$^{-1}$** | **$D_2$: Average (median)/cm$^{-1}$** | **$D_T$: Average (median)/cm$^{-1}$** | **Areas ratios of $D_1$/( $D_T$ + $D_1$): Average (median)** |
|---|---|---|---|---|
| HOPG-A (XFNANO) | 2714(2714) | 2671(2672) | 2697(2696) | 1.0(1.0) |
| Sample A (Type B) | 2713(2714) | 2669(2669) | 2698(2698) | 1.01(1.02) |
| Sample B(Type B) | 2715(2715) | 2672(2672) | 2698(2700) | 1.0(1.0) |
| Sample C(Type B) | 2715(2715) | 2671(2671) | 2697(2695) | 0.98(0.99) |
| Sample 1 (Type A, wrinkled) | 2715(2716) | 2671(2672) | 2696(2695) | 0.96(0.97) |

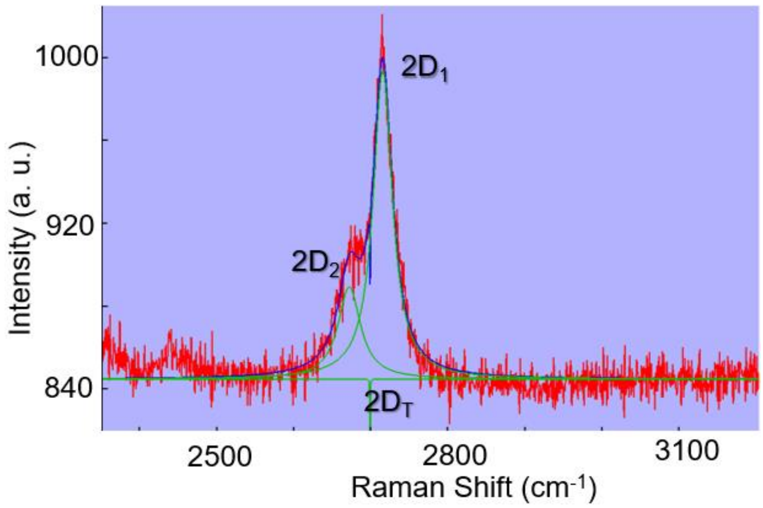

**Figure S16**. An example of a 2D peak from a Type B graphite film being fitted with a 2D$_1$, a 2D$_2$ and a 2D$_T$ peak. As the area under the 2D$_2$ peak is negligible, the graphite film at this point may be considered to be AB stacked.

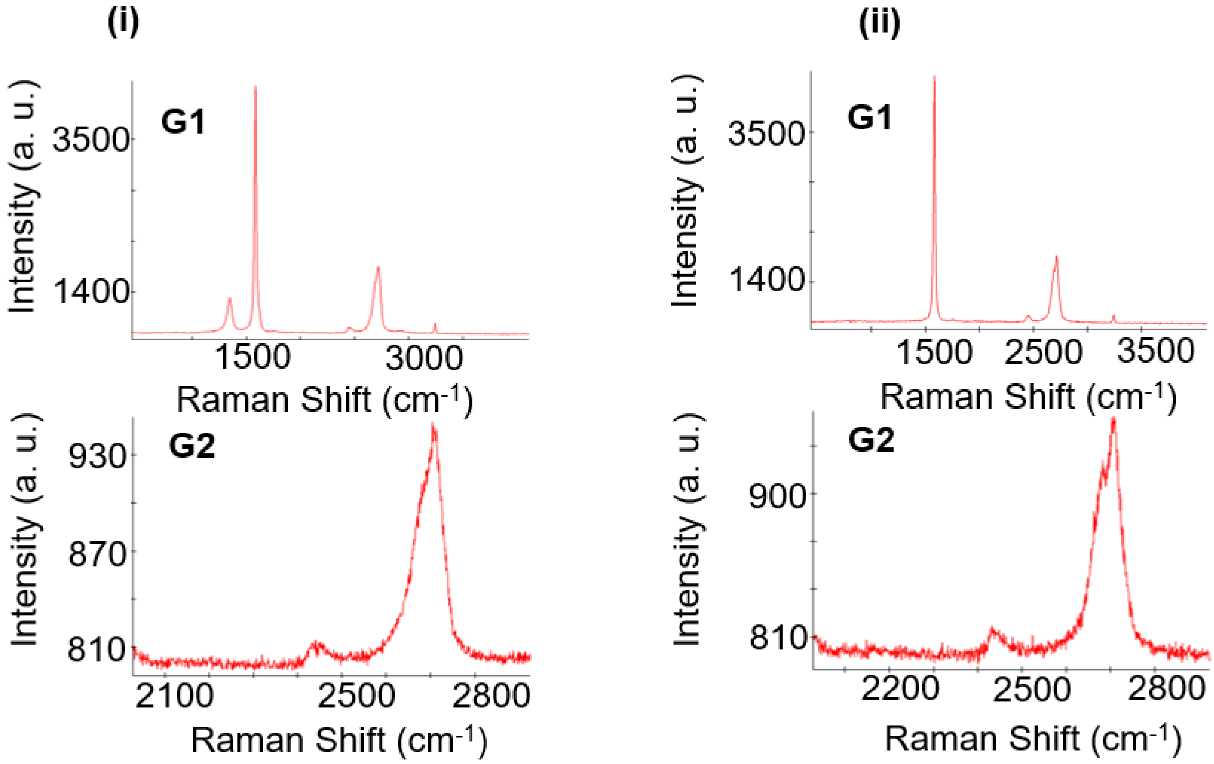

**Figure S17**. Examples of Raman spectra showing turbostratic character where, G1 denotes a 600 g/mm grating and G2 denotes a 1800 g/mm grating. The 2D peaks were recorded with the higher resolution G2 for clarity.

### ***EBSD Analysis of Graphite Films***

EBSD scans were typically performed using a 6.4 nA current and at 20 kV with the sample surface tilted by 70° and using a hexagonal sampling grid. Step sizes for the maps ranged from 0.25 – 25 µm. The standard post-processing steps included confidence index (CI) standardization (where the low CI of a point was replaced by the higher CI value of a neighboring point with the same orientation) followed by the creation of a partition that excluded points with CI < 0.1. Finally, the grain tolerance angle and minimum size were defined before the different plots and charts were generated.

As explained by Demirel et. al.,[8] EBSD scans have an inherent instrumental broadening that typically has a FWHM of ~1°, and grain tolerance angles $\geq$ 2° should be used to define mis-orientations. It was also reported by Demirel et. al. that this dispersion in orientation increases monotonically with increasing scan size (for single crystal silicon). Finally, variability in mounting and tilting of the sample that may locally change the geometry of the incident beam will cause orientation variability across the scan. This last type of topographic variation is quite common for the millimeter scale scans of the graphite films, as their surfaces are not perfectly flat. Additionally, the films sometimes have loose graphitic material deposited on the surface possibly from the torn regions of the film: it is hard to get good quality Kikuchi patterns or acceptable indexing from such areas. Thus, a grain tolerance angle of 2° and minimum size of 2 pixels have been used to define grains unless mentioned otherwise. Grain areas have been determined by multiplying the area of each hexagonal pixel by the number of pixels included in the grain. Grain diameters have been calculated as the diameter of circles occupying equivalent areas. It should be noted here that using a grain tolerance angle of 5° (ASTM protocol E2627) often produces an increase in grain size and the largest grain diameters thus obtained may be as large as ~1.4 mm (**Figure S25**). Hence, by using a tolerance angle of 2°, we have provided a somewhat conservative estimate of the grain size. In all PFs and IPFs, the points have been weighted by associated grain sizes. In all figures, the IPFs and the IPF maps are with respect to the sample normal direction. KAM maps have been plotted using the 1st nearest neighbors and an upper limit of 5º.

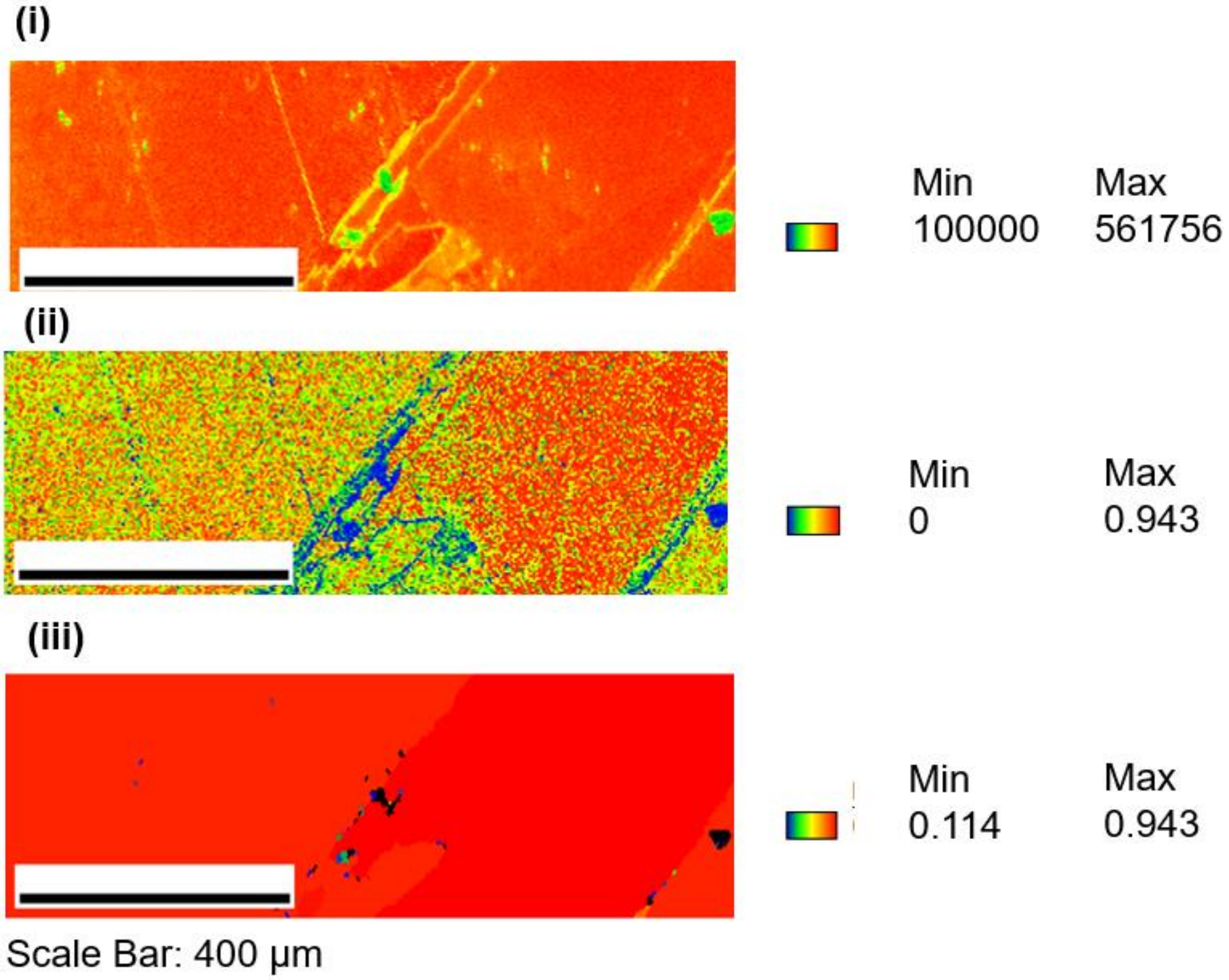

**Figure S18**. Image Quality (IQ) map from raw data (i), and, Confidence Index (CI) maps obtained from raw data (ii) and, after processing (iii) from an EBSD scan of a natural graphite flake. Black areas in (iii) have CI < 0.1.

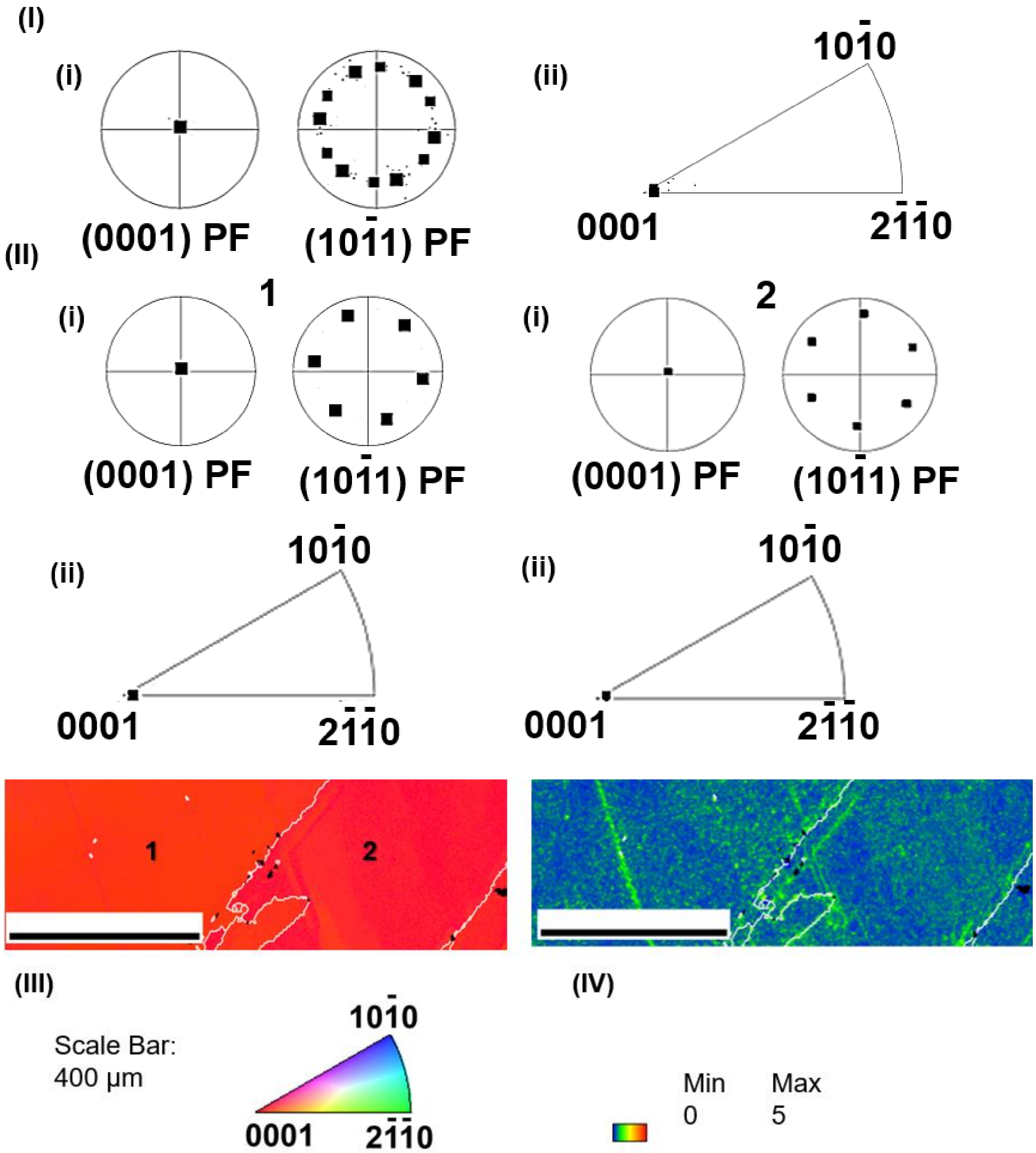

**Figure S19**. Large area EBSD scan of a natural graphite flake: (I) (i) (0001) and $(10\bar{1}1)$ PFs, and, (ii) IPF from the entire scan; (II) (i) (0001) and $(10\bar{1}1)$ PFs, and, (ii) IPFs from regions 1 and 2; (III) IPF map for entire scan; (IV) KAM map for entire scan. Black areas represent pixels with CI < 0.1 that have not been included and grain boundaries are represented in white in the IPF and KAM maps. The points in the PFs and IPFs have been weighted by grain size. For this scan, ISR = 99.6% and the step size used = 4 µm. All IPFs and IPF maps are of the sample normal direction (001).

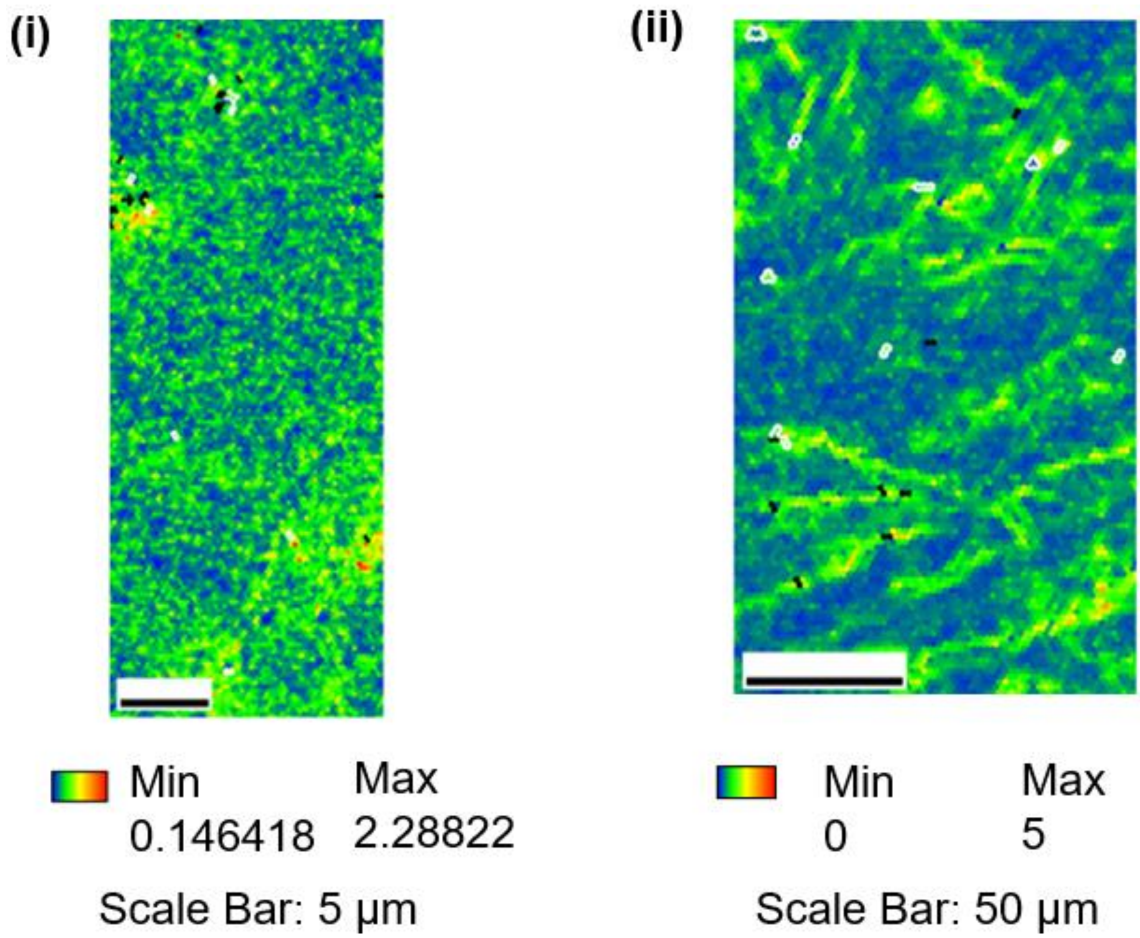

**Figure S20**. KAM maps for the ‘smaller’ EBSD scans in (I) Figure 3-I, and, (II) Figure 3-II. Black areas represent pixels with CI < 0.1 that have not been included and grain boundaries are represented in white.

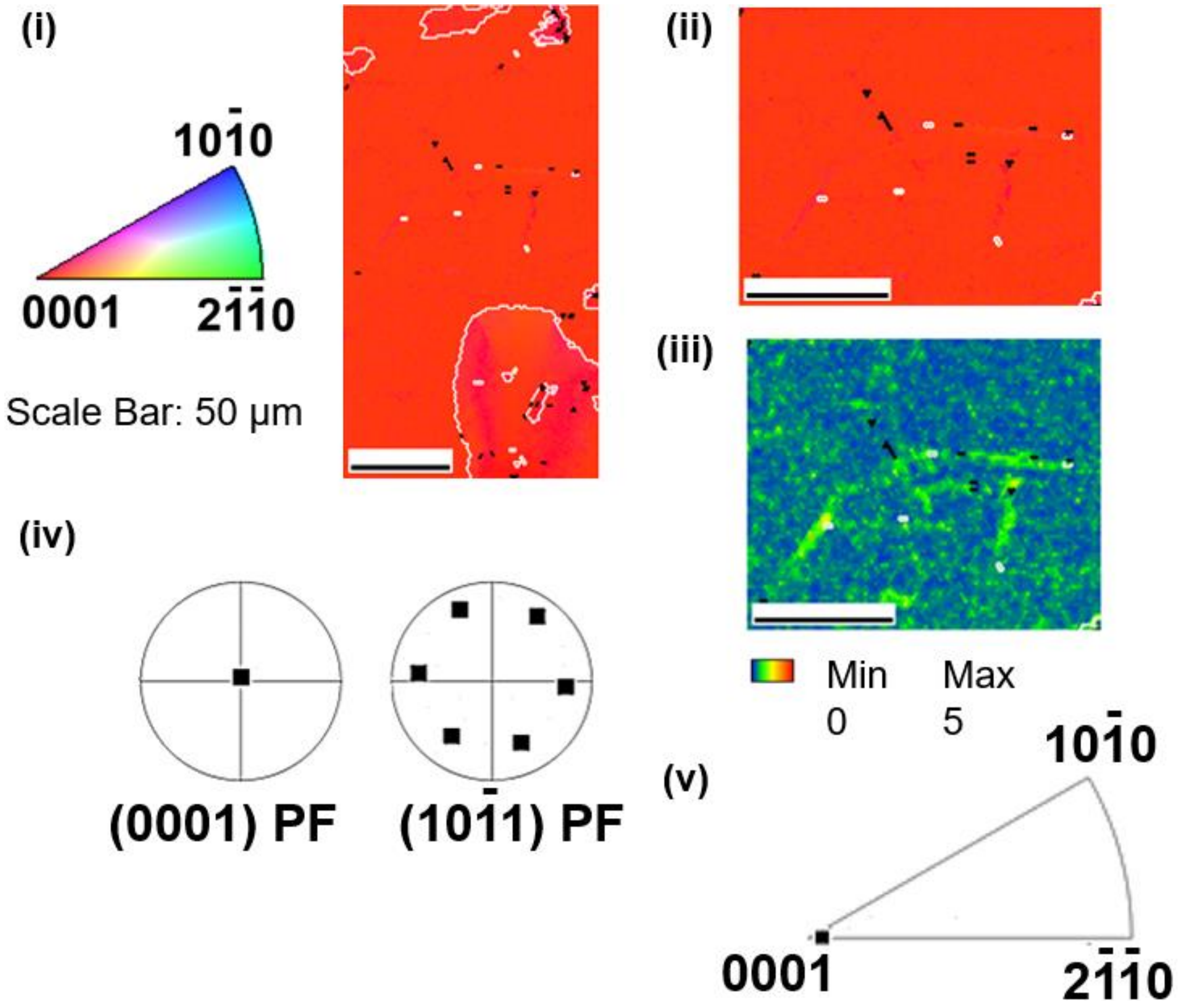

**Figure S21.** (i) IPF map of a ~0.13x0.2 mm$^2$ scan; (ii) IPF map, (iii) KAM map, (iv) (0001) and (10$\bar{1}$1) PFs, and, (v) IPF of a cropped ‘single-crystal’ area 1. Black areas represent pixels with CI < 0.1 that have not been included and grain boundaries are represented in white in the IPF and KAM maps. The points in the PFs and IPFs have been weighted by grain size. All IPFs and IPF maps are of the sample normal direction (001).

**Table S4**: Details of ‘small’ EBSD scans

| **Sample Details** | **Step size (µm)** | **ISR (%)** | **Largest grain size** | |
|---|---|---|---|---|
| | | | Diameter (µm) | Area (µm$^2$) |
| Fig. 3-I | 0.25 | 99.7 | 28 | 619 |
| Fig. 3-II | 2 | 99.8 | 189 | 28672 |
| Fig. S21 | 1.5 | 99.4 | 174 | 24332 |

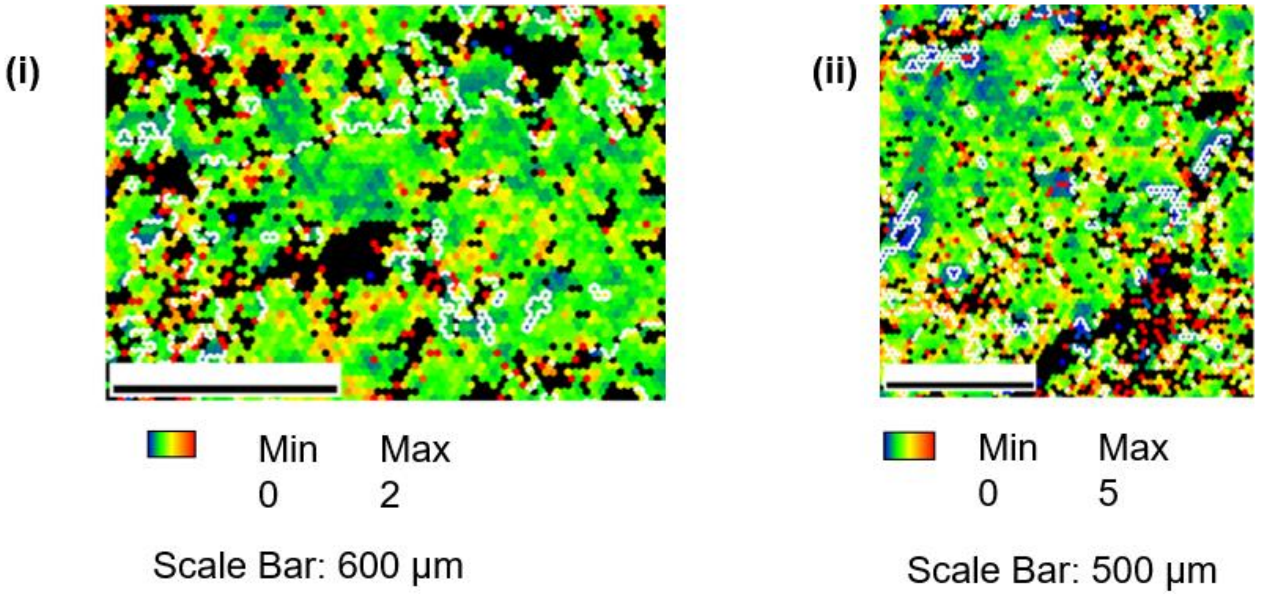

**Figure S22**. KAM maps for the ‘larger’ EBSD scans in (i) Figure 4-I, and, (ii) Figure 4-II. . Black areas represent pixels with CI < 0.1 that have not been included and grain boundaries are represented in white.

**Table S5**: Details of large EBSD scans

| **Sample Details** | **Step size (µm)** | **ISR (%)** | **Largest grain size** | |
|---|---|---|---|---|
| | | | Diameter (µm) | Area (mm$^2$) |
| Type B (Fig. 4-I) | 20 | 80 | 904 | 0.62 |
| Type B (Fig. 4-II) | 20 | 80 | 877 | 0.62 |
| Type A (Fig. S23) | 10 | 73 | 826 | 0.56 |

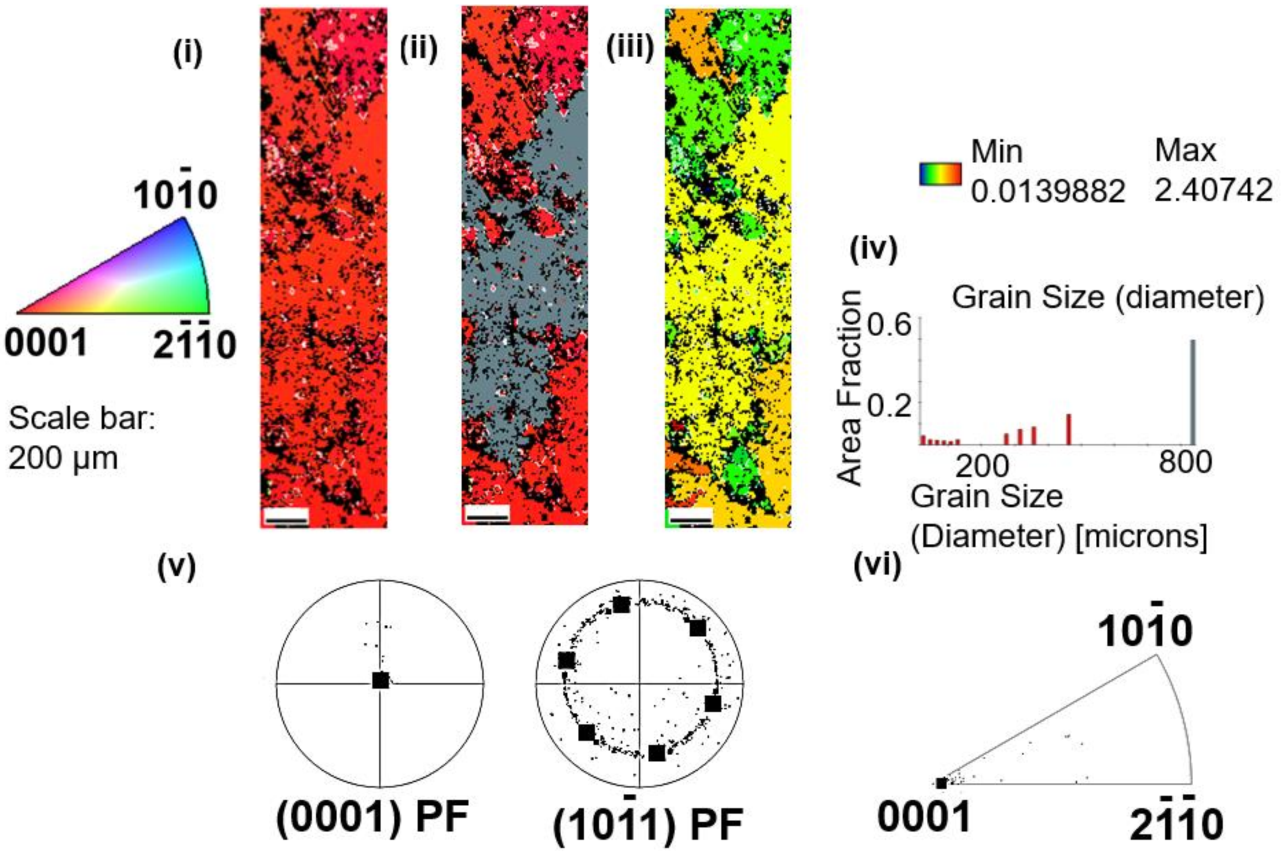

**Figure S23**. EBSD scan of a Type A graphite film: (i) IPF map, (ii) IPF map with the largest grain highlighted in gray, (iii) KAM map, (iv) Grain size chart, (v) (0001) and (10$\bar{1}$1) PFs, and, (vi) IPF. Grain boundaries are represented in white, black areas represent pixels with CI < 0.1 that have not been included and yellow regions are from the bare silicon wafer in the IPF and KAM maps. The points in the PFs and IPFs have been weighted by grain size. All IPFs and IPF maps are of the sample normal direction (001).

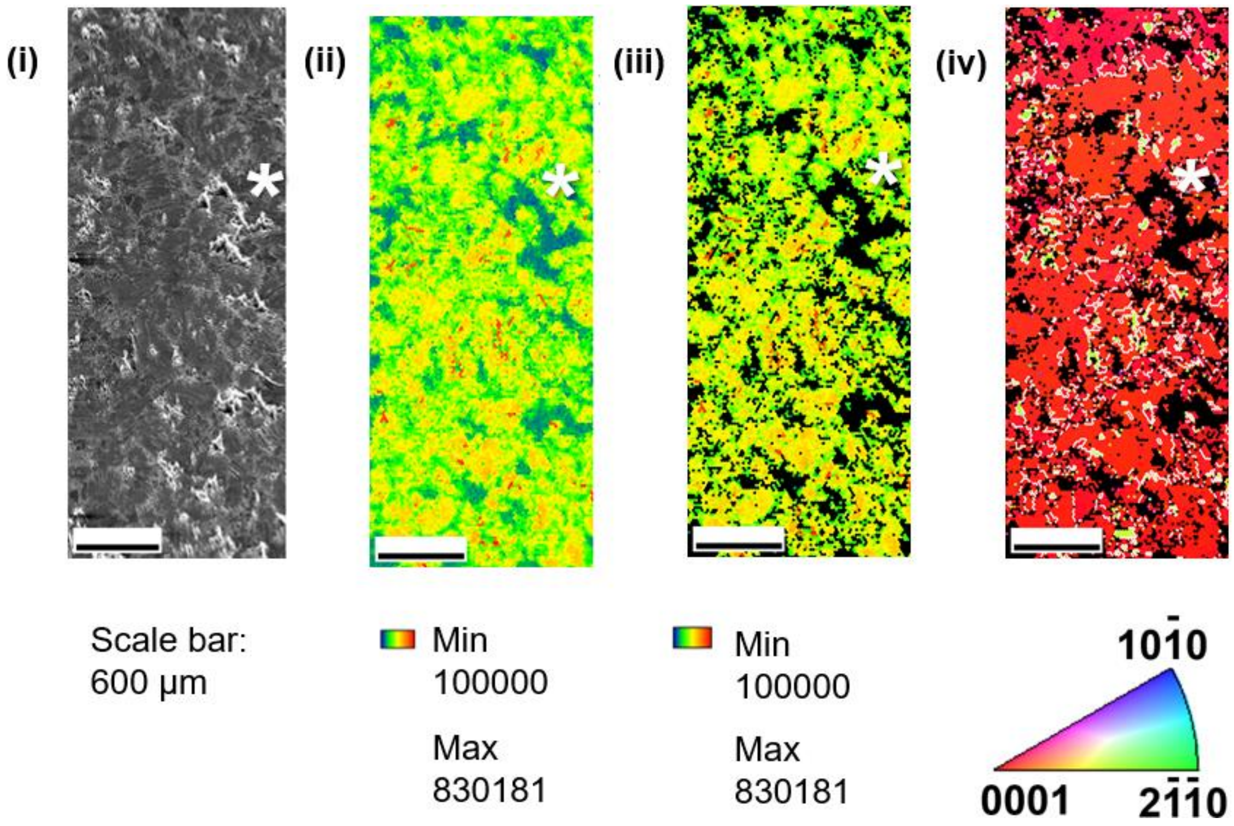

**Figure S24**. (i) SEM image, (ii) Raw IQ map, (iii) – (iv) IQ map and IPF map obtained from post-processing. Black areas represent pixels with CI < 0.1 that have not been included in (III)-(IV) and grain boundaries are represented in white in (IV). All IPFs and IPF maps are of the sample normal direction (001).

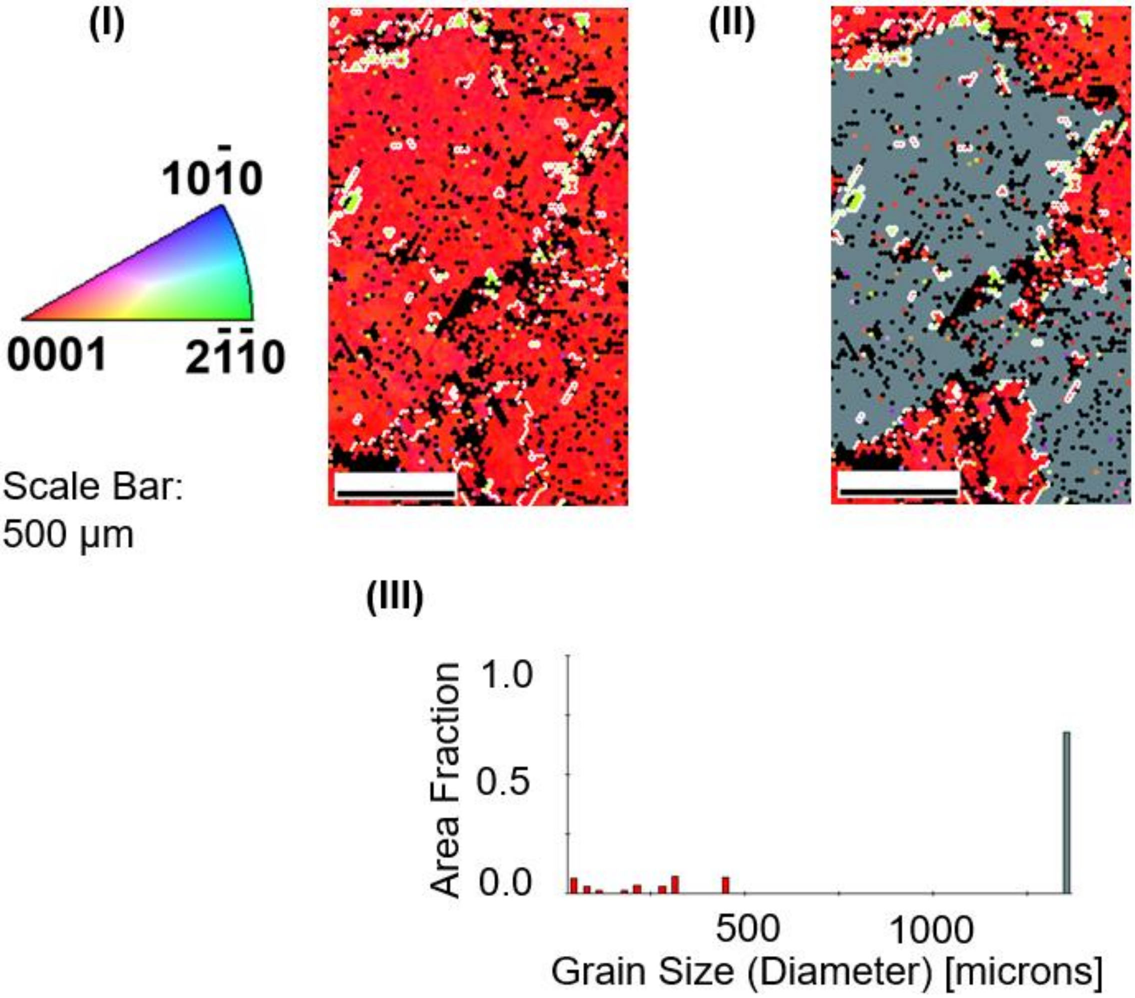

**Figure S25**. Grain size estimation with a tolerance angle of 5º for the EBSD scan of a Type B film in **Figure 4-B**: (I) IPF map, (II) IPF map with the largest grain highlighted in gray, (III) grain size chart. Black areas represent pixels with CI < 0.1 that have not been included, yellow regions are from the bare silicon wafer and grain boundaries are represented in white in the IPF maps. All IPFs and IPF maps are of the sample normal direction (001).

(I)

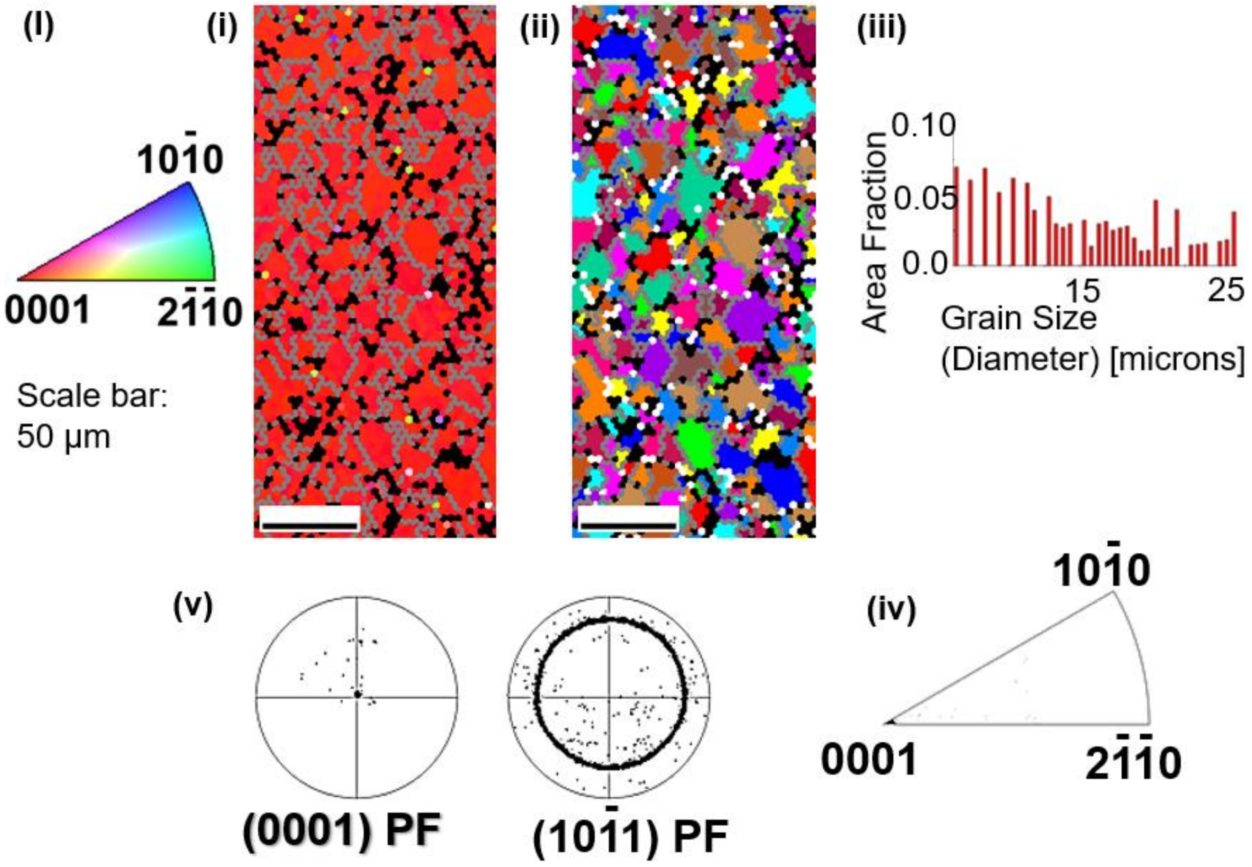
(i)
(ii)
(iii)
10$\bar{1}$0
0001
2$\bar{1}\bar{1}$0
Scale bar:
50 µm
Area Fraction
0.10
0.05
0.0
15
25
Grain Size
(Diameter) [microns]
(v)
(0001) PF
(10$\bar{1}$1) PF
(iv)
10$\bar{1}$0
0001
2$\bar{1}\bar{1}$0

(II)

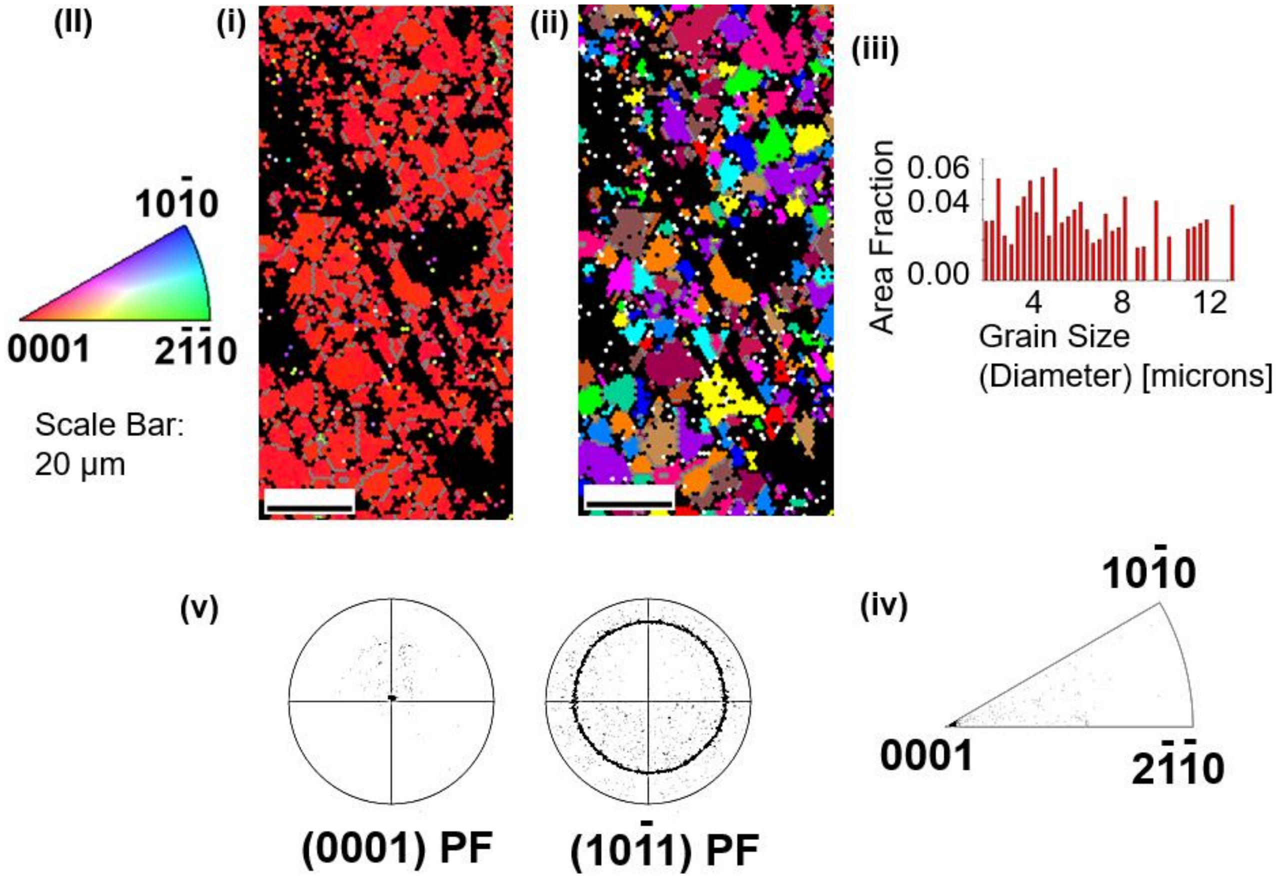
(i)
(ii)
(iii)
10$\bar{1}$0
0001
2$\bar{1}\bar{1}$0
Scale Bar:
20 µm
Area Fraction
0.06
0.04
0.00
4
8
12
Grain Size
(Diameter) [microns]
(v)
(0001) PF
(10$\bar{1}$1) PF
(iv)
10$\bar{1}$0
0001
2$\bar{1}\bar{1}$0

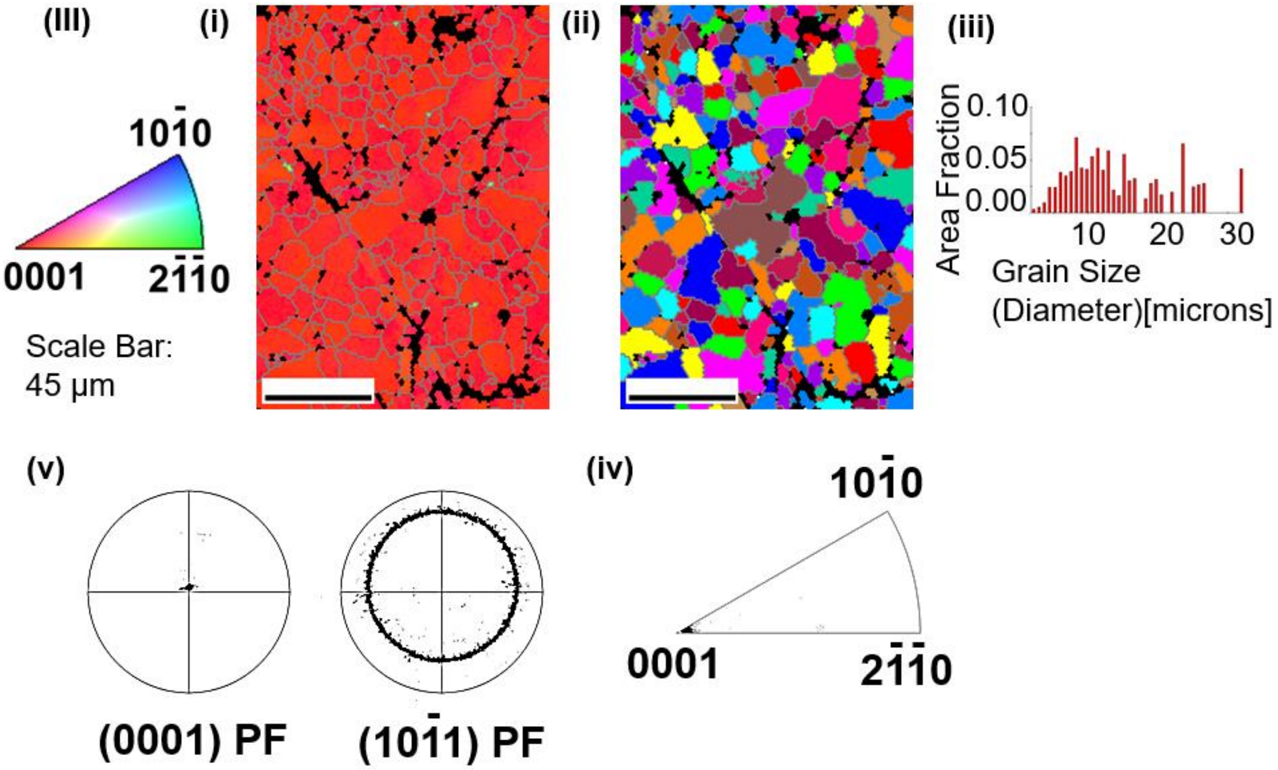

**Figure S26**. EBSD scans of (I) HOPG-A (Optigraph), (II) HOPG B (Optigraph) and (III) HOPG B (XFNano): (i) IPF map, (ii) unique grain color map, (iii) grain size chart, (iv) IPF and, (v) (0001) and $(10\bar{1}1)$ PFs. Black areas represent pixels with CI < 0.1 that have not been included, grain boundaries are represented in gray and yellow regions are from the bare silicon wafer in the IPF maps. The points in the PFs and IPFs have been weighted by grain size. All IPFs and IPF maps are of the sample normal direction (001).

**Table S6**: Details of EBSD scans of HOPG

| **Sample Details** | **Step size (µm)** | **ISR (%)** | **Largest grain size** | |
|---|---|---|---|---|
| | | | Diameter (µm) | Area (µm$^2$) |
| HOPG A (Optigraph) | 4 | 83 | 26 | 1066 |
| HOPG B (Optigraph) | 1 | 55 | 13 | 140 |
| HOPG B (XFNano) | 1.2 | 92 | 32 | 820 |

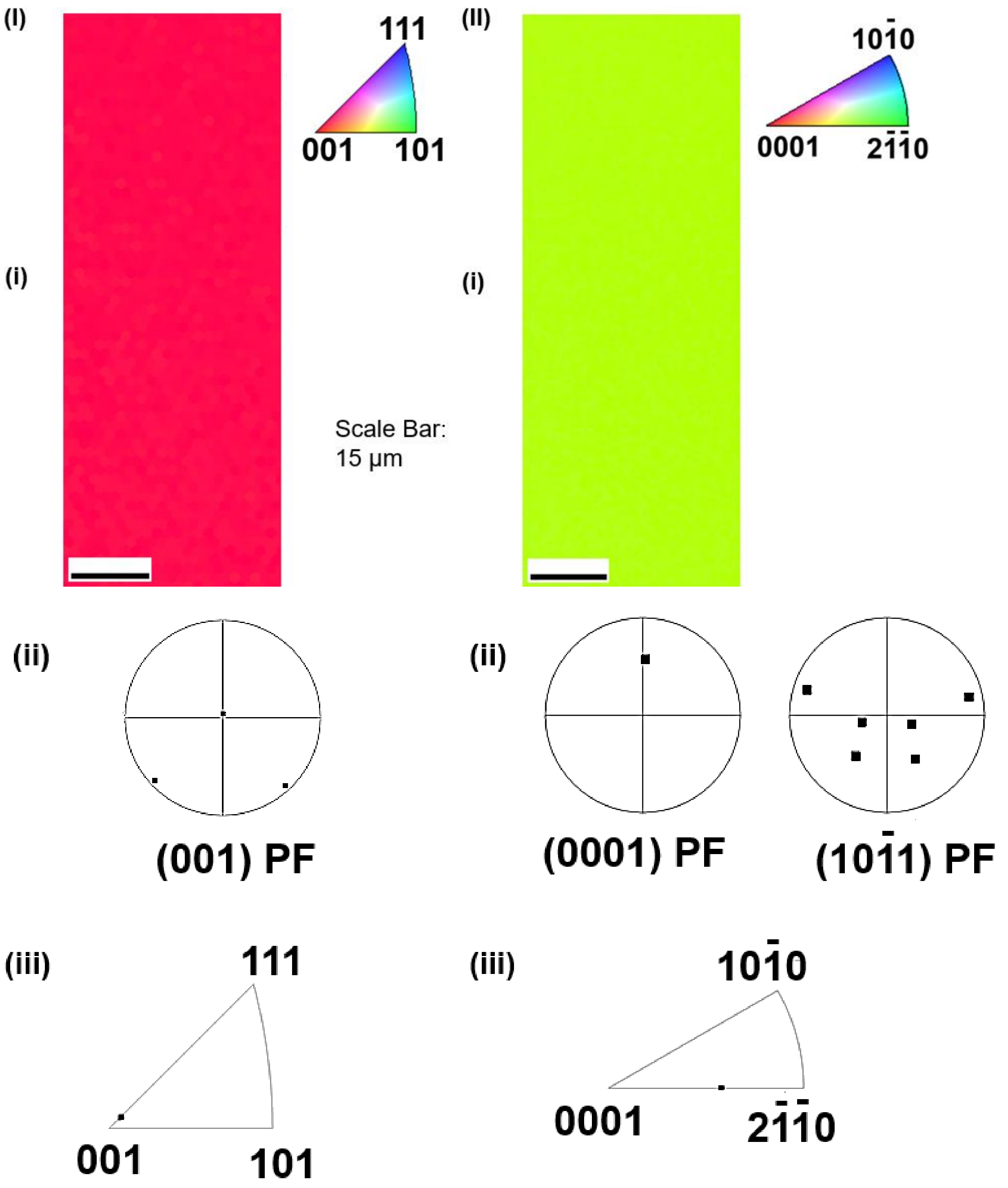

**Figure S27**. EBSD scan of a silicon wafer with the input phase as (I) Silicon: (i) IPF map, (ii) (001) PF, and, (iii) IPF; (II) Graphite: (i) IPF map, (ii) (0001) and (10$\bar{1}$1) PFs, and, (iii) IPF. Grain boundaries are in white. All IPFs and IPF maps are of the sample normal direction (001).

## ***XRD Characterization of Graphite Films***

**Table S7-(i)**: Lattice spacing for $d_{002}$ from XRD with Cu-Kα radiation and a 0-D detector.

| Sample Details | 2θ (°) | FWHM (°) | FWHM (°)-corrected | $d_{0002}$ (Å) |
|---|---|---|---|---|
| Grade A HOPG (Optigraph) | 26.522 | 0.168 | 0.103 | 3.358 |
| Grade B HOPG (Optigraph) | 26.455 | 0.218 | 0.173 | 3.667 |
| Grade A HOPG (SPI) | 26.482 | 0.223 | 0.180 | 3.363 |
| Grade B HOPG (XFNANO) | 26.557 | 0.192 | 0.138 | 3.353 |
| Sample A (inner)-8-8-18-E (type B) | 26.568 | 0.201 | 0.151 | 3.352 |
| Sample B (outer)-4-2-19-C (type B) | 26.551 | 0.200 | 0.149 | 3.354 |
| 8-2-18-US-A (type B) | 26.560 | 0.163 | 0.094 | 3.352 |
| 8-2-18-DS-B (type B) | 26.561 | 0.203 | 0.153 | 3.353 |
| 4-4-19-A (type B) | 26.554 | 0.173 | 0.111 | 3.354 |
| 3-27-19-D (type B) | 26.561 | 0.200 | 0.149 | 3.353 |
| 4-4-19-F (type B) | 26.571 | 0.188 | 0.133 | 3.352 |
| Sample 1 (wrinkled)-(type A) | 26.571 | 0.188 | 0.133 | 3.352 |

A FWHM of 0.133° was obtained for 2θ = 41.780° for Sapphire-0001 and was used to correct for instrumental broadening. Generally, for HOPG like materials the crystal sizes are too large (> 1 µm) to be determined by the Scherrer equation.[9-11]

Mosaic spread may be determined by varying or 'rocking' the incident beam relative to the Bragg angle of interest.

**Table S7-(ii)**: Mosaic spreads from Rocking Curve Experiments around the (004) peak at 2θ = 54.66°

| Sample Details | θ (°) | Mosaic Spread (°) |
|---|---|---|
| Grade A HOPG (Optigraph)[1] | 27.369 | 0.533 |
| Grade B HOPG (Optigraph)[1] | 27.340 | 0.963 |
| Grade A HOPG (XFNANO)[1] | 27.292 | 0.775 |
| Grade B HOPG (XFNANO)[2] | 26.697 | 0.887 |
| Sample A-8-8-18-E (type B) | 27.332 | 0.210 |
| 8-2-18-DS-B (type B) | 27.327 | 0.238 |
| 8-2-18-US-A (type B) | 27.309 | 0.093 |
| 4-4-19-F (type B) | 27.297 | 0.115 |
| Sample 1 (wrinkled)[3]- (type A) | 27.279 | 0.551 |
| Sample 1 (wrinkled)[3]-pressed-(type A) | 27.305 | 0.377 |

[1]Sample thickness ~1000 µm; [2]Sample thickness ~ 1–2 µm; [3]Sample thickness ~250 nm. All other sample thicknesses ~ 800 nm.

The mosaic spreads have not been corrected for instrumental broadening. However, on running the same measurement for single crystal c-sapphire, the 20.61° theta peak gave a value of 0.0481°, indicating that an inherent instrumental broadening is present. Thickness variations and curvature (i.e. the fact that the films are not perfectly flat on the silicon wafer) are also expected to contribute to the mosaic spread.[12]

### *$H_2$ pre-treatment of Ni*

The first part of all Type A and Type B processes included a $H_2$ pre-treatment step (step 1, **Figure 1**). In addition to cleaning the Ni surface from surface oxides, considerable grain growth was observed, with larger average grain sizes with increasing temperature.

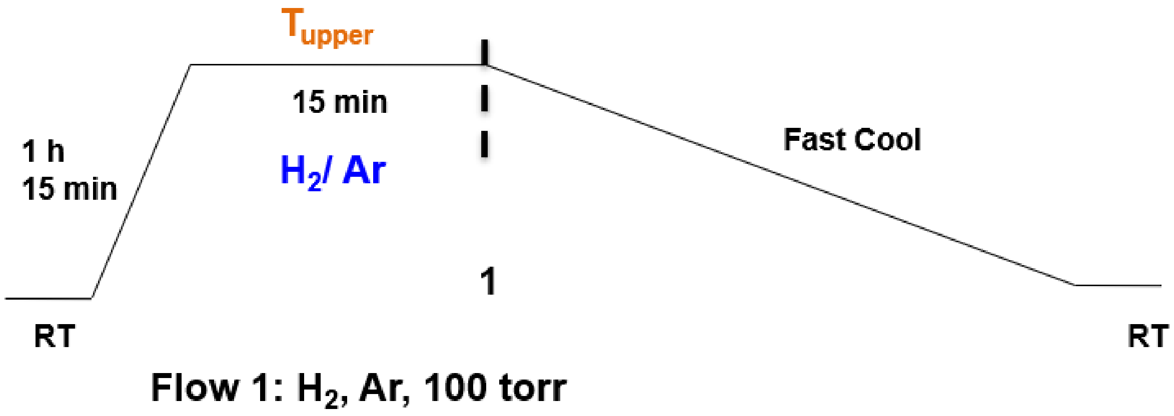

**Figure S28**. Schematic of the $H_2$ pre-treatment step reproduced to determine Ni grain size.

**Table S8**. Ni grain sizes after $H_2$ pre-treatment at 1150 °C

| Conditions | Largest grain diameter (μm) | Average grain diameter (μm) |
|---|---|---|
| As received Ni-100 | 8 | 2 |
| Ni-100 | 846 | 470 |
| Ni-25 | 130 | 61 |

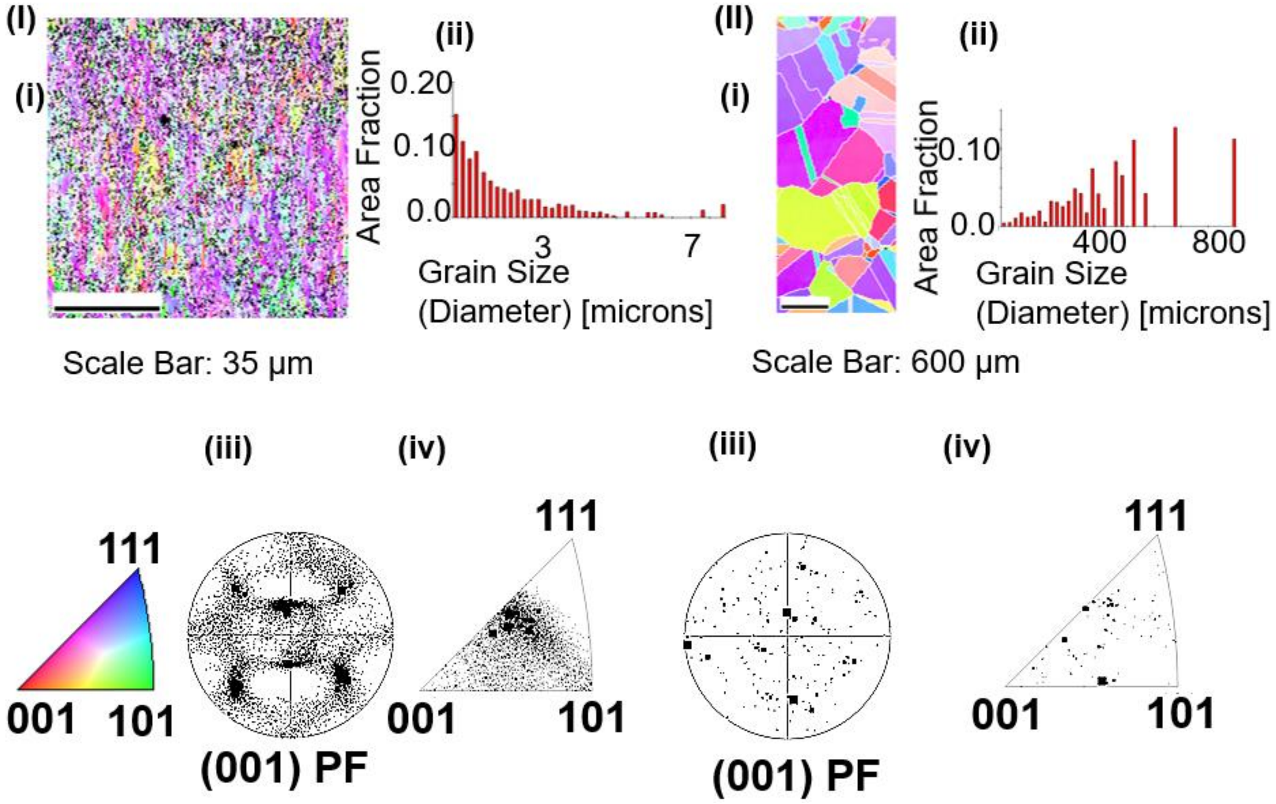

**Figure S29**. EBSD of Ni: (I) As-received Ni, (II) after $H_2$ pre-treatment at 1150 ºC; (i) IPF map, (ii) grain size chart, (iii) (001) PF, and, (iv) IPF. Black areas represent pixels with CI < 0.1 that have not been included and grain boundaries are represented in white in the IPF maps. All IPFs and IPF maps are of the sample normal direction (001).

### ***Graphite Films from 25 µm thick Ni foils***

Graphite films with smaller grains were obtained under the same process conditions (Process B) with the largest grain sizes ~0.24 mm.

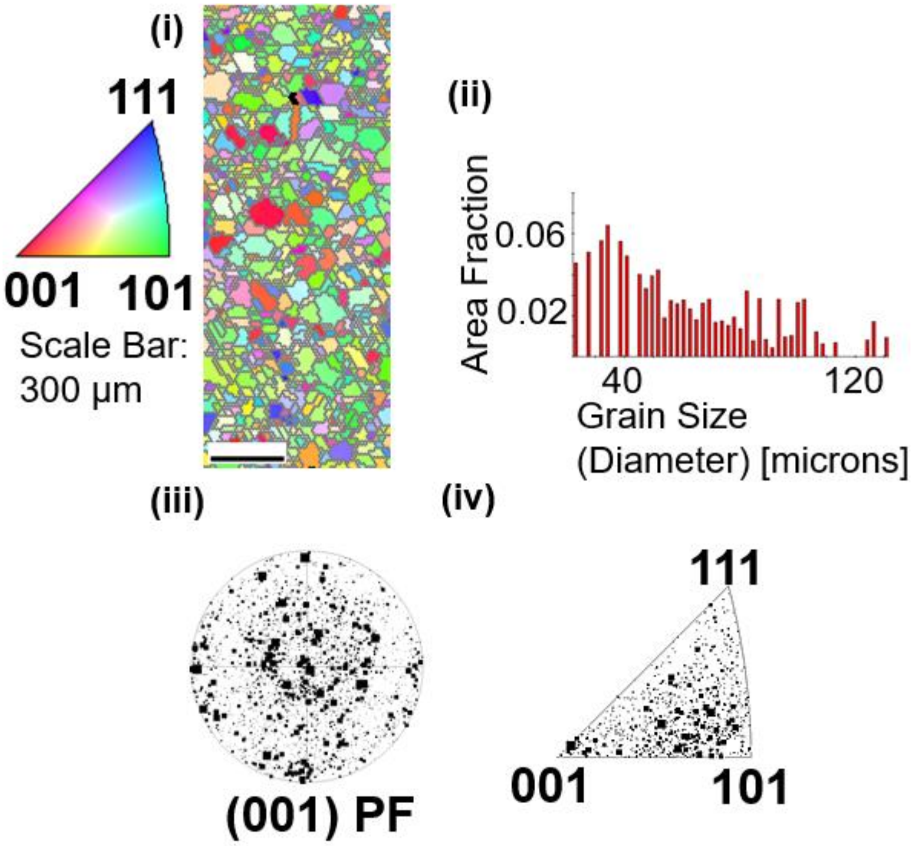

**Figure S30**. Ni after $H_2$ pre-treatment at 1150 ºC: 25 µm Ni (i) IPF map, (ii) grain size chart, (iii) (001) PF, and, (iv) IPF. Black areas represent pixels with CI < 0.1 that have not been included and grain boundaries are represented in gray in the IPF maps. All IPFs and IPF maps are of the sample normal direction (001).

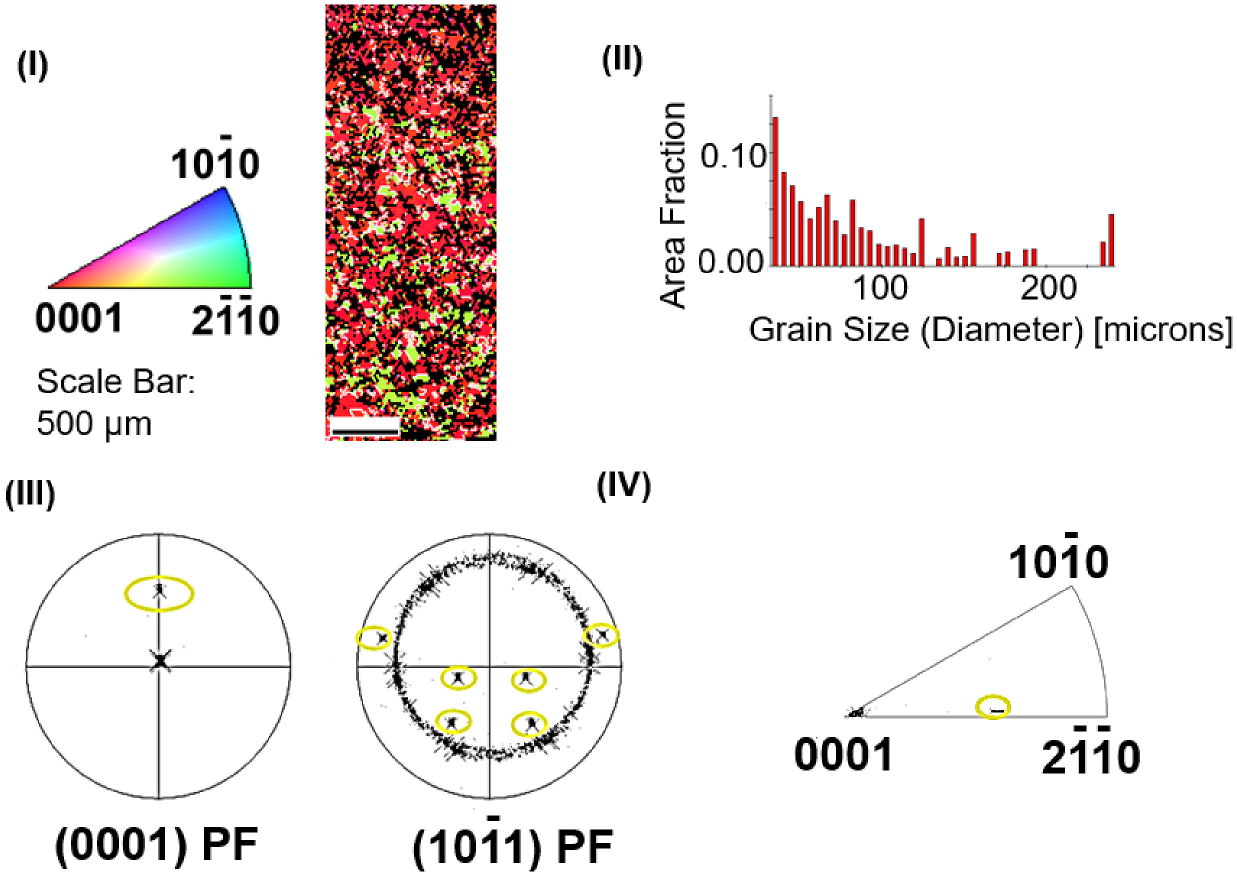

**Figure S31**. EBSD scan of a Type B 'collapsed' graphite film synthesized on a 25 µm Ni foil. (I) IPF map (scale bar: 500 µm), (II) Grain size chart, (III) (0001) and (10$\bar{1}$1) PFs, and, (IV) IPF. Grain boundaries are shown in white, black areas represent pixels with CI < 0.1 that have not been included and yellow regions are from the bare silicon wafer in the IPF maps. The points circled in yellow on the IPFs and PFs are from the bare silicon wafer. The points in the PFs and IPFs have been weighted by grain size. All IPFs and IPF maps are of the sample normal direction (001).

**Table S9**: Details of EBSD scans from graphite films synthesized on 25 µm Ni foils

| **Sample Details** | **Step size (µm)** | **ISR (%)** | **Largest grain size** | |
|---|---|---|---|---|
| | | | Diameter (µm) | Area (µm$^2$) |
| Graphite (Ni-25 µm)<br>Fig. S31 | 25 | 63 | 240 | 90538 |

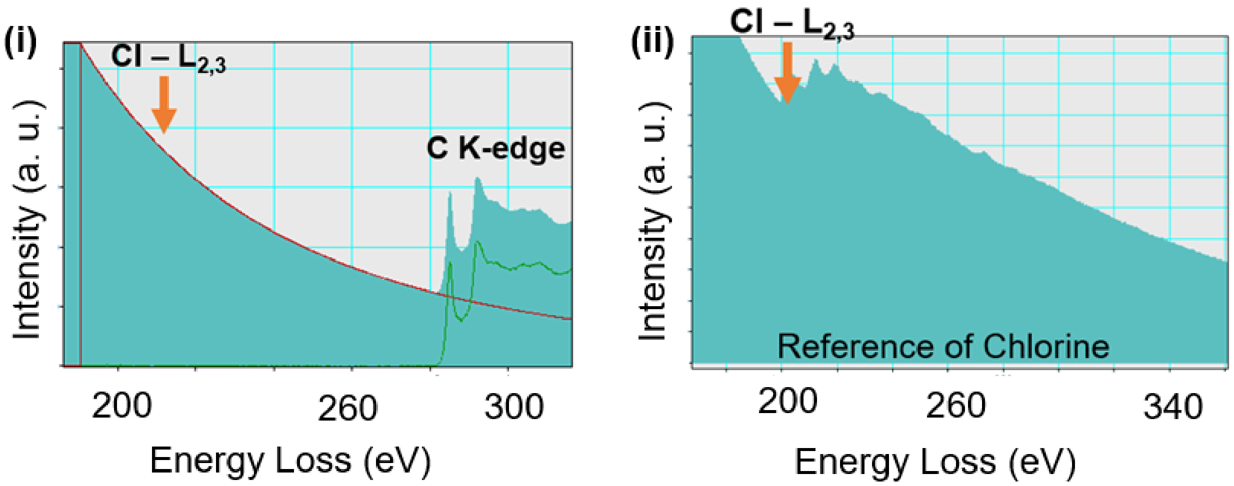

**Figure S32.** Typical EELS spectrum showing the absence of chlorine and the presence of $sp^2$ hybridized C, from the cross-section of a Type B graphite film.

### *Mechanical property calculations*

**Effect of wrinkles**: The increase in in-plane stiffness may be estimated using reference [13] for a film of thickness T from which wrinkles, having an amplitude A that is small compared to their mean separation distance and occupying an area fraction f, have been removed. We have accordingly found that $E_{(f=0)}/E_{(f)}=1+k*f*(A/T)^2$, where k=6 is a theoretical value and $E_{(f=0)}$ and $E_{(f)}$ represent the Young's modulus of the wrinkle-free and wrinkled films respectively.[13] Thus, for example, removing a 0.1 (=f) area fraction of wrinkles for films that have (A/T) ranging from 1–10 would increase the Young's modulus by a factor of 0.6–60. Removal of wrinkles is not expected to significantly influence the strength.

**Effect of grain size on film strength**: In general, the tensile strength s of the film is determined from the size m (in terms of atomic size) of its largest defects as $s(m) = s(m=0)*(1+m)^{-n}$, with $0<n<1$. An intermediate value of n=1/2 is theoretically predicted for this equation from quantized fracture mechanics[14,15] (whereas other values could describe nonlinear constitutive laws, re-entrant corner defects, or the weakest link theory).

Hall-Petch like behavior: Considering the defect size m=c1*d, and thus proportional via a constant c1 to the grain size d, would result in the well-known Hall-Petch law, i.e. $s(d)=s(d=0)*(1+c1*d)^{-n}$ with n=1/2. Again, the constant c1 is the inverse of a characteristic length. Thus, s(d) is nearly proportional to $d^{-n}$. The direct Hall-Petch-like law has been observed in silico via molecular dynamics (MD) simulations for polycrystalline graphene by Song et. al.,[16] with s(d=0)=62 GPa suggesting that smaller grain size is beneficial for the strength up to this last value, that could thus be interpreted as the strength of amorphous graphene. However, the full removal of grain boundaries and the recovering of the crystalline nature of graphene could further increase the strength to the graphene ideal strength of about 100GPa (for example, 98GPa or 115GPa are the values reported along the armchair and zigzag directions respectively[16]).

Inverse Hall-Petch like behavior: Another intepretation is to consider the defect size as proportional to the number of grain boundary (GB) junctions, which geometrically is proportional to $d^{-2}$, so that s(d)=s(d=∞)*(1+c2/$d^{2}$)$^{-n}$ where c2 is a constant. Thus, s(d) is nearly proportional to $d^{2n}$, representing an inverse Hall-Petch law. The inverse Hall-Petch law has been observed in silico by MD simulations for polycrystalline graphene by Sha et. al.,[17] with s(d)=31GPa/nm^0.1*d^0.1, verifying also that the scaling of the number or density of GB junctions is proportional to $d^{-2}$.

Using this last strength scaling equation, we can quantify the strengthening due to the removal of GBs, assuming that they are the weakest links observed experimentally.[17] Thus, the strength increase in a graphite film of size L that results from an increase in grain size from a size d to a single crystal of size L may be roughly estimated as: s(d=L)/s(d)=(L/d)^0.1. For example, the strength increases by a factor of ~2 if L/d changes from 10000–10.

**Effect of grain size on film stiffness**. The same power law type of scaling has been observed by both Song et. al. and Sha et. al. [16, 17] for Young's modulus, suggesting film stiffenning by GB removal. Accordingly, the potential applications for both wrinkle-free and grain boundary-free graphite films are where "high modulus and high strength carbon films" are required.

## *Quality comparison of graphite formed in Steps 3 and 4 in Process B*

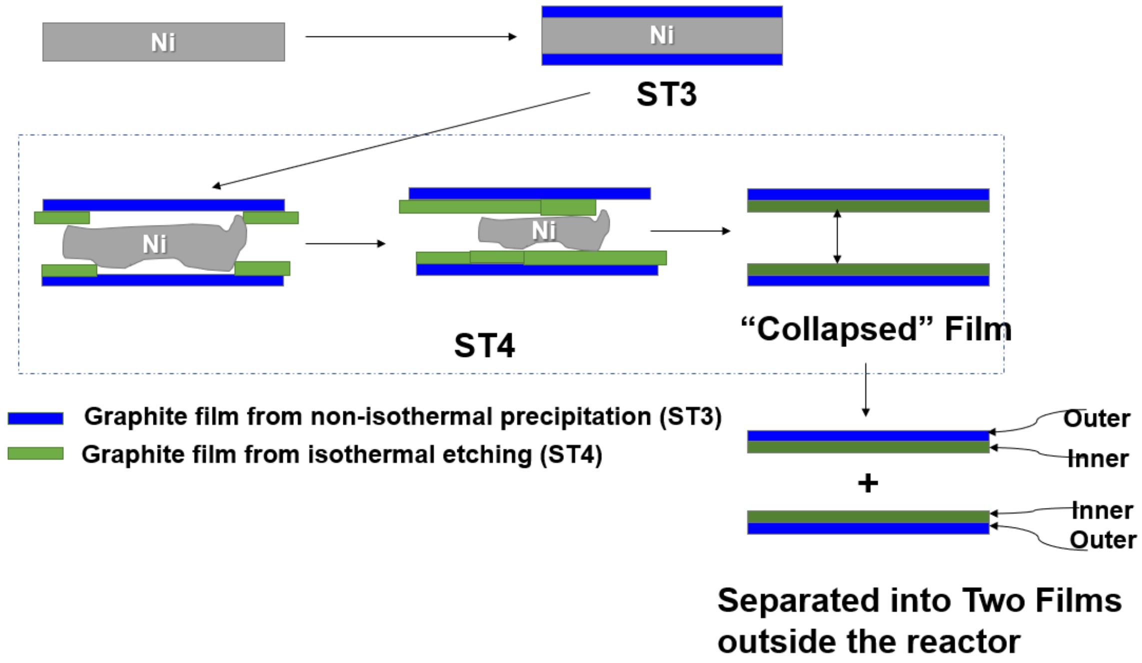

**Figure S33**. Schematic depicting a possible route for the formation of Type B graphite film in steps 3 and 4 (as described in **Figure 1**).

The schematic above takes the following observations into account: (1) the etching started from the edges of the Ni foils and proceeded inward such as in **Figure S8-(ii)**, and (2) a Ni foil with an area ~1 cm$^2$ formed 2 graphite films (on its top and bottom surfaces) with ~1 cm$^2$ lateral areas. The surface of the graphite film that was originally in contact with the Ni foil substrate has been referred to as the 'inner' surface and the opposite surface as the 'outer' surface. Thus, as per the above schematic, regions closer to the outer surface were formed during step 3, while regions closer to the inner surface were formed during step 4. Samples have been transferred to silicon wafers such that either the inner or the outer surface was exposed and thus, the surface studied. No obvious differences have been observed between the outer and the inner surfaces (from similarly synthesized different films) in terms of graphite quality, using multiple characterization techniques. Examples include:

1. EBSD scans: **Figures 4-I** and **4-II** are, respectively, from the inner and outer surfaces of two different graphite films.

2. Raman maps:

   **Table S3-(i)**: Samples 1-2: inner surface; Samples 3-4: outer surface

   **Table S3-(ii)**: Samples B-C: inner surface

3. XRD: As explained in the main text, the entire thickness of the film is interrogated by XRD.

   **Table S7-(i)**: Sample A:inner surface, Sample B:outer surface

   **Table S7-(ii)**: Sample A-8-8-18-E: inner surface, 8-2-18-US-A: outer surface

**HR-TEM and EELS Analysis**: HR-TEM and EELS have been used to study and explore graphitization in cross-section TEM samples. No obvious differences were observed in terms of graphite quality between the top and middle regions (**Figure S34**) from HR-TEM imaging.

**Figure S35** shows EELS spectra collected at ~20 nm intervals from a cross-section sample. For the C-K edge, the maximum $\pi^*/\sigma^*$ intensity was observed close to the 'inner' surface of the film, implying that the highest quality graphite might be contained in this region. In any case, we note that the variation is relatively small, and the sample is "well graphitized" throughout the entire cross section. (Please note that variations in quality in cross-section TEM samples may also arise from exposure to ion or electron beams during sample preparation or imaging).

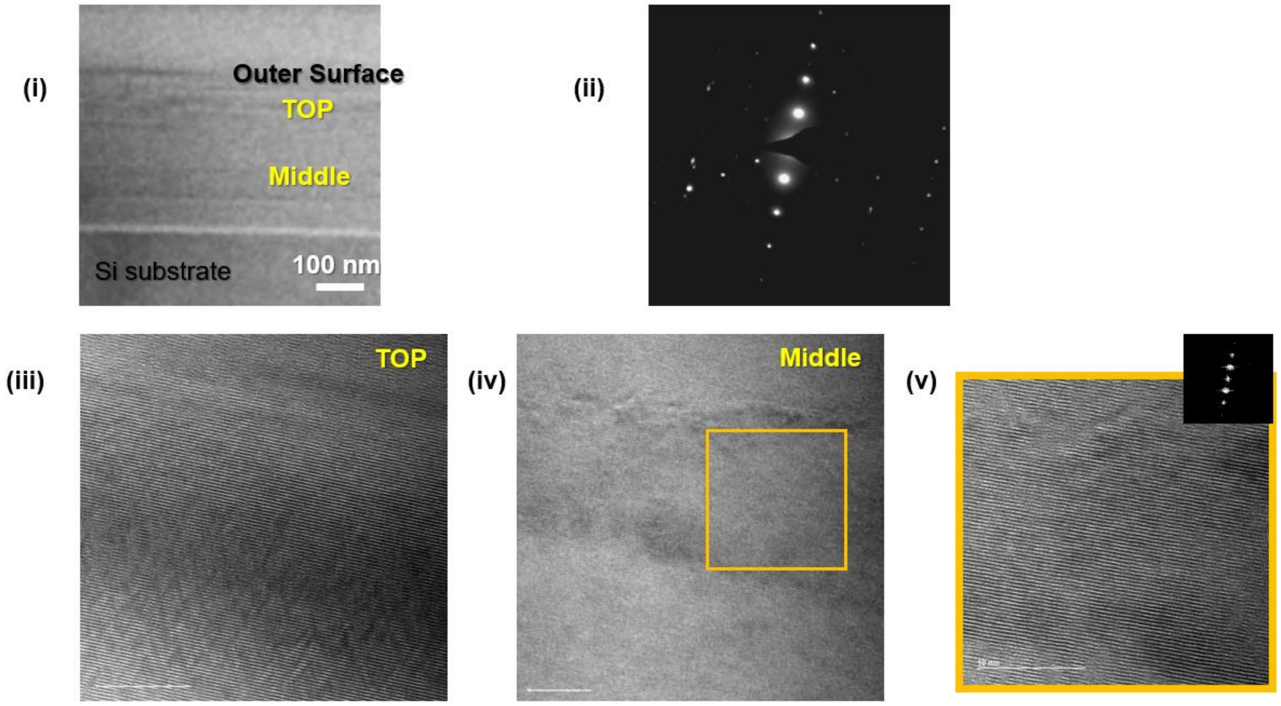

**Figure S34**. HR-TEM images of a cross-section sample: (i) image, and (ii) electron diffraction pattern; images from (iii) top region, and, (iv) middle region; (v) is a higher magnification image of the middle region with its digital diffractogram pattern shown in the inset. Scale bars for (iii)-(v): 10 nm.

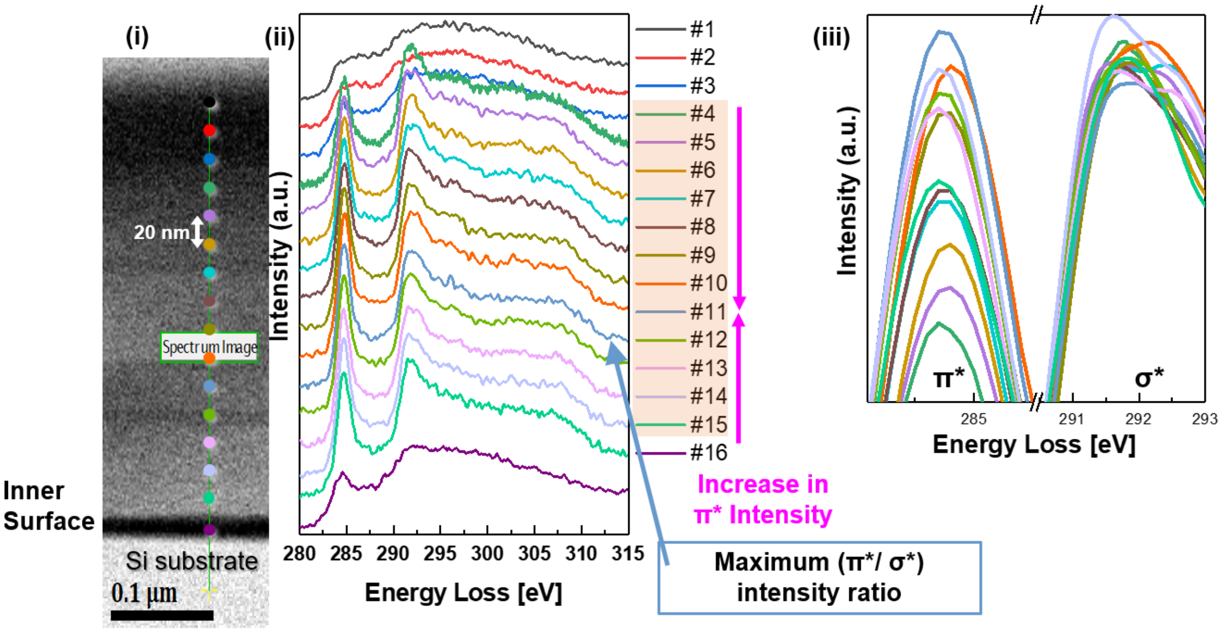

**Figure S35**. (i) Image of a cross-section sample; (ii)-(iii): corresponding EELS spectra.

**Oxygen Plasma Etching**: Oxygen plasma etching has been used to etch and compare samples through EBSD. Two plasma strengths were used, ST1 resulted in the etching of about 80 to 100 nm, while ST2 resulted in the etching of about 40 to 50 nm. As the upper graphene layers are etched away, similar layers lying underneath are revealed.

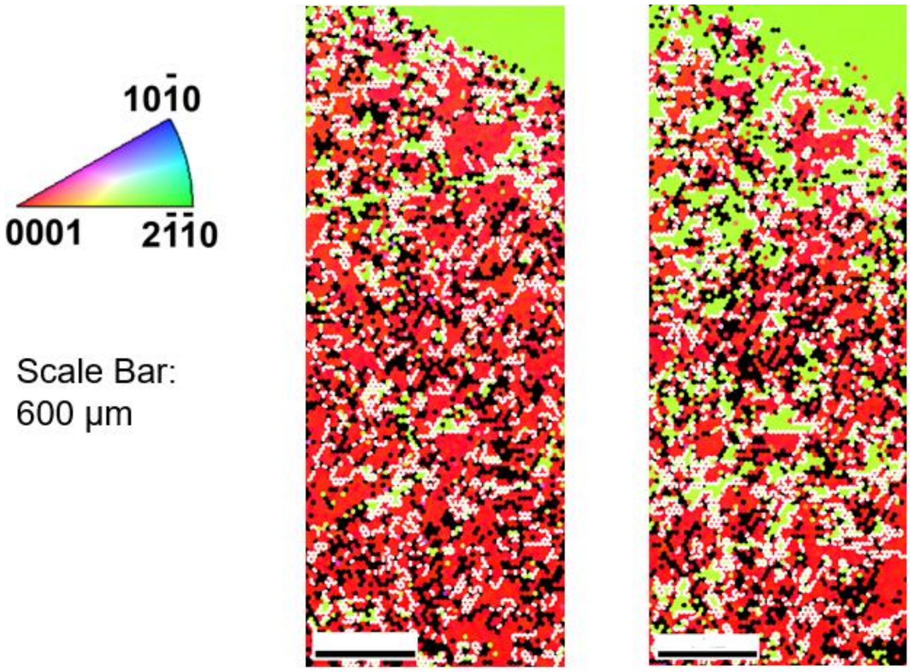

(i) (ii)

**Figure S36-I**. IPF maps of the sample normal direction (001) from EBSD scans of a plasma etched Type B film with the ‘outer’ surface exposed: (i) 1 h (etched by about 60 to 75 nm), (ii) 3 h (about 140 to 175 nm etched). Grain boundaries are represented in white, black areas represent pixels with CI < 0.1 that have not been included and yellow regions are from the bare silicon wafer.

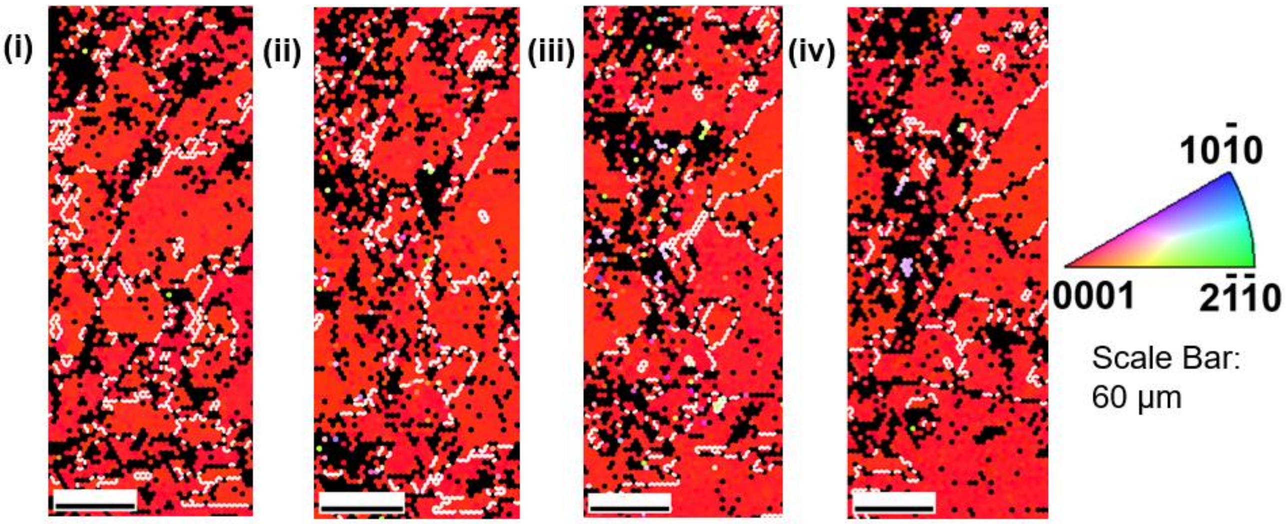

**Figure S36-II**. IPF maps of the sample normal direction (001) from EBSD scans of a plasma etched Type B film with the 'inner' surface exposed: (i) 0 min, (ii) 50 min, (iii) 1 h 50 min, (iv) 4 h (about 160 to 200 nm). Grain boundaries are represented in white, black areas represent pixels with CI < 0.1 that have not been included and yellow regions are from the bare silicon wafer.

However, as oxygen plasma etching is a destructive technique, a reduction of grain size was observed (**Figure S37-I**). Again, 3-4 h (up to 200 nm) of etching resulted in surface roughening (**Figure S37-II**) and the appearance of a prominent D peak (**Figure S37-III**). Similar surface roughening and the appearance of a D peak were observed after plasma etching grade A HOPG (**Figure S38**).

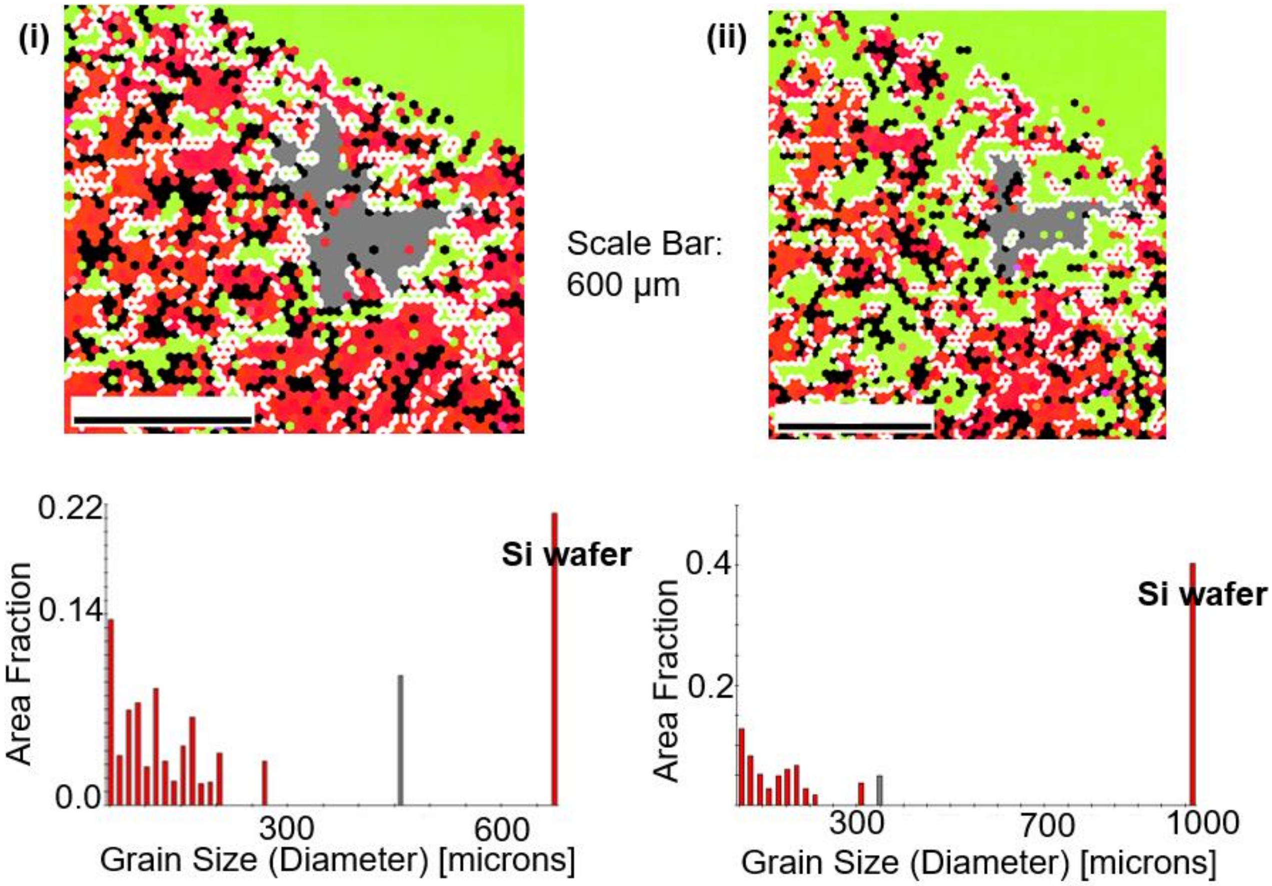

**Figure S37-I**. Grain size reduction with oxygen plasma etching: (i) 1 h, and, (ii) 3 h.

Top: IPF maps of the sample normal direction (001) with the largest grain highlighted in gray; grain boundaries are represented in white, black areas represent pixels with CI < 0.1 that have not been included and yellow regions are from the bare silicon wafer. Bottom: grain size charts with the largest grains highlighted in gray.

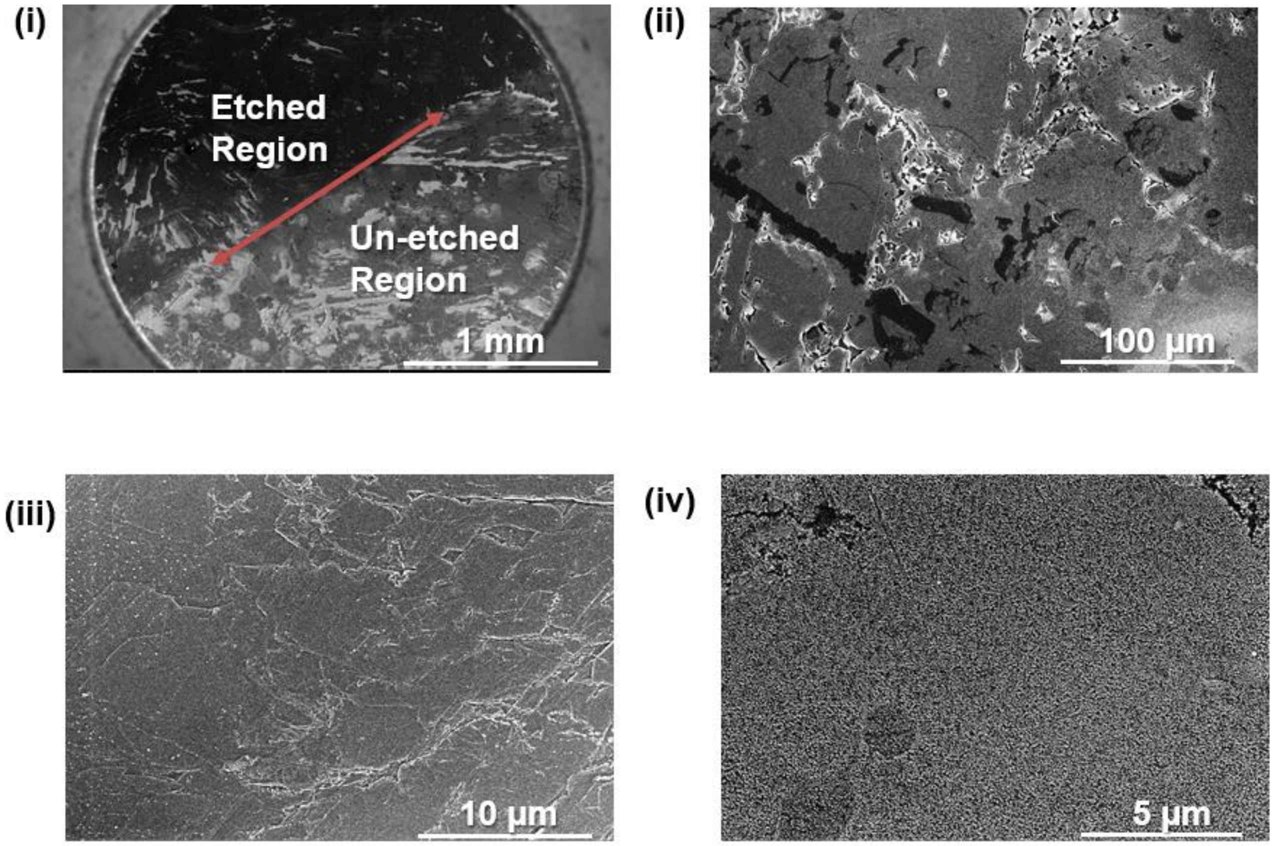

**Figure S37-II**. SEM images of Type B films film etched for 3- 4 h (about 200 nm) with oxygen plasma, scale bars: (i) 1 mm, (ii) 100 µm, (iii) 10 µm, (iv) 5 µm.

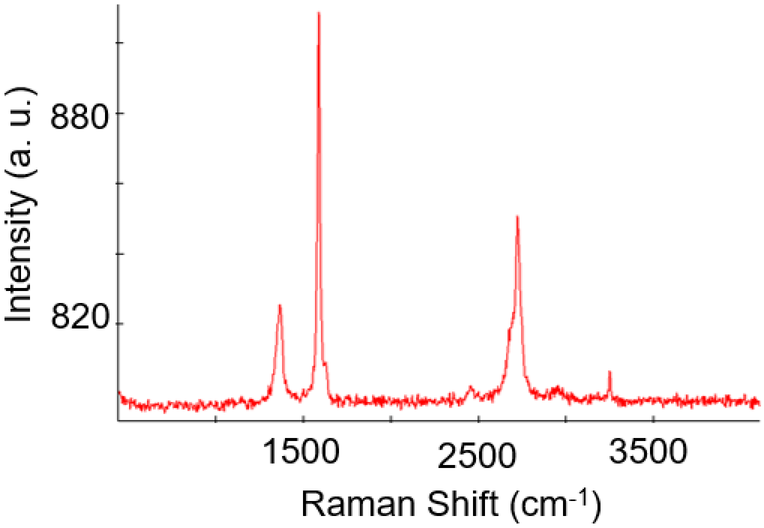

**Figure S37-III**. Typical Raman spectrum of a Type B film etched for 3-4 h (about 200 nm) with oxygen plasma.

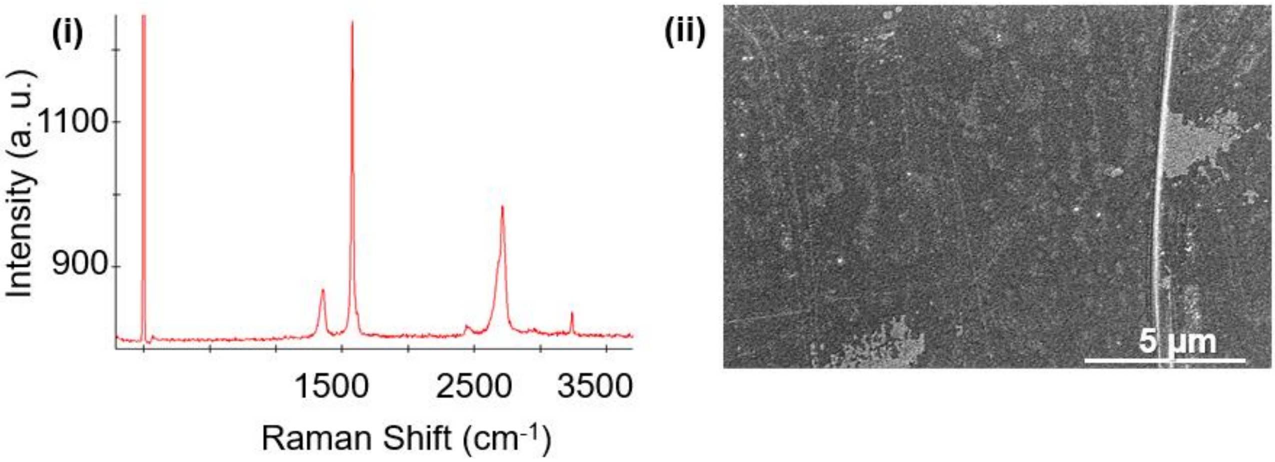

**Figure S38**. An oxygen plasma etched grade A HOPG sample: (i) Raman spectrum after 30 min (about 40-50 nm), (ii) SEM image after 1 h (about 80-100 nm).

Please note that mechanical exfoliation methods (using sticky notes, scotch-tape, carbon tape or transfer tapes) were found, in our hands, to be mostly un-suitable. This was because of the poor adhesion of the films to the silicon substrates; the films would transfer to the adhesive surfaces in their entirety. Also, mechanical damage to the films were possible, making it difficult to reach conclusions about the new surfaces now revealed. Attempts to explore the flakes on the adhesive tapes also proved to be difficult, including keeping track of exactly what depth of the film these new flakes were from and the requirement to transfer such new flakes to flat surfaces (like silicon wafers) on which EBSD and other characterization would be possible. Our efforts as described above suggest to us that new methods (inventing new methods) would seem to be helpful for preparing “sections” of graphite film samples.

## References

1. Colby, R. Y., Q.; Cao, H.; Pei, S. S.; Stach, E. A.; Chen, Y. P. Cross-Sectional Transmission Electron Microscopy of Thin Graphite Films Grown by Chemical Vapor Deposition *Diam. Relat. Mater.* **2010,** *19*, 143-146.
2. Lander, J. J.; Kern, H. E.; Beach, A. L. Solubility and Diffusion Coefficient of Carbon in Nickel - Reaction Rates of Nickel-Carbon Alloys with Barium Oxide. *J. Appl. Phys.* **1952,** *23* (12), 1305-1309.
3. Hwang, J.-W. Thermal Expansion of Nickel and Iron, and the Influence of Nitrogen on the Lattice Parameter of Iron at the Curie temperature. Master's Theses, University of Missouri Rolla, **1972**.
4. Kellett, E. A.; Richards, B. P. The Thermal Expansion of Graphite within the Layer Planes. *J. Nucl. Mater.* **1964,** *12* (2), 184-192.
5. Morgan, W. C. Thermal-Expansion Coefficients of Graphite Crystals. *Carbon* **1972,** *10* (1), 73-79.
6. Lockwood, D. J.; Bertrand, D.; Carrara, P.; Mischler, G.; Billerey, D.; Terrier, C. Raman-Spectrum of NiCl2. *J. Phys. C-Solid State Physics* **1979,** *12* (17), 3615-3620.
7. Cançado, L. G.; Takai, K.; Enoki, T.; Endo, M.; Kim, Y. A.; Mizusaki, H.; Speziali, N. L.; Jorio, A.; Pimenta, M. A. Measuring the Degree of Stacking Order in Graphite by Raman Spectroscopy. *Carbon* **2008,** *46* (2), 272-275.
8. Demirel, M. C.; El-Dasher, B. S.; Adams, B. L.; Rollett, A. D. Studies on the Accuracy of Electron Backscatter Diffraction Measurements. In *Electron Backscatter Diffraction in Materials Science;* Schwartz, A. J.; Kumar, M.; Brent, A. L., Eds.; Springer US: New York, **2000**; Vol. 1, pp 65-74.
9. Muniz, F. T.; Miranda, M. A.; Morilla Dos Santos, C.; Sasaki, J. M. The Scherrer Equation and the Dynamical Theory of X-ray Diffraction. *Acta Crystallogr A Found Adv* **2016,** *72* (Pt 3), 385-90.
10. Miranda, M. A. R.; Sasaki, J. M. The Limit of Application of the Scherrer Equation. *Acta Crystallogr A Found Adv* **2018,** *74* (Pt 1), 54-65.
11. Moore, A. W. Highly oriented pyrolytic graphite. In *Chemistry and Physics of Carbon;* P.L. Walker, J.; Thrower, P. A., Eds.; Dekker: New York, **1973**; Vol. 11, pp 69-187.
12. Grigorieva, I.; Antonov, A.; Gudi, G. Graphite Optics—Current Opportunities, Properties and Limits. *Condensed Matter* **2019,** *4* (1), 18.
13. Garcia, A. P.; Pugno, N.; Buehler, M. J. Superductile, Wavy Silica Nanostructures Inspired by Diatom Algae. *Adv. Eng. Mater.* **2011,** *13* (10), B405-B414.
14. Pugno, N. M. Space elevator: Out of Order? *Nano Today* **2007,** *2* (6), 44-47.
15. Pugno, N. M.; Ruoff, R. S. Quantized Fracture Mechanics. *Philos. Mag.* **2004,** *84* (27), 2829-2845.
16. Song, Z.; Artyukhov, V. I.; Yakobson, B. I.; Xu, Z. Pseudo Hall-Petch Strength Reduction in Polycrystalline Graphene. *Nano Lett.* **2013,** *13* (4), 1829-33.
17. Sha, Z. D.; Quek, S. S.; Pei, Q. X.; Liu, Z. S.; Wang, T. J.; Shenoy, V. B.; Zhang, Y. W. Inverse pseudo Hall-Petch relation in polycrystalline graphene. *Sci. Rep.* **2014,** *4*, 5991.